DESIGN AND ANALYSIS OF METAMATERIAL BASED MICROSTRIP PATCH ANTENNAS FOR WIRELESS APPLICATIONS

Bukola Doyinsola Ajewole

2023

DESIGN AND ANALYSIS OF METAMATERIAL BASED MICROSTRIP PATCH ANTENNAS FOR WIRELESS APPLICATIONS

Bukola Doyinsola Ajewole

217077505

This Thesis is submitted in fulfillment of the requirements for the degree of Doctor of Philosophy: Electronic Engineering

Discipline of Electrical, Electronic and Computer Engineering

School of Engineering, College of Agriculture, Engineering and Science

University of Kwazulu-Natal, Durban, South Africa

Supervisors: Prof Pradeep Kumar

Prof Thomas Afullo

As the candidate's supervisors, we agree to the submission of this thesis.

Signed: _ _____ Date: 07-Feb-2023

Name: Prof Pradeep Kumar

Signed: ___ _____ Date: 7th Feb 2023

Name: Prof Thomas Afullo

DECLARATION 1: PLAGIARISM

I, Bukola Doyinsola Ajewole, with student number 217077505 declare that this thesis titled "**Design and Analysis of Metamaterial Based Microstrip Patch Antennas for Wireless Applications**," declare that;

1. The research reported in this thesis, except where otherwise indicated, is my original work.
2. The thesis has not been submitted for any degree or examination at any other University.
3. This thesis does not contain other persons' data, pictures, graphs, or information, unless specifically acknowledged as being sourced from other persons.
4. This thesis does not contain other persons' writings, unless specifically acknowledged as being sourced from other researchers. Where other written sources have been quoted, then:
    a) Their words have been re-written, but the general information attributed to them has been referenced,
    b) Where their exact words have been used, their writing has been placed inside quotation marks, and referenced.
5. This thesis does not contain text, graphics or tables copied and pasted from the internet unless specifically acknowledged, the source being detailed in the thesis and in the References section.

Signed Date……07- FEB-2023……

Bukola Doyinsola Ajewole

DECLARATION 2: PUBLICATIONS

I, Bukola D. Ajewole declare that the following is the list of publications from this dissertation:

1. B. D. Ajewole, P. Kumar, T. J. O, "Square SRR Metamaterial Inspired Microstrip Antenna for Wireless Mobile Communication*", Proceedings of the International Conference on Artificial Intelligence, Big Data, Computing and Data Communication Systems (IcABCD)*, pp. 1-6, IEEE, 2021.

2. B. Ajewole, P. Kumar, T. Afullo, "I-Shaped Metamaterial Using SRR for Multi-Band Wireless Communication", *Crystals*, vol. 12, no. 4, pp. 1-15, 2022.

3. B. D. Ajewole, P. Kumar, T. Afullo, "A Microstrip Antenna Using I-Shaped Metamaterial Superstrate with Enhanced Gain for Multiband Wireless Systems," *Micromachines*, vol. 14, no. 2, pp. 1-18, 2023.

4. B. D. Ajewole, P. Kumar, T. Afullo, "A MIMO Microstrip Antenna Using I-Shaped Metamaterial Superstrate with Improved Gain and Isolation for Multiband Wireless Systems," *International Journal on Communications Antenna and Propagation*, 2023 (under review).

DEDICATION

To my parents.

ACKNOWLEDGEMENT

My heartfelt gratitude goes to the Almighty God for giving me the strength to pursue this PhD program.

I would like to express my sincere appreciation and gratitude to my highly esteemed supervisor Dr Pradeep Kumar, for his constant motivation and support during my research. I sincerely appreciate his encouragement and contribution from the first day to the end of this thesis.

My deepest appreciation to my exceptional co-supervisor, Professor Thomas Afullo. He has been a source of many ideas, guidance, enthusiasm, and encouragement which made this research possible. Working with him has been my greatest pleasure and am glad to have work under his co-supervision. I appreciate the time spared for me.

I would like to express my gratitude to Mr Taiwo, Dr Femi Oni, Anita Shima, Bukunmi Oyelami, and Ope Ajoro for their immense support and encouragement throughout this work. You are greatly appreciated.

To the wonderful man in my life, Dr. Omotoyosi Craig, without whose consistent support and encouragement I could not have completed this thesis. I appreciate your kindness and love. Through it all, I owe the greatest debt to my parents Prof. & Mrs. Ajewole and my sister Temiloluwa for the active role they took in my education. They have provided me invaluable love and support financially, moraly, and spiritually.

Special appreciation to all the members of staff at the department of Electrical, Electronics and Computer Engineering, University of KwaZulu-Natal, Durban for enabling me to undertake this research.

ABSTRACT

Due to the tremendous growth of wireless communication applications, there is an enormous demand for more compact antennas with high speed, wider coverage, high gain, and multi-band properties. The microstrip patch antennas (MPAs) and multiple-input multiple-output (MIMO) antennas with high gain and multi-band properties are suitable to fulfil these requirements. MPAs have been found to possess unique qualities such as light weight, low profile, easy fabrication, and integration. However, the low gain, narrow bandwidth, and mutual coupling in the MIMO antennas limit the performance of MIMO systems. Several techniques have been studied and implemented over the years, but they are not without limitations. The utilization of artificial materials such as metamaterials has proven to be efficient in overcoming the limitations of MPAs.

Due to the advancement in modern technology, it is necessary to study and use recently developed metamaterial structures. Metamaterials (MeTMs) are artificially engineered materials with electromagnetic properties that are not found in nature. MeTMs are used due to their electric and magnetic properties. The goal of this thesis is to design and investigate a novel metamaterial structure which can be integrated into the microstrip patch antennas for improving their performance. The design, simulation, and measurement of the metamaterial is carried out on the Computer Simulation Technology (CST) studio suite, Advance Design Systems (ADS) software, MATLAB, and the Rohde and Schwarz network analyzer etc.

In this thesis, a novel I-shaped metamaterial (ISMeTM) structure is proposed, designed, and investigated. The proposed novel ISMeTM unit cell structure in this work has a characteristic shape that distinguishes it from earlier multi-band MeTMs in the literature. The structure's unit cell is designed to have an overall compact size of 10 mm × 10 mm. The structure generates transmission coefficients at 6.31 GHz, 7.79 GHz, 9.98 GHz, 10.82 GHz, 11.86 GHz, 13.36 GHz, and 15. 5 GHz. These frequency bands are ideal for multi-band satellite communication systems, C, X, and Ku-bands, and radar applications etc.

The performance of the MPA is improved in this work, by integrating a novel square split ring resonator (SSRR) metamaterial. The performance of the proposed antenna is investigated and analyzed. The SSRR is designed to have a dimension of 25 x 21.4 x 1.6 mm^2 which is the same dimension as the radiating patch of the MPA. The SSRR is etched over the antenna, and it operates at single operating frequency of 5.8 GHz with improved gain from 4.04 to 5.3 dBi.

Further, the MPA with improved parameters for multiband wireless systems is designed, analyzed, fabricated, and measured. The proposed design utilizes the ISMeTM array as superstrate with the area of 70 x 70 mm^2. The superstrate is etched over a rectangular MPA exhibiting multi-band properties. This antenna resonates at 6.31, 9.65, 11.45 GHz with increased bandwidth at 240 MHz, 850 MHz, and 1010 MHz. The overall gain of the antenna increases by 74.18%. The antenna is fabricated and measured. The simulated results and the measured results are found to be in good agreement.

The mutual coupling and low gain problems in MIMO patch antennas is also addressed in this thesis. A 3 x 5-unit cell array of the ISMeTM is used as a superstrate over a two port MIMO patch antenna. The two port MIMO antenna with the superstrate provides triple-band operation and operates over three resonance frequencies at 6.31, 9.09, and 11.41 GHz. A mutual coupling reduction of 26 dB, 33 dB, and 22 dB for the first band, second band and third band, respectively is attained.

In this thesis, a novel I-shaped metamaterial structure is introduced, which produces multiband operation. The presented metamaterial is suitable for various multiband wireless communication applications. The integration of a square split ring resonator metamaterial enhances the performance of the antenna. Using the I-shaped metamaterial a high gain multiband microstrip antenna is designed. The I-shaped metamaterial array is utilized to improve the performance of the MIMO antenna. Various antenna parameters confirm that the presented MIMO antenna is suitable for multiband wireless communications.

Contents

DECLARATION 1: PLAGIARISM i

DECLARATION 2: PUBLICATIONS ii

DEDICATION iii

ACKNOWLEDGEMENT iv

ABSTRACT v

List of Figures x

List of Tables xii

List of Acronyms xiii

Chapter 1 1

Introduction 1

1.1 Introduction 1

1.2 Problem Statement 3

1.3 Research Questions 4

1.4 Research Aim and Objectives 4

1.5 Research Contribution 5

1.6 Organization of the Thesis 6

1.7 Chapter Summary 7

Chapter 2 8

Literature Review 8

2.1 Introduction to Microstrip Patch Antenna 8

2.2 Near Field and Far Field Regions 10

2.2.1 Reactive Near Field Region 10

2.2.2 Radiative Near Field Region 11

2.2.3 Far Field Region 11

2.3 The Parameters of Antenna 11

2.3.1 Radiation Patterns 12

2.3.2 Antenna Directivity 12

2.3.3 Antenna Efficiency 12

2.3.4 Antenna Gain 13

2.3.5 Return Loss 13

2.3.6 Voltage Standing Wave Ratio 14
2.3.7 Polarization 14
2.3.8 Antenna Bandwidth 15
2.4 Types of Antennas 16
2.5 Microstrip Patch Antenna (MPA) 16
2.5.1 Classification of MPA 18
2.5.2 Feeding Techniques for MPA 18
2.5.2.1 Aperture Coupling Technique 19
2.5.2.2 Coaxial Probe Feed 19
2.5.2.3 Proximity Coupling Feed 20
2.5.2.4 Microstrip Line Feed 21
2.6 Techniques for Analyzing MPA 21
2.6.1 Transmission Line Model 22
2.6.2 Cavity Model 22
2.6.3 Full Wave Model 23
2.7 Design Criteria for Rectangular MPA 23
2.8 Methods of Improving MPA Limitations 24
2.9 Metamaterials 27
2.9.1 Classification of MeTMs 30
2.9.2 Left-Handed Material 30
2.10 Applications of Metamaterial 32
2.11 Metamaterial in Antenna Design 32
2.11.1 Bandwidth Enhancement 32
2.11.2 Gain and Enhancement 33
2.11.3 Miniaturization 34
2.12 Parameter Extraction Methods 35
2.12.1 The Nicolson- Ross-Weir Technique 35
2.13 Methodological Approach 37
2.14 Chapter Summary 37
CHAPTER 3 38
I-Shaped Metamaterial Using SRR for Multi-Band Wireless Communication 38
3.1 Introduction 38
3.2 MeTM Unit Cell Geometry and Design 38
3.3 Theoretical Model and Equivalent Circuit of the ISMeTM 40
3.4 Design Methodology 42

3.5 Methodology for Extracting the Unit Cell's Effective Medium Parameters 46
3.6 ISMeTM Unit Cell Analysis 46
3.7 Result and Discussion 48
3.8 ISMeTM Array Analysis 54
3.9 Chapter Summary 60
Chapter 4 61
Microstrip Patch Antennas Using Metamaterial Superstrate with Enhanced Gain 61
4.1 Introduction 61
4.2 Design and Geometry of the SSRR Inspired Patch Antenna (Design 1) 61
4.3 Result of the SSRR Inspired Patch Antenna (Design 1) 64
4.4 Design of MPA using I-Shaped Metamaterial (Design 2) 72
4.4.1 Geometry of the ISMeTM Superstrate 72
4.4.2 Rectangular Microstrip Antenna (ReMPA) Design 76
4.4.3 ReMPA based ISMeTM Superstrate 80
4.5 Equivalent Circuit of the ISMeTM based ReMPA 81
4.6 Result of the Proposed ISMeTM (Design 2) 83
4.7 Chapter Summary 94
Chapter 5 95
Design of a Two-Port MIMO Patch Antenna using I-Shaped Metamaterial Superstrate for Triple-Band Wireless Applications 95
5.1 Introduction 95
5.2 Geometry of the Two-Port MIMO-ANT (Antenna A) 95
5.3 ISMeTM Superstrate based MIMO-ANT (Antenna B) 96
5.4 Results and Discussion 97
5.5 Chapter Summary 108
Chapter 6 110
Conclusion and Future Scope 110
6.1 Conclusion 110
6.2 Future Scope 111
References 112

List of Figures

Figure 2.1: Transmission Techniques [11]. 9
Figure 2.2: Diagram of the Antenna Field Region [11,34]. 11
Figure 2.3: Types of Polarization: (a) Linear, (b) Circular, (c) Elliptical [37]. 15
Figure 2.4: The Geometric Structure of Different MPA. 18
Figure 2.5: Aperture Coupled Feeding Technique [45]. 19
Figure 2.6: Coaxial Probe Feeding Technique [46]. 20
Figure 2.7: Proximity Coupled Feeding Technique [47]. 20
Figure 2.8: Microstrip Line Feeding Technique [11]. 21
Figure 2.9: Transmission Line Model [11]. 22
Figure 2.10: Circular and Rectangular SRR Unit Cell (b) SRR and CSRR with its Equivalent Circuits [72,95]. 29
Figure 2.11: Classification of Metamaterials [86]. 30
Figure 2.12: Wave Propagation of LHM [88]. 31
Figure 3.1: Proposed ISMeTM (a) Unit Cell Configuration, (b) Simulated Model. 39
Figure 3.2: The Equivalent Circuit of the Proposed ISMeTM Structure. 41
Figure 3.3: Design Steps for the Proposed ISMeTM Unit Cell: (a) Design step-a, (b) Design step-b, (c) Design step-c, (d) Design step-d (ISMeTM). 43
Figure 3.4: Reflection and Transmission Parameters of Various Configurations (a) S_{11}, (b) S_{21}, (c) Permittivity. 45
Figure 3.5: S-parameters and Effective Parameters of the ISMeTM (a) S- Parameter, (b) Effective Parameters. 47
Figure 3.6: ISMeTM Unit Cell Parameters (a) Variation of S11 with g, (b) Variation of S21 with g, (c) Variation of S11 with RL, (d) Variation of S11 with W. 50
Figure 3.7: ISMeTM Unit Cell Parameter Variation (a) S21 with Dielectric Constant of the Substrate, (b) S21 with sh, (c) Permittivity and Permeability with ls, (d) Permittivity and Permeability with sh. 53
Figure 3.8: Schematic Diagram of ISMeTM arrays: (a) Geometry and Simulated Model of 1 × 2 Array (b) Geometry and Simulated model of 2 × 2 Array (c) Geometry and Simulated Model of 2 × 4 Array. 55
Figure 3.9: S-Parameters of Array Configuration. 56
Figure 3.10: Parameters of Array Configurations (a) Permittivity, (b) Permeability, (c) Refractive Index. 58
Figure 4.1: Geometry of the Proposed Antenna (a) Radiating Patch (b) SRR Unit Cell (c) Side View. 64
Figure 4.2: Reflection Coefficient Curve of Antenna Loaded with the Square Split Ring Resonator (SSRR). 65
Figure 4.3: Reflection Coefficient for Variation of Air Gap (ag). 66
Figure 4.4: 3D- Radiation Pattern (a) Patch only (b) SSRR inspired Antenna. 67
Figure 4.5: Normalized radiation patterns of the antenna at (a) 5.0 GHz, (b) 5.4 GHz (c) 5.8 GHz. 69
Figure 4.6: 7 X 7 Array Structure of the ISMeTM: (a) Array and Unit Cell (b) Fabricated Array. 73
Figure 4.7: ISMeTM Unit Cell Analysis (a) S11 and S12 (b) Effective Parameters. 75
Figure 4.8: ReMPA Design (a) Top View (b) Side View (c) Fabricated Top and Back View. 78
Figure 4.9: Variation of W 80
Figure 4.10: Proposed ReMPA Based ISMeTM (a) Configuration (b) Fabricated Prototype. 81
Figure 4.11: Equivalent Circuit of the Proposed ISMeTM-ReMPA. 83

Figure 4.12: Simulated S-parameter of the ReMPA with and without ISMeTM Superstrate. 84
Figure 4.13: Reflection coefficient S_{11} (dB): (a) Simulated and Measured (b) Experimental Setup. 86
Figure 4.14: S-Parameter for different Values of ag. 87
Figure 4.15: Radiation parameters of the ReMPA and Proposed Antenna (a) 6.18 GHz (b) 9.65 GHz (c) 11.5 GHz. 89
Figure 4.16: Radiation Characteristics of the Proposed Antenna**: (**a) Realized Gain (b**)** Radiation Patterns at 6.18 GHz **(**c) Radiation Patterns at 9.65 GHz (d) Radiation Patterns at 11.5 GHz. 91
Figure 5.1: Two Port MIMO-ANT. 96
Figure 5.2: Proposed Antenna (a) 3 x 5 ISMeTM Array (b) Configuration. 97
Figure 5.3: Reflection Coefficient and Mutual Coupling of the Antenna A. 98
Figure 5.4: Reflection Coefficient and Mutual coupling of Antennas A and B. 100
Figure 5.5: Mutual coupling and reflection coefficient of Antennas A and B. 102
Figure 5.6: Reflection Coefficient of Antenna B various air gaps. 103
Figure 5.7: Radiation Patterns of Antenna B (a) 6. 31 GHz (b) 9.08 GHz (c) 11.41 GHz. 104
Figure 5.8: Realized Gain of Antennas A and B. 105
Figure 5.9: Envelope Correlation Coefficient of the Antennas A and B. 106
Figure 5.10: Diversity Gain of Antennas A and B. 107

List of Tables

Table 2.1 Types of Antennas 16
Table 2.2 Mostly used Dielectric Substrate [11,42,43] 17
Table 3.1 Parameter of the ISMeTM Unit Cell 40
Table 3.2 Parameters of Various Design Steps 45
Table 3.3 Parameter of ISMeTM Unit Cell, ISMeTM 1 x 2 Array, ISMeTM 2 x 2 Array, and ISMeTM 2 x 4 Array 59
Table 3.4 Comparative analysis of the proposed ISMeTM with the structures in literature 59
Table 4.1 Antenna Dimensional Parameters 62
Table 4.2 Comparison with Conventional Patch and Proposed Antenna 69
Table 4.3 Distance Between the Radiating Patch and SSRR Metamaterial 70
Table 4.4 The Main Lobe and Beamwidth at Various Frequencies 70
Table 4.5 Maximum Gain, Maximum Directivity, and Efficiency of the Antenna 71
Table 4.6 Comparison with Similar Antennas 71
Table 4.7 Dimensional Parameters of the 7 X 7 Array Cell 74
Table 4.8 Dimensional Parameters of the ReMPA 76
Table 4.9 Dielectric Constant and Loss Tangent at Various Frequencies 79
Table 4.10 Computed and Simulated Resonant Frequencies of Various TM_{mnp} Modes for ReMPA 79
Table 4.11 Realized Gain of the ReMPA and the Proposed Antenna 92
Table 4.12 Radiation Parameters of the ISMeTM-ReMPA 92
Table 4.13 Comparison of the ReMPA Based ISMeTM with Related Literature 93
Table 5.1 Two Port MIMO-ANT Parameters 96
Table 5.2 Radiation Parameters for Antennas A and B 107
Table 5.3 Comparison with Related Works 108

List of Acronyms

ag	Air gap
CSRR	Complimentary Split Ring Resonant
DG	Diversity Gain
DNG	Double Negative Material
ECC	Envelope Correlation Coefficient
ENG	Epsilon Negative Material
EMW	Electromagnetic Wave
GHz	Giga Hertz
ISMeTM	I-Shaped Metamaterial
LHM	Left- Handed Metamaterial
NRIM	Negative Refractive Index Material
MeTM	Metamaterial
MNG	Mu-Negative Material
MPA	Microstrip Patch Antenna
Mu-CP	Mutual Coupling
MIMO	Multiple-input Multiple-output
MHz	Mega Hertz
RF	Radio Frequency
RMP	Radiating Metallic Patch

ReMPA	Rectangular Microstrip Patch Antenna
SRR	Split Ring Resonator
SSRR	Square Split Ring Resonator
SNG	Single Negative Material
Tr-line	Transmission Line
UHF	Ultra-High Frequency

Chapter 1

Introduction

1.1 Introduction

The revolution of wireless technology began when Guglielmo demonstrated the transmission of signal between the transmitter and receiver without the use of physical medium in 1896 [1]. Numerous wireless applications have emerged because of the success of the experiment. The emergence of wireless communication systems has resulted in an increase in newer technological devices that meet the need of end users. The antenna is an essential component in wireless communication as it serves an interface between the transmitter and the receiver of radio frequency (RF) signals. The transmitting antenna converts electrical signals into electromagnetic waves (EMW) while the receiving antenna converts EMW back to electrical waves. Hence, the antenna can be said to have reciprocal characteristics. Moreover, the reciprocity theorem does not guarantee that the distribution of current remains static in both transmitting and receiving mode [2]. The electromagnetic theory, which is considered as the fundamental principle behind all antennas, was established by Maxwell in 1873. He merged the theories of electricity and magnetism and expressed their relation through series of equations [3]. In 1886, Hertz showcased the first wireless electromagnetic system. In 1901, Marconi accomplished a major feat by transmitting wireless signals across a vast distance between England and Newfoundland. Since the introduction of Marconi's antenna, the focus of antenna technology has been on wire-related radiation components and operating frequencies as high as the ultra-high frequency (UHF) [4].

Over the years, various types of antennas have been used in wireless system applications. These antennas include but not limited to wire, aperture, array, reflector, lens, and microstrip antennas [5-11]. Due to its numerous uses, the wire antenna is the most traditional and popular of all. However, it does have several shortcomings. The next chapter discusses a comprehensive classification of the various antennas.

The first microstrip patch antennas (MPAs) were proposed in 1953. However, the first practical MPA was developed by Howell in 1970s [12]. The MPA consist of a metallic radiating patch with a dielectric substrate layer and a metallic ground. The radiating patch can be designed in accordance with its intended usage. Due to its noteworthy superiority over other conventional antennas, the microstrip patch antenna (MPA) has established itself as a highly effective radiator for a multitude of applications. The benefits of MPA include, but are not limited to, its cost-effectiveness, low profile planar structures, versatile and compact design, multi-band properties, ease of implementation with integrated circuits, and the capability for mass production. However, it must be noted that MPAs also possess several limitations such as limited bandwidth, low gain, low efficiency, and inadequate isolation between radiating elements [11, 13–15]. Over the years, researchers have proposed various techniques to mitigate the drawbacks associated with microstrip patch antennas (MPA). These techniques encompass the employment of multiple radiating patches in an array configuration, variations in substrate thickness, utilization of high permittivity substrates, modification of radiating patch geometries, utilization of multi-layered substrates, and utilization of artificial materials such as metamaterials [16–21]. However, most of these methods are difficult to implement and mainly work with single patch antennas. In contrast to other techniques for improving antenna performance, metamaterials (MeTMs) have gained widespread application.

Metamaterials (MeTMs) are materials that have been designed artificially and have unique properties [22]. In contrast to conventional materials, some materials exhibit negative permittivity (ε), permeability (μ), and refractive index (n). These characteristics have made it feasible to develop novel ideas, devices, and potential uses in numerous novel applications. The MeTM structures are flexible to use with antenna structures since they have thin surfaces and unit cell size which are less than the guided wavelength λ_g [23,24].

Veselago initially proposed the concept of left-handed materials (LHMs), which would enable the propagation of EMW with electric fields and magnetic fields [25]. Since then, MeTMs have drawn the interest of researchers because of their planar shape and compatibility with the MPA in design and fabrication, which has resulted in improved antenna performance. The MeTMs can be classified into

three major categories: electromagnetic MeTMs, acoustic MeTMs, and mechanical MeTMs to improve the properties of conventional antennas [26]. A more detailed description of these MeTMs is presented in the next chapter. MeTM structures can be utilized for a variety of applications in addition to antennas, such as absorbers, superlens, cloaks, sensors, phase compensators, and more [26, 27]. The periodic metallic structures that make up the MeTM structures are arranged into arrays and printed on a dielectric substrate. In this thesis, a novel MeTM structure has been proposed and utilized to enhance the antenna's performance in terms of bandwidth, gain, and efficiency.

1.2 Problem Statement

Over the past few decades, wireless communications have evolved significantly, and large data rates are now required for many wireless applications. High gain and wide bandwidth are crucial for meeting these demands. As a result, the design and analysis of microstrip patch antennas (MPA) have received considerable attention. MPA are of great interest in wireless communications because they are small, compact, low-profile, flexible, light weight, and possess multi-band properties. Their application is constrained in some systems, nonetheless. The major limitations of MPA are very low gain, narrow bandwidth, and low efficiency due to dielectric losses especially for single patch systems [11, 13-15]. To combat these limitations, numerous researchers have proposed several techniques which includes the use of multiple radiating patches, modifying the shape of the patch, amongst others. However, some of these techniques are bulky and complex to implement.

This research seeks to utilize the use of metamaterial which is an artificial engineering material to enhance the low gain and bandwidth of the MPA. A novel MeTM structure is loaded over the MPA such that the MeTM acts as a reflective plane between the radiating patch and the unit cell. In MIMO patch antennas, a superstrate layer made of the MeTM unit cells is loaded over the radiating elements at a height from the superstrate to the radiating elements. The MeTM superstrate boosts the performance of the MPA to produce a high gain, wider bandwidth, improved radiation patterns for a wider coverage and mutual coupling reduction in MIMO antenna systems.

1.3 Research Questions

This research addresses the problem associated with the low gain, narrow bandwidth, and mutual coupling in single patch and MIMO antenna systems. These limitations are improved by proposing and investigating a novel metamaterial structure suitable for the improvements of the antenna limitations. These questions are addressed by this research:

(a) How can we enhance the bandwidth and gain of the MPA?

(b) What motivates the choice of metamaterial?

(c) How can we achieve a multi-band frequency with the MPA?

(d) How can the metamaterial be used to improve the antenna limitations such as low again and narrow bandwidth in single microstrip patch antenna?

(e) How can the metamaterial reduce the mutual coupling degradation in MIMO antenna systems?

1.4 Research Aim and Objectives

The main shortcomings of MPA systems are low gain and small bandwidths. Similarly, mutual coupling restricts the performance of MIMO antenna systems. The metasurface technology is being used in this research to try to address these shortcomings. A two-dimensional structure called a metasurface has properties that are identical to those of metamaterials. MeTMs can be easily integrated with MPAs because of their planar structure, which simplifies the design and production of these antennas. This research aims to considerably extend literature by increasing knowledge in metamaterial based MPAs. In brief, the following summarizes this research aim and objectives:

(a) To design and investigate a novel metamaterial configuration for multi-band systems.

(b) To improve the parameters of the microstrip patch antennas by integrating antennas with proposed novel metamaterial structure.

(c) To utilize the proposed novel metamaterial configuration for designing multiband antennas.

(d) To reduce mutual coupling in MIMO antenna systems by utilizing the proposed novel metamaterial structure.

(e) To fabricate and test the prototype of the proposed metamaterial structure.

(f) To validate the theoretical simulated with the practical implementation of the proposed metamaterial structure.

1.5 Research Contribution

This research work is carried out to investigate the limitations of single patch antennas and MIMO patch antenna systems. The design, investigation, and analysis of a novel I-shaped metamaterial (ISMeTM) structure for multiband systems constitute the thesis' main contribution. The proposed MeTM unit cell structure in this work has a distinctive shape that sets it apart from previous multi-band MeTMs in the literature. Three square metallic split ring resonators are used in the design of the structure's exterior, and an I-shaped metallic strip makes up the interior. The metallic rings are etched on the low-cost FR-4 dielectric substrate material with thickness of 1. 6 mm and dielectric constant of 4.3. The unit cell of the structure is designed to have an overall compact overall size of 10 mm x 10 mm. The structure produces transmission coefficient at 6.31 GHz, 7.79 GHz, 9.98 GHz, 10.82 GHz, 11.86 GHz, 13.36 GHz, and 15. 5 GHz. These frequency ranges are appropriate for radar applications, C, X, and Ku-bands multi-band satellite communication systems etc.

Secondly, a novel square split ring resonator (SSRR) metamaterial structure inspired MPA for wireless communication systems is proposed and designed. The unit cell of the novel SSRR is designed using two metallic copper rings. The outer rings compromise of four split gaps while the inner ring consists of a single cut. These designs make this structure distinct form other SRR reported in literatures. This SSRR unit cell is placed over the MPA with a single operating frequency band of 5.85 GHz at a height of 9 mm. The dimension of the SSRR is the same as the radiating patch of the MPA. The bandwidth of the conventional MPA increased from 350 MHz to 430 MHz as the SSRR is etched over the patch. This antenna is suitable for use in WiMAX and Wi-Fi application in wireless communication systems.

This work is further extended by utilizing the novel I-shaped metamaterial as superstrate over a MPA with multiple operating frequency bands. The superstrate comprises of a 7 x 7-unit cell array of

the ISMeTM with total dimension of 70 mm x 70 mm. The superstrate is integrated with the MPA at a height of 7 mm from the ground plane. The proposed antenna is designed, simulated, fabricated, and measured. The proposed antenna radiates at 6.18 GHz, 9.09 GHz, and 11.5 GHz with a high gain enhancement of 65.17%, 69.83%, and 74.18% over the three frequency bands. The proposed is fabricated and measured, the simulated and measured antenna are found to be in close match.

Finally, a two-port MIMO patch antenna with enhanced gain and reduced mutual coupling for multiband wireless applications is designed and analyzed. To reduce the mutual coupling of the two-port MIMO patch antenna, a superstrate consisting of a 3 x 5-unit cell array of the ISMeTM is used. The antenna's gain and bandwidth are enhanced as the mutual coupling of the antenna is decreased.

1.6 Organization of the Thesis

The structure of the thesis is given below:

Chapter 1 presents the introduction of the MPA, research aim, research objectives, research contributions, and organization of study.

Chapter 2 discusses the fundamentals of MPAs, antenna parameters, design criteria for the MPAs, the theory of metamaterials, and review of relevant literatures that includes the application of metamaterials in antenna designs.

Chapter 3 discusses the design and analysis of the I-shaped metamaterial using SRR for multi-band wireless communication. The effective parameters of the metamaterial unit cell such as permittivity, permeability, and refractive index are studies and analyzed. The simulation of the metamaterial is carried out using the CST studio suite.

Chapter 4 presents the design and analysis of the patch antenna using I-shaped metamaterial superstrate for multiband wireless systems. The proposed ISMeTM based microstrip patch antenna was fabricated and measured. The simulated and measured results are compared and discussed.

Chapter 5 presents the design of a two-port MIMO patch antenna using ISMeTM superstrate for triple-band wireless applications. The ISMeTM superstrate was utilized to enhance the gain of the antenna and to reduce the mutual coupling in the two port MIMO patch antenna.

Chapter 6 presents the conclusion and the future recommendation of the work.

1.7 Chapter Summary

This chapter discusses the background of antennas, microstrip patch antennas, metamaterials, research problems, contributions, and thesis organization. The flexibility, compactness, and ease of fabrication of the MPAs, among many other benefits, increase their suitability for use in wireless communication. The MPAs, however, has a limited gain and narrow bandwidth. This thesis offers a novel metamaterial structure to improve MPAs' wireless communication performance.

Chapter 2

Literature Review

2.1 Introduction to Microstrip Patch Antenna

This chapter examines the microstrip patch antenna, including its fundamental principles and practical applications. The chapter encompasses a succinct examination of the feeding methodologies, analytical procedures for determining microstrip antenna parameters, and mathematical frameworks utilized. Furthermore, the chapter delves into the arena of metamaterial design and its fundamental principles, including the categorization of metamaterials, their electromagnetic characteristics, and real-world utilization.

The revolution of wireless technology began when Guglielmo demonstrated the transmission of signal between the transmitter and receiver without the use of physical medium in 1896 [1]. Numerous wireless applications have emerged because of the success of the experiment. The emergence of wireless communication systems has resulted in an increase in newer technological devices that meet the need of end users. The antenna is an essential part in wireless communication as it serves a link between the transmitter and the receiver of radio frequency (RF) signals. The transmitting antenna converts electrical signals into electromagnetic waves (EMW) while the receiving antenna converts EMW back to electrical waves. Hence, the antenna can be said to have reciprocal characteristics. Moreover, the reciprocity theorem does not guarantee that the distribution of current remains static in both transmitting and receiving mode [2]. The electromagnetic theory, which is considered as the fundamental principle behind all antennas, was established by Maxwell in 1873. He merged the theories of electricity and magnetism and expressed their relation through series of equations [3].

There are various types of antennas employed in communication systems. These includes wire antennas, aperture antennas, array antennas, reflector antennas, lens antennas and microstrip antennas. Among the most prominent antenna types is the wire antenna. They consist of long wire stretched over the surface. Antennas with a hole or opening at the end are known as aperture antennas. These antennas

are protected from the impacts of the environment by dielectric materials that surround these apertures. The array antennas are multiple antennas connected to work as a single antenna [28]. A feed system for transmitting and/or receiving EMW is included in reflector antennas, which can have one or more reflecting surfaces. Lens antennas are a type of three-dimensional electromagnetic device with a non-uniform refractive index. Using the appropriate lens material, this antenna is made to complement the incident divergent energy and transform it into plane waves. The microstrip antennas have a metallic patch placed on a dielectric material above a metallic ground plane, making them low-profile antennas [11,28-32].

Before we can determine how radiation occurs in antenna technology, it is imperative that we analyze the radiation mechanism. The main factor for the conducting wire to radiate is a change in current. If there is no current flow and no charge movement in the wire, radiation won't happen. Radiation would not occur even if the charges were moving along the straight wire at a steady speed. But when a charge moving along a wire is bent or coiled at a steady pace, radiation is produced [11]. The radiation techniques of the antenna are presented in Figure 2.1. A sinusoidal electric field (E-field) occurs when the transmission line is fed with an alternating voltage.

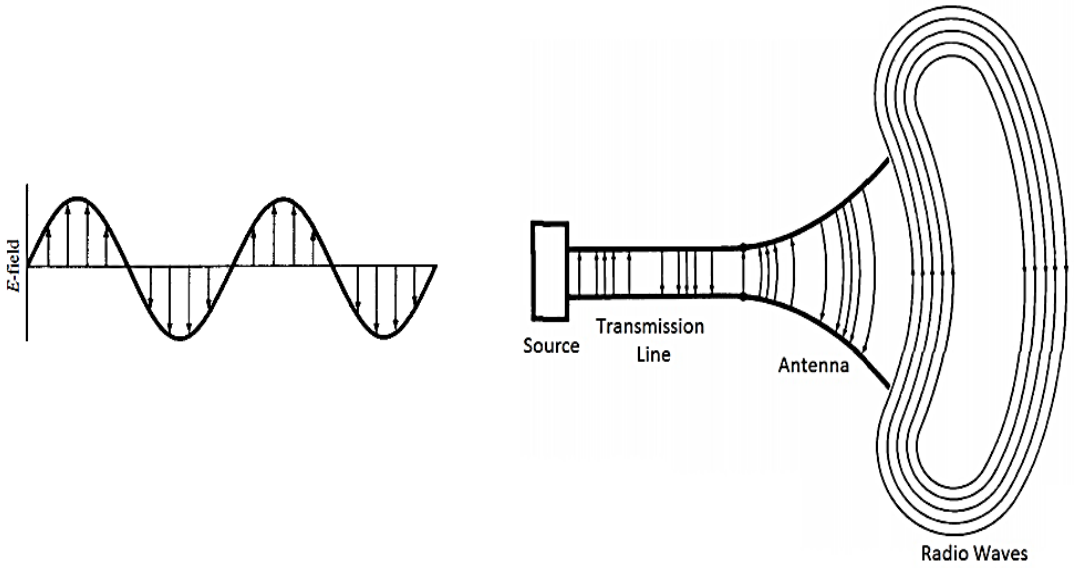

Figure 2.1: Transmission Techniques [11].

The clustering of the electric line of force shows the proportion of the E-field. The electric lines of force coercively eliminate the conductors' free electrons, and the current that emerges from the movement of these charges produces a magnetic field (M-field). The EMW is produced by the time-varying E-field and M-field that flow between the conductors. The ends of the electric lines are interconnected to generate radio waves as these waves travel toward the space. At the source, an electric disturbance is generated, and EMW are consistently produced. These passes through the transmission line and are radiated into space by the antenna [11,33]

2.2 Near Field and Far Field Regions

The antenna is surrounded by two regions, the near field and far field. The radiation pattern is determined in the far-field region and is represented as a function of the directional coordinates. The near field is the closest region to the antenna, as we further away, the field patterns shift. The near and far fields do not act in the same way because the inductive and capacitive effects lose power at a quicker rate with distance than they do at the far field radiation. The near field is classified into two categories, the reactive near field and radiative near field regions. The diagram for the antenna field region is illustrated in Figure 2.2. Hence, the fields surrounding the antenna is divided into three regional parts:

I. Reactive near field region
II. Radiative near field region
III. Far field region

2.2.1 Reactive Near Field Region

Due to the reactive field predominate in this region, energy here occurs as a reaction. Since the fields in this area are mostly reactive fields and the radiating fields are perpendicular but in phase, the E and H fields are out of phase by 90^0 from one another. The outer boundary of this region exists at distance $R_e < 0.62\sqrt{\frac{D^3}{\lambda}}$ from the antenna surface. Where D, and λ are the antenna's diameter and the operating wavelength of the EMW [12].

2.2.2 Radiative Near Field Region

This region of the antenna is between the reactive near field and the far field region. This region can also be referred to as the Fresnel region. In this region the reactive fields are not dominate, the radiating field begin to emerge. The radiation pattern could differ appreciably with distance. The inner boundary is taken at distance $R_a \geq 0.62\sqrt{\frac{D^3}{\lambda}}$ and outer boundary distance $R_a < \frac{2D^2}{\lambda}$ [11].

2.2.3 Far Field Region

This region comes after the radiative near region. The electromagnetic fields are dominated by radiating fields in this region. The E and H fields are orthogonal to each other and to the direction of propagation as the plane waves. This is a region can also be referred to as the Fraunhofer region $R_a < \frac{2D^2}{\lambda}$ [11].

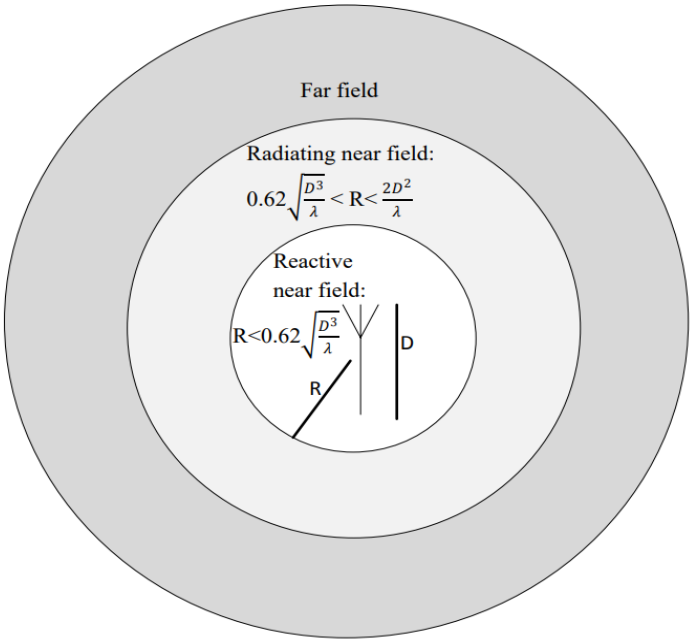

Figure 2.2: Diagram of the Antenna Field Region [11,34].

2.3 The Parameters of Antenna

A set of parameters can be used to evaluate the performance of the antenna. Some of the relevant parameters are explained in the section below.

2.3.1 Radiation Patterns

The radiation pattern or antenna pattern refers to the graphical illustration of the radiation properties of the antenna as a function of spatial coordinates. The spatial coordinate system is used to calculate and analyze an antenna's radiation pattern in the far field area. The isotropic antennas radiate equally in all directions. The radiation from the homogeneous antennas is uniform throughout [5, 11]. The far field radiation pattern can be represented graphically as a plot of one of several related variables, including the field strength, power pattern, and directive gain. The plotted quantity may be shown in dB or on a linear scale. The plot is represented as a three - dimensional graph in magnetic (H- Field) and electric (E- Field).

2.3.2 Antenna Directivity

The directivity of an antenna determines the extent to which the radiation being emitted is concentrated in a direction. It can be defined as the ratio of the radiation intensity from the antenna in a specific direction to the radiation intensity in all directions. This implies that the directivity of the antenna, has the capacity to focus and concentrate the radiated power in a particular direction. It can be expressed as [11]

$$D_i = \frac{U}{U_0} = \frac{4\pi U}{P_{RD}} \tag{2.1}$$

When the direction is not indicated, the maximum directivity can be expressed as:

$$D_{MX} = D_0 = \frac{U_{MX}}{U_0} = \frac{4\pi U_{MX}}{P_{RD}} \tag{2.2}$$

where D_i, D_0, U, U_0, U_{MX}, and P_{RD} are the directivity, maximum directivity, radiation intensity, radiation intensity of the isotropic source, maximum radiation intensity and total radiated power, respectively.

2.3.3 Antenna Efficiency

The efficiency of the antenna can be described as the power radiated (P_{RD}) by the antenna to the input power supplied (P_S) to the antenna. When considering the antenna efficiency, losses in the antenna must be considered. These losses may be due to the reflection caused by mismatch which occurs between the

antenna and the transmission, and the conduction and dielectric losses. It can be expressed mathematically as [11]

$$E_T = E_R E_C E_D \tag{2.3}$$

The E_T, E_R, E_C, and E_D represent the total efficiency, reflection efficiency, conduction efficiency, and the dielectric efficiency, respectively.

2.3.4 Antenna Gain

The antenna gain is the ratio of the intensity in one direction to the intensity that would be obtained if the antenna were to emit its power uniformly in all directions. The antenna gain combines the directivity and efficiency of the antenna. The gain of a receiving antenna indicates how effectively it transforms radio waves that are coming from a specific direction into electrical power. The gain is measured in decibel (dBi) and can be expressed as [35]

$$Gain = 4\pi \frac{Rad_{in}}{Tp_{in}} \tag{2.4}$$

where, Rad_{in} and Tp_{in} are the radiation intensity and the total input power of the antenna, respectively.

2.3.5 Return Loss

The signal that is reflected or returned by a transmission line discontinuity suffers from a power loss referred to as return loss (RL). An antenna's impedance matching is measured by the RL of the antenna. The power delivered to the load is below maximum due to this mismatch. Return loss is the term used to describe the wasted energy that is sent back to the source without being sent to the load. When RL is less than or equal to 10dBi, the matching is adequate, and enough power is provided to the load. The R_L is expressed mathematically as [30]

$$R_L = -20 \log_{10}|\Gamma| \tag{2.5}$$

where the reflection coefficient (Γ) indicates the amount of EMW reflected by an impedance mismatch in the transmission medium.

2.3.6 Voltage Standing Wave Ratio

The ratio between the transmitted and reflected wave is known as the voltage standing wave ratio (VSWR). As it evaluates the effectiveness of the antenna, the VSWR is connected to the return loss. It shows how effectively the antenna's impedance matches the distinctive impedance of the transmission line. More power is transmitted to the antenna and the antenna is better suited to the transmission line when the VSWR is reduced. The range value for VSWR to obtain a high impedance is between 2.0 and 1.0. The reflection coefficient (Γ) is given as [36]

$$\Gamma = \frac{V_R}{V_T} = \frac{Z_I - Z_S}{Z_I + Z_S} \tag{2.6}$$

Where V_R and V_T denotes the amplitude of the reflected wave and incident wave. The input impedance Z_I and impedance of the transmission line Z_S can be expressed as [36]

$$Z_I = R_I + jX_I \tag{2.7}$$

$$Z_S = R_S + jX_S \tag{2.8}$$

where R_I, X_I and R_S, X_S represent the transmission line's resistance and reactance as well as the antenna's input terminals' resistance and reactance. The VSWR is given by [30]

$$VSWR = \frac{1 + |\Gamma|}{1 - |\Gamma|} \tag{2.9}$$

2.3.7 Polarization

The antenna polarization is the far-field measurement of the polarization of the fields radiated by an antenna. We can imply that it describes the direction in which electric field components oscillate. These fields are always parallel to one another and parallel to the propagation direction. Polarization can be classified into three parts, linear, circular, and elliptical [37]. The type of polarizations is presented in Figure 2.3.

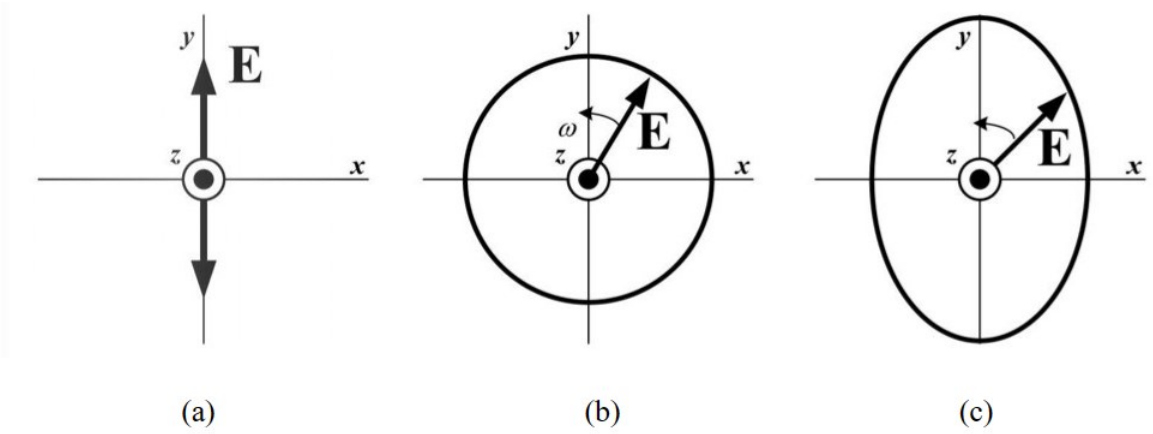

Figure 2.3: Types of Polarization: (a) Linear, (b) Circular, (c) Elliptical [37].

2.3.8 Antenna Bandwidth

The bandwidth of the antenna describes the frequency ranges over where the antenna meets specific performance requirements. One of the criteria used to evaluate an antenna's performance is its optimal antenna bandwidth. The mathematical expression for the antenna's bandwidth is given by [35]

$$BDW = F_H - F_L \tag{2.10}$$

The highest frequency and the lowest frequency are denoted by F_H and F_L, respectively. The broadband and narrow band bandwidth of the antenna can also be expressed as [38]

$$BDW_{broadband} = \frac{F_H}{F_L} \tag{2.11}$$

$$BDW_{narrowband} = \frac{F_H - F_L}{F_C} \tag{2.12}$$

The center frequency is denoted by F_C. It is given as [5]

$$F_C = \frac{F_H + F_L}{2} \tag{2.13}$$

The percentage bandwidth is given as:

$$BDW = BDW_{narrowband} \times 100\% \tag{2.14}$$

2.4 Types of Antennas

The major six types of antennas namely wire, aperture, array, reflector, lens and microstrip are discussed in this section [5-7, 9,11,30-33]. In Table 2.1, the merit, demerit, and areas of applications of the antenna types are discussed.

Table 2.1 Types of Antennas

Antenna classification	Types of antennas	Merit	Demerit	Area of Application
Wire	Dipole, Short dipole, Half-wave dipole, Folded dipole, Monopole, Helical, Loop, Broadband, Cloverleaf	• Simple design • Low cost	• Dipole antenna exhibits a large size. • Helical antennas are bulky. • Loop antennas have poor gain and extremely narrowband.	Space crafts, automobile, missiles, microwave communication, ships, satellite.
Aperture	Slot, microstrip slot, waveguide, horn, waveguide	• Easy fabrication • Omni- directional radiation	• Poor radiation • Increase in VSWR	Microwave Radars
Array	Broadside, End-fire, Collinear, Parasitic	• High gain applications • Controlled radiation patterns • Increased signal strength	• Complex maintenance • High resistive losses • Bulky	Military radars, astronomical observation, long distance communication
Reflector	Flat-plate, corner, parabolic	• Suitable for long distance applications	• Bulky	Radio astronomy, microwave communication, satellite tracking.
Lens	Dielectric, metal plate	• Used in high frequency applications. • flexible	• Expensive • Heavy and Bulky	Microwave
Microstrip	Circular, rectangular	• Low profile • Easy fabrication • Inexpensive • Compact and flexible	• Low gain • Narrow bandwidth	Aircraft, spacecraft, satellites, missiles, cars, mobile phones, Wi-fi, WLAN.

2.5 Microstrip Patch Antenna (MPA)

The first microstrip patch antennas (MPAs) were proposed in 1953. However, the first practical MPA was developed by Munson and Howell in 1970s [12,39,40]. A MPA comprises of a metallic

ground plane and a radiating metallic patch printed on one side of the dielectric substrate. Recently, the research community has shown significant interest in the MPAs due to its various advantages, such as their low profile, simple fabrication, flexible and compact design, multiband properties, and ease of integration with integrated circuits which make these antennas suitable for various wireless applications [11,13,14,41].

Although it has numerous advantages, its performance is limited by low gain, narrow bandwidth, and low efficiency. For the MPA to work at its best, a couple of factors must be considered during fabrication. These factors are the type and thickness of the dielectric substrate to be utilized, the patch's size and shape, the feeding techniques, and the resonant frequency [11]. The choice of the dielectric substrate type is the most vital, even though all the requirements are significant. It needs to be selected based on cost, effectiveness, size, and accessibility. The most popular substrates and their specifications are included in Table 2.2.

Table 2.2 Mostly used Dielectric Substrate [11,42,43]

Substrate	Thickness (mm)	Dielectric constant ($\boldsymbol{\varepsilon_r}$)	Loss tangent ($\boldsymbol{tan\delta}$)
Rogers R03003	1.575	3.00	0.0010
Rogers R03010	3.175	10.2	0.0022
Rogers Duroid 5880	0.127	2.20	0.0009
Rogers R04003	0.203	3.55	0.0027
Rogers R04350	0.030	3.48	0.004
Roger Duroid 6010	0.005	10.7	0.0060
FR4 glass epoxy	1.5-1.6	4.4	0.02
Nylon fabric	0.25	3.6	0.0083
Bakelite	-	4.8	0.0305
Taconic	0.09	3.2	0.003

2.5.1 Classification of MPA

The radiating metallic patch (RMP) ($h << \lambda_0$) is placed on a fraction of the wavelength on top of the metallic ground plane ($hs << \lambda_0$). Where, h is the thickness of the RMP, λ_0 is the free space wavelength, hs is the height of the substrate such that ($0.003\lambda_0 \leq hs \leq 0.05\lambda_0$) [11]. The radiating metallic patch (RMP) is often made of thin copper foil that has been nickel, tin, or another corrosion-resistant metal plated on it. This is due to the desired characteristics of these metals, such as low resistance, ease of soldering, and resistance to oxidation [44,45]. The MPA comes in a variety of shapes that have been tailored to fit requirements. Some of the most used shapes includes but not limited to circular, square, dipole, rectangular, elliptical, and triangular. The geometric structure of different MPA shapes is shown in Figure 2.4.

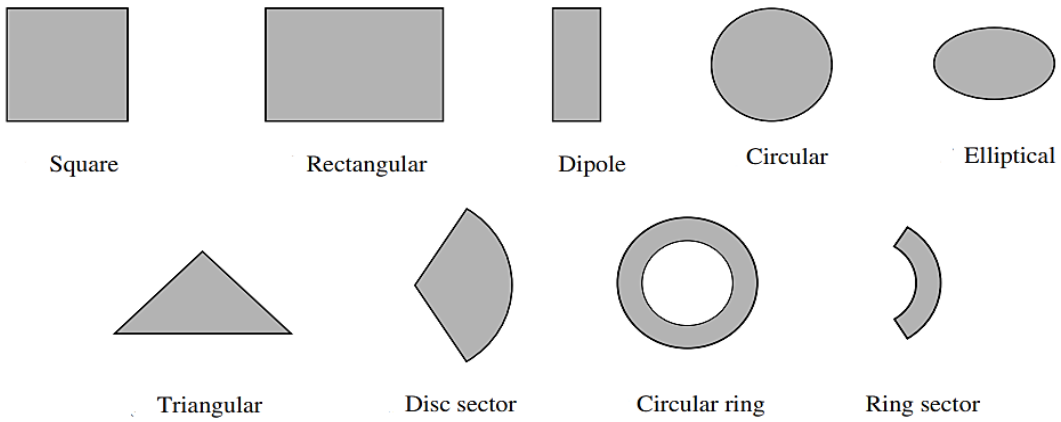

Figure 2.4: The Geometric Structure of Different MPA.

2.5.2 Feeding Techniques for MPA

The feeding techniques play a significant role in antenna design since they have a direct impact on an antenna's input impedance and characteristics. The antenna feeding techniques can be divided into two categories which are contacting and non-contacting feeding techniques. The four most popular techniques used in MPA are microstrip line (ML), coaxial probe (contacting techniques), aperture coupling and proximity coupling (non-contacting).

2.5.2.1 Aperture Coupling Technique

The metallic ground plane is positioned between two dielectric substrates when using the aperture coupling (ACP) techniques. For the upper substrate layer, a substrate material with a low dielectric constant is utilized, and for the lower substrate, a substrate material with a higher dielectric constant. While the ML is put on the bottom substrate, the RMP is put on the upper substrate. The feedline is coupled to the patch via the aperture slot cut in the ground plane. The ACP involves multiple layer fabrication, making it the most challenging feeding technology to fabricate. The antenna's bandwidth is often narrowed by the utilization of ACP [9,30,35,46]. The aperture coupled feeding technique is depicted in Figure 2.5.

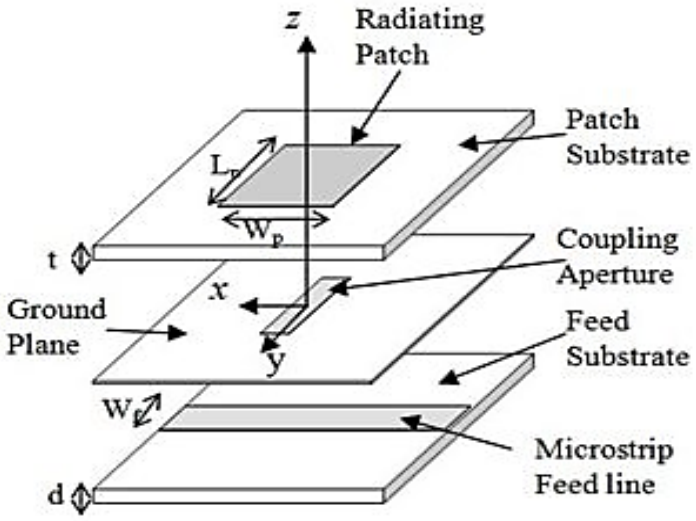

Figure 2.5: Aperture Coupled Feeding Technique [45].

2.5.2.2 Coaxial Probe Feed

Coaxial probing is a widely popular method for feeding MPA. The outer conductor of the coaxial connector/probe feed is soldered to the metallic ground plane, while the inner conductor passes through the dielectric and is attached to the RMP. This technique's advantage is that the connector can be placed anywhere with a patch that matches the impedance. However, the substrate's thickness increases thereby causing an impedance mismatch and difficulty in fabrication [6,11]. Figure 2.6 shows the coaxial probe feeding technique.

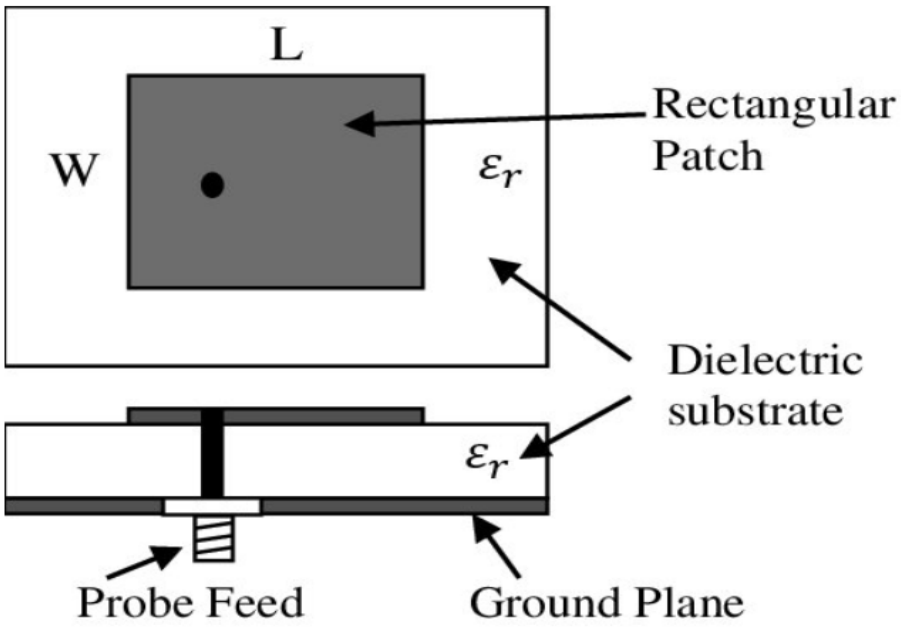

Figure 2.6: Coaxial Probe Feeding Technique [46].

2.5.2.3 Proximity Coupling Feed

The proximity coupling feed technique can be achieved by two techniques. Firstly, by separating the patch and the feedline by using a small gap and by mounting the patch and the feedline on different substrate layers. This approach produces a wide bandwidth and is simple to model. It is, nevertheless, quite challenging to fabricate [11,47]. The proximity coupled feeding technique is shown in Figure 2.7.

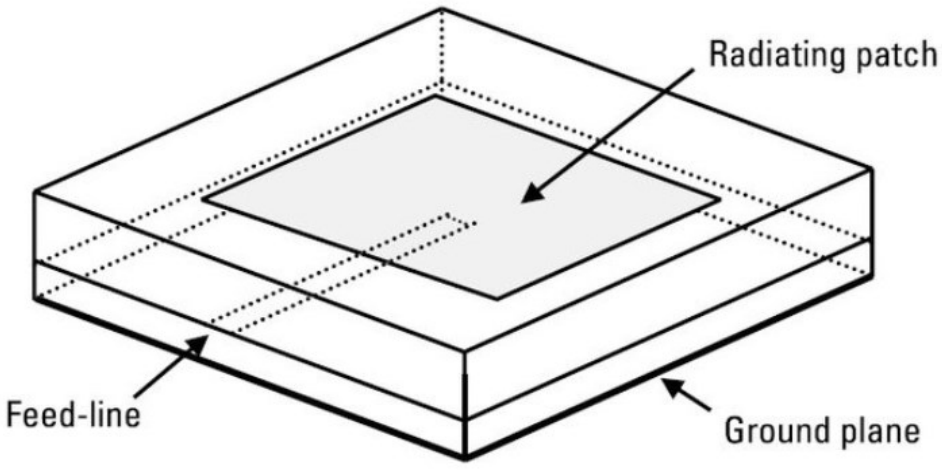

Figure 2.7: Proximity Coupled Feeding Technique [47].

2.5.2.4 Microstrip Line Feed

The microstrip line feed (MLF) is a technique where the conducting strip is connected directly to the patch. The ML is etched onto the surface of the dielectric substrate, giving the structure a planar advantage. This technique is easy to fabricate due to having a single layer. In this technique, an inset cut is made in the patch, which aids in matching the impedance of the feedline to the patch without the use of an additional matching component. The microstrip feeding technique is shown in Figure 2.8. The significant advantage of this feeding method includes its planar structure, ease of modeling, ease of fabrication, and ease of matching (by insert feed). The major drawbacks of this feeding method include the limitation of antenna bandwidth and the increase in spurious radiation and surface waves caused by the rise in substrate height [11,48].

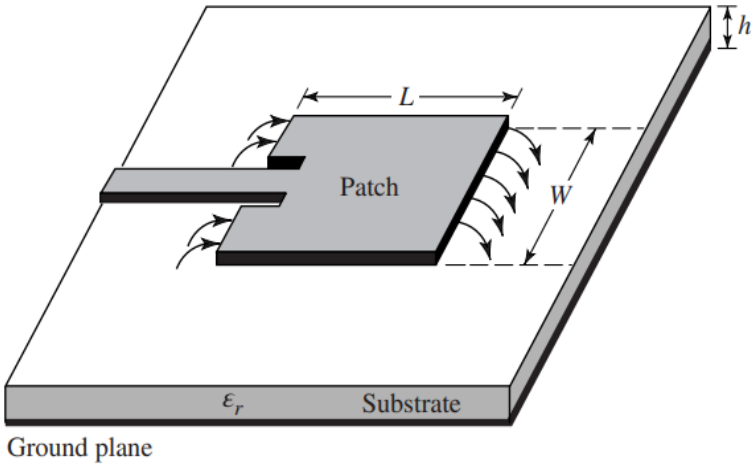

Figure 2.8: Microstrip Line Feeding Technique [11].

2.6 Techniques for Analyzing MPA

There are many techniques for analyzing the MPA. There are three main techniques namely, the transmission line (Tr-Line) model, cavity model, and full wave model (primary integral equations/moment method) [11,29].

2.6.1 Transmission Line Model

The transmission line (Tr-Line) model is the most used model due to its simplicity. In this model, the RMP is considered as a Tr-Line without any variation in transverse field, and at the open circuit ends, there are fringing fields. The fringing fields at the open circuited ends are where the radiation is primarily produced [6,7,11]. It represents the RMP as two slots separated by a low impedance (Z_C) with a transmission line of length L_T. The Tr-Line was initially developed for the rectangular RMP. However, it has since been modified to be compatible with other patch geometries. The Tr-Line model for the MPA is illustrated in Figure 2.9.

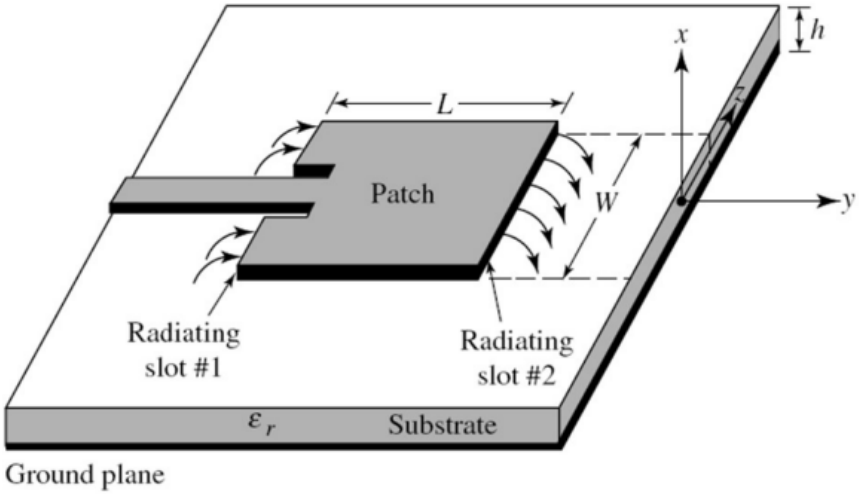

Figure 2.9: Transmission Line Model [11].

2.6.2 Cavity Model

The cavity model used to analyse the MPA is based on the concept that the region between the RMP and the ground plane is a resonance cavity bordered by magnetic walls along the conductor's edge and the top and bottom sides of an electric conductor. By expanding the RMP boundary outward so that the effective sizes are greater than the physical size of the patch, the fringing fields around the edge are addressed. The conductor loss and the effect of the antenna's radiation are taken into consideration by adding these losses to the dielectric substrate's loss tangent. The cavity model is more precise but also

more complex than the Tr-Line model. Although it has been utilized successfully, it also provides good physical understanding and is somewhat difficult to represent coupling [11,15].

2.6.3 Full Wave Model

The cavity model is expanded upon in the full wave model (FDM). This method models the electromagnetic fields outside and within the patch separately. The patch is analyzed as a 2D planar network with several ports scattered throughout. By including an equivalent edge admittance network, the fringing fields at the edges and the radiated fields are integrated. The FDMs are more precise and adaptable than the Tr-Line and cavity models. However, modelling them is the most difficult and they typically provide little physical information.

2.7 Design Criteria for Rectangular MPA

When designing an MPA, several criteria such as the antenna dimension and geometry, the dielectric constant, loss tangent and thickness/ height of the substrate material must be put into consideration. The antenna's dimensions have a very negligible effect on resonance frequency and radiation patterns. The antenna's bandwidth is, however, significantly impacted. It implies that the bandwidth and radiation efficiency increase because of the RMP's width. For a rectangular antenna (Rec-antenna), the width of the RMP should be greater than the length of the RMP to avoid triggering undesirable modes. The length of the radiating patch L_P is given as [2,7,11,12]

$$L_P = \frac{c}{2f_r\sqrt{\varepsilon_r}} \tag{2.15}$$

The antenna's patch is not the only region where the fields might occur. The fringing field, a small portion of the fields, is located outside the antenna. We must determine the effective dielectric constant ε_{reff} to take the fringing field effect into consideration.

$$L_P = \frac{c}{2f_r\sqrt{\varepsilon_{reff}}} \tag{2.16}$$

The width of the radiating patch can be calculated as

$$W_P = \frac{c}{2f_r\sqrt{\frac{\varepsilon_r + 1}{2}}} \tag{2.17}$$

$$W_P = \frac{c}{2f_r}\sqrt{\frac{2}{\varepsilon_r + 1}} \tag{2.18}$$

where the resonance frequency is denoted as f_r, the dielectric constant of the substrate is expressed as ε_r, and c is given as the speed of light (3 x 10^8 m/s) By considering the fringing effect that occurs in the dielectric constant, we can express the effective dielectric constant as given by [11]

$$\varepsilon_{reff} = \frac{\varepsilon_r + 1}{2} + \frac{\varepsilon_r - 1}{2\sqrt{1 + \frac{12s_h}{W_P}}} \tag{2.19}$$

The patch's actual length and effective length L_{eff} can be expressed as [11]

$$L_p = L_{eff} - 2\Delta L \tag{2.20}$$

From equation (2.16), we can calculate the L_{eff}. It can be expressed as

$$L_{eff} = \frac{C}{2f_r\sqrt{\varepsilon_{reff}}} \tag{2.21}$$

Therefore, ΔL is expressed as [22,49]

$$\Delta L = 0.412sh\,\frac{\left(\varepsilon_{reff} + 0.3\right)\left(\frac{W_P}{s_h} + 0.264\right)}{\left(\varepsilon_{reff} - 0.5258\right)\left(\frac{W_P}{S_h} + 0.8\right)} \tag{2.22}$$

The length (L_g) and the width (W_g) of the MPA ground plane can be expressed as:

$$L_g = 6 \times sh + L_p \tag{2.23}$$

$$W_g = 6 \times sh + W_p \tag{2.24}$$

2.8 Methods of Improving MPA Limitations

Numerous methods to improve the performance of the MPA have been adopted and investigated by various researchers in literatures. There are several ways to improve the impedance matching of the MPAs, such as by including more patches in the array configuration, increasing substrate thickness,

incorporating plates or high permittivity substrates, adjusting the patch structure, utilizing multiple substrates, and loading the patch with artificial materials [16-20, 50-62].

A 4 x 4 dual polarized aperture coupled MPA array was designed, optimized, and fabricated by Islam et al [16]. The developed MPA operated over the 22 GHz- 26.5 GHz frequency band with realized gain of 16 dBi. Also, an 8 x 8 linearly polarized aperture MPA was presented for a long-range millimeter wave chipless RFID tag sensor reader by Islam [50]. The proposed antenna operated over the 22 GHz-27 GHz frequency band with total realized gain of 22 dBi. A 2 x 1, 4 x 1, and 8 x1 MPA array was proposed by Errifi [17]. The proposed designs operated at 11 GHz with realized gains of 9.93 dBi, 11.87 dBi, and 14.24 dBi respectively.

A 2 x 2 square dense dielectric patch antenna's gain and bandwidth were increased in [18] using a dielectric superstrate layer. The proposed antenna's size and thickness were improved but the antenna became bulky due to the study's use of two substrates. Paul et al [19], proposes changing the substrate material and thickness of the MPA operating at 2.4 GHz. Four different substrate materials RT Duroid 5880, GML 1000, RO4003, and FR-4 where proposed and investigated. Although the antenna's size was found to be reduced by the change in substrate material and thickness, the antenna's performance degraded. The bandwidth of a MPA was increased by using a thick substrate [20]. However, the increased substrate thickness caused the surface waves to be excited. The antenna gain is decreased because of these surface waves dispersing at the substrate edges. The MPA performance was enhanced by many researchers employing shorting pins. In [51], a multiple layer phase shifter was proposed and fabricated. At resonance frequency of 3 GHz, the structure exhibits a phase shift of 274^0, leading to an FoM of 37.3^0/dBi. By using a shorting pin and meandering the patch antenna, Wong et al. [52] were able to reduce the antenna's dimensions by 10%. However, a reduction in the antenna gain was observed. If the shorting pin is not placed close to the MPA feedline, the antenna's impedance matching may also be impacted. Consequently, a rise in input impedance is produced. In [53], the bandwidth of a patch antenna was enhanced by loading shorting pins with the transmission line model. Similarly, the gain of a single-fed MPA was improved by loading the patch with shorting pins [54].

Lo et al [55] utilized a high permittivity substrate to enhance the gain of an aperture coupled MPA. Tang et al [56] used a high permittivity substrate enhanced the MPA's axial ratio bandwidth. However, the loss of surface waves was caused using a high permittivity substrate. Numerous researchers have also investigated adjusting the patch shape to improve the MPA restrictions. The ground plane dimension and shape of a circular patch was adjusted in [57]. It was observed that as the gain of antenna was small and as the ground plane size increases, the main beam of the antenna became narrower, and the radiation rapidly decreases. The radiation and bandwidth of the MPA was shown to improve by 90% and 4 %, respectively when the patch of the antenna was folded [58]. The use of multiple substrates was proposed and investigated in [59]. The bandwidth of the antenna was increased by 20% and return loss of -25 dBi was achieved. However, fabricating such antennas might be complex.

In recent years, the loading of the MPA with artificially engineered material have been studied and investigated by various researchers. These artificially engineered materials include electromagnetic bandgap structures (EBG), highly reflective surfaces (HRS), dielectric slabs, artificial magnetic conductor (AMC), and metamaterials [60-71]

The feasibility of using EBG structure for gain enhancement in MPA was investigated by Alnaiemy and Nagy [64]. In [65], an integrated sievenpiper EBG substrate was used for the gain enhancement. A dual layered ultra -wideband hexagonal shaped MPA with an EBG was presented in [66]. The antenna operated at a UWB 5.1 -19.7 GHz with realized gain of 5.7 dBi. The bandwidth of circularly polarized (CP) antenna was enhanced by using a single layer reflective surface in [67]. A wideband (CP) antenna with reflective surface was proposed and demonstrated by Zhou et al in [68]. A gain and bandwidth improvement were achieved when a single dielectric superstrate was etched over a MPA in [69]. Bahari et al [70], proposed the use of AMC to improve the gain of a patch antenna. The AMC was placed between two dielectric substrate Rogers RT5880, the antenna operates at 16 GHz with a gain improvement of 16.3%. Similarly, a 20 x 20 x 2.4 mm^3 MPA was loaded with an 8 x 8 array unit cell of an asymmetric AMC as it ground plane [71]. An improvement in the gain and directivity of the MPA was observed.

2.9 Metamaterials

Metamaterials (MeTMs) are materials that have been engineered to display distinct electromagnetic properties. Rather than being distinctive due to their composition, these materials often have artificially engineered structures that contain inhomogeneities that support the effective macroscopic behavior. When designing a MeTM structure, the effective permittivity and permeability are the primary factors considered [22,72]. Mandel'shtam and Veselago introduced the Left Hand Medium (LHM) materials, which displayed negative permittivity and permeability, in 1945 and 1968, respectively [25,73]. The electromagnetic assets such as reverse of Snell's law, the Vavilov-Cerenkov's effect and Doppler's law were demonstrated by Veselago [25]. The general characteristics of EMW propagation in such materials were also presented. Pendry et al. [74] introduced a metallic framework with negative permeability which can also be referred to as split ring resonator (SRR) in 1996. He also developed metallic SRR, a non-magnetic structure, in collaboration with other researchers [75].

Additionally, Smith et al. [76] implemented Pendry's suggested SRR on a printed circuit board (PCB) in 2000 by integrating it with a set of metallic strips. Both the magnetic permeability and the electric permittivity were retrieved and examined. MeTMs based on transmission lines were proposed by Iyek et al. [77] and Caloz et al. [78]. Many researchers have utilized the Drude-Loentz model to demonstrate that materials exhibit the negative refractive index (NRI) precisely above each resonance while having little losses [79].

Benosman et al. introduced a MeTM structure with a double S-shape and dimensions of 4x4mm^2 that operates in a frequency band of 15.63 GHz [80]. The structure exhibits permittivity and permeability in the range of 15.63 GHz to 17.8 GHz, and the negative refractive index lies between 15.67 to 17.43 GHz. Aznabet et al. proposed a MeTM antenna with dimensions of 30x22x0.8 mm^3 that operates at a single band [81], but the properties of its unit cell were not discussed or validated. Malik et al. designed a novel two-rectangular U-shaped negative MeTM with dimensions of 25 x2 5x 1 mm^3 for various orthogonal structures [82]. The structure was made using a glass substrate, gold plate, and thin-plate graphite and had operating frequencies in the range of 5 to 7 GHz. Alam et al. presented an Aztec

shaped MeTM structure with dimensions of 11 x 12x 1.6 mm^3, which was made using FR-4 as the substrate material [83]. It operates in the frequency range of 6.3, 8.9, 11.91, and 16.42 GHz.

Ekmekei et al. [84] proposed a V-shaped MeTM, while Jain et al. [85] provided an I-shaped MeTM antenna with dimensions of 12.5 x1 2.5 mm^2. The structure, which is etched on a 5 x 5 x 0.25 mm^3 fused quartz substrate, resonates between 5 and 15 GHz. At 8.10 GHz, it exhibits double-negative characteristics. Dhouibi et al. introduced a Z-shaped MeTM for an operating frequency of 4.5 GHz [86], but it has only been verified for single-negative properties with negative permittivity. A. M Tamim et al. presented an inverse double-L-shaped structured MeTM etched on a Roger RT5880 dielectric substrate [87]. The structure exhibits a triple-band frequency operation in C-, X-, and K_u- bands through different array arrangements.

Additionally, Hossain et al. developed a "C-shaped" split circular resonator with dimensions of 12 x 12 x 1.635 mm^3 on a Roger RT6010 dielectric substrate with a thickness of 0.035mm [88]. Islam et al. proposed a 30x30mm^2 split H-shaped MeTM structure [89]. The effective negative permittivity, permeability, and refractive index were verified over the frequency bands of 2.74, 7.122, 10.855, and 14.337 GHz, respectively. A. M. Siddiky et al. proposed an inverse double C-shaped SSRR MeTM [90], which has a multi-resonant frequency operating at a frequency range of 2.47 to 12.60 GHz.

On this, numerous and improved applications of MeTMs have proposed recently. The use of MeTMs have been utilized to improve the performance of surface plasmon resonance sensors instead of metallic components [91]. Also, MeTMs have been utilized to improve and enhance the parameters of MPAs. These parameters include but not limited to gain and bandwidth efficiency of the antenna [62,92,93]. The Complementary SRRs (CSRRs) and SRRs inspired by metamaterials are the most widely used options for ultra-wideband antenna technology, particularly in band rejection for narrow band interference [94]. The metamaterial SRR and CSRR can take on square, rectangular, and circular geometries.

A metal ring with its magnetic field polarized parallel to the surface and positioned in an EMW that is oscillating makes up the SRR. When the magnetic field intensifies the current in the ring, a magnetic flux perpendicular to the external magnetic field is produced. The metallic ring also includes a gap to provide resonance properties, which lead to capacitance. Due to the split in the rings, the moving current

builds up charge across the gap, which is then stored as capacitance. The capacitance is assimilated more efficiently when two rings are placed side by side with gaps on either side of one another. The SRR can be portrayed as an LC equivalent circuit due to its response to the external field as a quasi-static LC circuit [95]. Figure 2.10 illustrates the equivalent circuits for the SRR and CSRR unit cells.

(a)

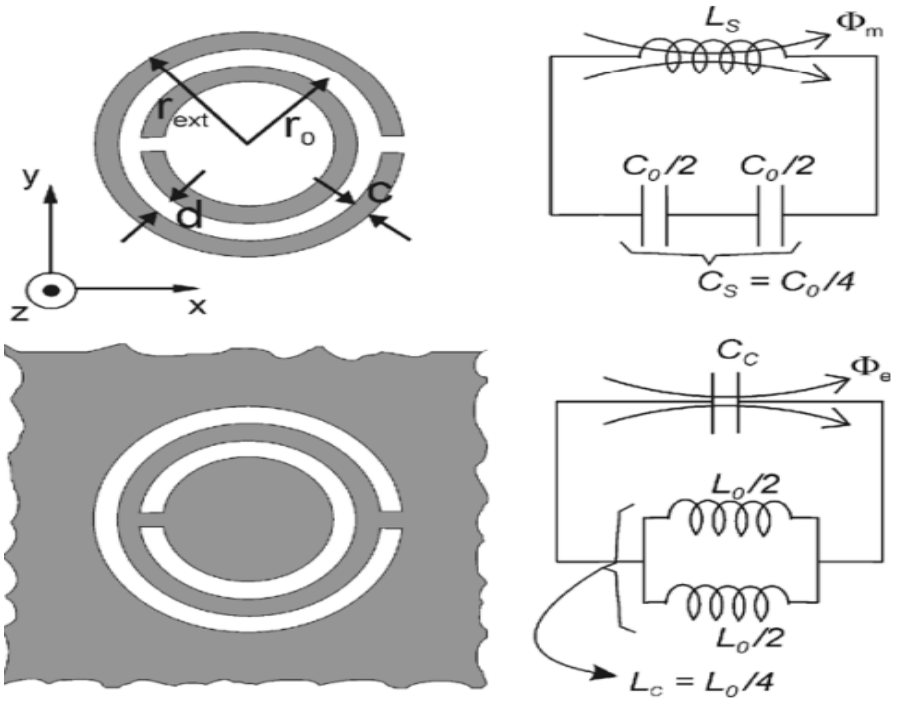

(b)

Figure 2.10: Circular and Rectangular SRR Unit Cell (b) SRR and CSRR with its Equivalent Circuits [72,95].

2.9.1 Classification of MeTMs

The electromagnetic characteristics of materials are categorized based on medium properties. The classification of MeTM according to permittivity (ε) and permeability (μ) values is shown in Figure 2.11. The first quadrant depicts Right-Handed Material, also known as Double-Positive Material (DPS), which has both positive values of ε and μ.The composite material that has permittivity and permeability values that are less than zero falls in the third quadrant and is commonly referred to as Left-Handed Material (LHM), Double-Negative Material (DNG), or Negative Refractive Index Material (NRIM), while other materials that only have one value of permittivity or permeability that is less than zero are known as Single-Negative Materials (SNG), and they can be found in the second quadrant or fourth quadrant. Epsilon-negative (ENG) and mu-negative (MNG) materials have permittivity values that are less than zero and permeability values that are less than zero, respectively [96,97].

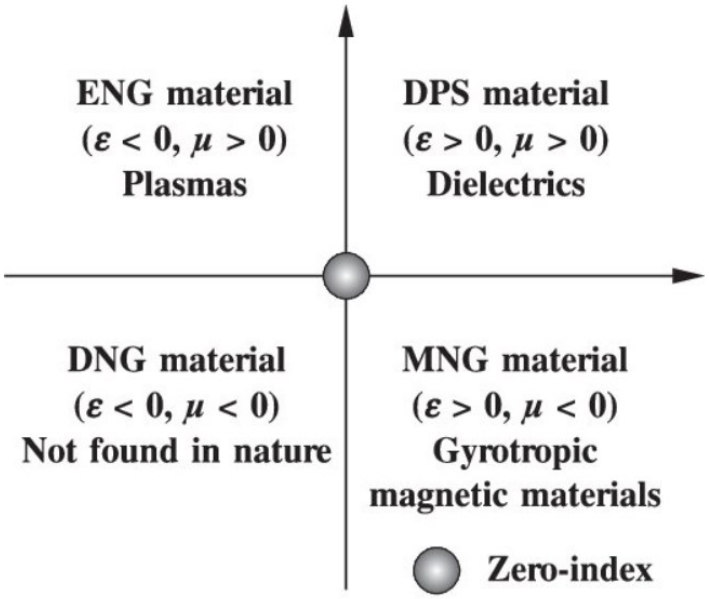

Figure 2.11: Classification of Metamaterials [86].

2.9.2 Left-Handed Material

Left-handed material (LHM) was first produced in 1968 by Veselago [25]. He asserted that such a medium exists, in which the wave vector (*K*), magnetic field $(\vec{H})$, and electric field $(\vec{E})$ are denoted by the thumb and index finger of the left hand, respectively. If the middle finger is placed normal to both

fingers, it then provides the directions of the wave vector's phase changes of $\left(k = \omega\sqrt{(\varepsilon)} * \sqrt{\mu}\right)$. The energy flow $\bar{P}_{av} = 0.5Re\left[\vec{E} \times \vec{H}\right]$ in a LHM medium [98,99]. The LHM have been referred to as negative index materials (NIMs), double negative materials (DNGs), and negative refraction index (NRI). The LHM has a negative refraction index because, over a given frequency range, it also has a negative permittivity (ε), permeability (μ), and refractive index (n). The wave propagation of the LHM is shown in Figure 2.12.

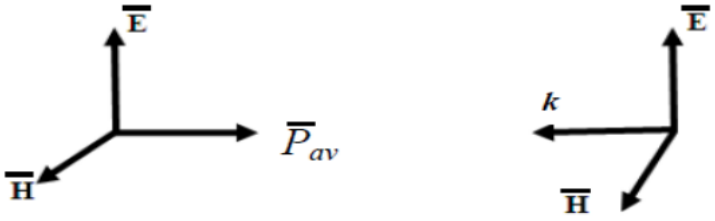

Figure 2.12: Wave Propagation of LHM [88].

To illustrate wave propagation in the LHM, we will first transform Maxwell's equation into the wave equation [24].

$$\left(\nabla^2 - \frac{n^2}{c^2}\frac{\partial^2}{\partial_t{}^2}\right)\psi = 0, \tag{2.25}$$

Where represents *n* and *c* the refractive index and speed of light in a vacuum, respectively. Due to the concurrent modification in sign n ε and μ, the refractive index n^2 is unaffected. Then, the explicit form of the Maxwell's first order differential equations is [100,101]

$$\nabla \times \vec{\boldsymbol{E}} = -j\omega\mu\vec{\mathbf{H}} \tag{2.26}$$

$$\nabla \times \vec{\mathbf{H}} = -j\omega\varepsilon\vec{\mathbf{E}} \tag{2.27}$$

The differences between Equations (2.26) and (2.27) are evident. The derived equations for planar waves are as follows:

$$K \times \vec{\boldsymbol{E}} = \omega\mu\vec{\mathbf{H}} \tag{2.28}$$

$$K \times \vec{\mathbf{H}} = -\omega\varepsilon\vec{\mathbf{E}} \tag{2.29}$$

As a result, $\vec{E}, \vec{H}$ and K form a right-handed orthogonal system of vectors for positive values of ε and μ. Therefore, if $\varepsilon < 0$ and $\mu < 0$, then equations (2.28) and (2.29) can be rewritten as:

$$K \times \vec{\boldsymbol{E}} = -\omega|\mu|\vec{\mathbf{H}} \tag{2.30}$$

$$K \times \vec{\mathbf{H}} = -\omega|\varepsilon|\vec{\mathbf{E}} \tag{2.31}$$

The condition in equations (2.30) and (2.31) shows that $\vec{E}, \vec{H}$ and K forms the left-handed triplet.

Equations (2.30) and (2.31)'s condition demonstrates that the left-handed triplet consists of $\vec{E}, \vec{H}$ and K.

2.10 Applications of Metamaterial

The electromagnetic properties of the MeTM such as permittivity, permeability, and arbitrary propagation constant are quite impossible to get using conventional materials. The metamaterial has a wide range of application [72,102]. These applications include imaging systems [103-105], absorbers [106-108], sensors [109,110], filters [111,112], multi-band elements [113], reduction of specific absorption rate [114] electromagnetic visibility cloaks [115, 116], couplers [117], and antennas [118-123].

2.11 Metamaterial in Antenna Design

Metamaterial based antennas are class of antenna which uses the MeTM to optimize antenna system performance. The antenna utilizes MeTMs to boost both the radiated power and the gain enhancement, bandwidth enhancement and miniaturization of MPA using MeTM loaded on or near the patch, placed at the ground plane, embedded in the substrate, or etched as a superstrate above the radiating patch. The MeTM can also be employed in MIMO antenna systems to help increase isolation caused by mutual coupling [124-126].

2.11.1 Bandwidth Enhancement

Apart from antenna miniaturisation, the demand for wide bandwidth in wireless communication have grown tremendously in recent years. several literatures offered a variety of approaches for

improving the antenna's bandwidth, including the use of vias, parasitic elements, modified ground planes [127-129]. Although these approaches enhance radiation properties, they do so at the expense of added complexity. The use of MeTM with the patch antennas provides an easy way to fabricate these antennas as MeTMs can be fabricated on the substrate. The MeTM unit cell introduces resonance, enhancing the MPA's bandwidth. An ultrawideband antenna with a planar MeTM structure was proposed in [130]. The adjustment in the ground plane causes the proposed structure to emit more energy. The proposed antenna covers the frequency range of 3.1 GHz to 10.6 GHz with a wide bandwidth range of 3.06 GHz to 36.4 GHz and a gain of 8.02 dBi. The proposed antenna has a mesh-shaped radiating patch and a ground plane with a defect of a cross-shape of 2 x 2 mm^2 FR-4 substrate with dimensions of 32 x 28 mm^2.

A 4 × 4 array of the modified SRR structure was loaded onto a dual-band antenna that was partially grounded [131]. The antenna's bandwidth was improved by 16% and 6%, respectively, at operating frequencies of 2.36 GHz and 8.5 GHz, without compromising the antenna's performance. A 31 x 24.57 x 1.6 mm^3 coplanar waveguide (CPW) fed monopole antenna with SRR loaded at the back of its dielectric substrate was proposed in [132]. The MeTM unit cell enhanced the bandwidth of the antenna by 48%. A 2 × 2 mm2 circular array of MPA with a bioplastic-backed, ceramic-filled low loss substrate was presented in [133] for use in WLAN, WiMAX, RFID, and UHF applications. A two-sided reflective metasurface was placed above the radiating patch and a significant bandwidth of 178% to 240% was attained. In [134], a patch antenna was designed using non-uniform patches, stair-shaped aperture and CPW feeding. An increased bandwidth of 67.3% and gain of 9.18 dBi was obtained. In [135], the bandwidth of MPA was increased by introducing a complementary Split Ring Resonator (CSSR) structure between the substrate's ground and patch. The antenna at 2.4 GHz achieved a bandwidth increment of 800 MHz. Thus, it was established that the metamaterial provided a 1 dBi improvement.

2.11.2 Gain and Enhancement

Low profile antennas experience performance deterioration in terms of radiation properties such as gain and efficiency in wireless communication applications. For a multiband antenna, this issue even gets worse, especially in lower frequency bands [93]. The gain performance of a low profile MPA was

enhanced by a triangular SRR metamaterial was investigated in [136]. The antenna operate at a frequency of 10.667 GHz and the gain was increased from 6.5 dBi to 11.5 dBi. The performance of the MPA exhibited a notable improvement. In [137], K. K. Naik proposed a dual antenna loaded with meandering line and SRR. The antenna resonated at 2.48 GHz and 3.49 GHz frequencies. However, the antenna's structure grew intricacy and size. Gain and bandwidth were increased by 680 MHz and 8 dB, respectively. An 18 x 22 mm^2 millimeter -wave MPA with vertically coupled split ring metaplate was presented in [138]. The proposed antenna achieved a good radiation with a gain of 11.94 dBi and bandwidth ranging 26.58 – 29.31 GHz. The gain of MPA was enhanced when square SRR metamaterial superstrate was loaded over the patch of the antenna [139]. The proposed antenna radiates at 5.5 GHz, with an increased gain from 3.7 dBi to 5 dBi respectively. A novel 2 x 2 MeTM superstrate was presented in [140]. The proposed operates at 2.4 GHz with a maximum gain of 3.5 dBi.

2.11.3 Miniaturization

Compact antennas are becoming more and more popular as portable wireless devices become more common. Extreme care must be taken while developing an antenna for one of these devices to guarantee that it will function as required because an antenna's radiating properties may be compromised as it becomes more compact. A complimentary SRR that is positioned planar to a T-shaped patch was investigated in [141] shifted the antenna's resonance frequency from 2.64 GHz to 2.45 GHz, resulting in a 7.75% size reduction. The proposed antenna is electrically compact due to the increase in the surface current of the radiating patch, which is made possible by an increase in the overall inductance and capacitance from rings. A double negative modified SRR loaded on the ground plane of a partial ground plane monopole antenna is presented in [142]. By enhancing the mutual coupling between the MeTM element and the unloaded monopole antenna, a 13.15 % decrease was attained in antenna dimension. A MPA with an operating frequency of 3.6 GHz had its ground plane etched with a 3 x 4 array of a modified complimentary ELC MeTM in [143]. The frequency of the proposed antenna reduced from 3.6 GHz to 2.67 GHz, causing an antenna miniaturization of 25.83%. In [144], the size of the radiating patch was reduced by 67% without compromising the performance of the antenna, when two metasurface layers made of complimentary rectangular unit was used in the design.

The characteristics of the MPA, such as improved bandwidth, gain, reflection coefficient, directivity, and radiation patterns, have been the subject of extensive investigation. It is important to note that no single type of conventional patch antenna can meet the evolving demands of recent wireless communication systems. However, it has been demonstrated that when compared to traditional MPAs, metamaterial-inspired antennas significantly enhance the MPA's performance. The MeTM structures examined in the aforementioned literatures have demonstrated compact sizes, and only a small number have also demonstrated multi-band characteristics. In Chapter 3, Table 3.4, a thorough comparative examination of these structures is provided. The MeTM structure described in this thesis has a novel structure and is created on an inexpensive FR-4 dielectric substrate with a compact design of 10 x 10 mm^2. By producing seven resonant frequencies, the MeTM unit cell demonstrates multi-band characteristics.

The metamaterial-based antennas covered in this section have also demonstrated improved gain, bandwidth, and size reduction. In Chapter 4, Tables 4.6 and 4.13 provide a thorough comparison of various antennas. It is noted that most of the investigated antennas only produce minimal gain and operate on a single frequency. The proposed antenna in this research shows a triple operational band and exhibits a very high gain improvement. It has been designed on the inexpensive FR-4 material.

2.12 Parameter Extraction Methods

The effective parameters, permittivity, and permeability are crucial for MeTM's performance. However, it might not be possible to directly retrieve these parameters. Several extraction techniques have so far been reported in literatures [96,145]. These techniques allow for the evaluation of permittivity and permeability, and most of MeTM exhibits anisotropic behavior. The Nicolson-Ross-Weir extraction technique, which is the most used, was covered in this chapter.

2.12.1 The Nicolson- Ross-Weir Technique

The Nicolson-Ross- Weir (NRW) technique is based on measuring the reflection S_{11} and transmission S_{21} coefficient of a MeTM slab, to calculate the effective permittivity (ε_r), magnetic permeability (μ_r),

and the relative refractive index (η_r) [146]. The Scattering parameters for the impedance (Z) and the refractive index can be expressed by [91]

$$S_{11} = \frac{\Gamma\left(1 - e^{j2\eta_r k_0 S_h}\right)}{1 - \Gamma^2 e^{j2\eta_r k_0 S_h}} \tag{2.32}$$

$$S_{21} = \frac{(1 - \Gamma^2) e^{j2\eta_r k_0 S_h}}{1 - \Gamma^2 e^{j2\eta_r k_0 S_h}} \tag{2.33}$$

We can express $\Gamma = \frac{Z_0 - 1}{Z_0 + 1}$, k_0 denotes the wave number of the incident wave in free space, Z_0 is the impedance and S_h is the substrate length/ thickness of the unit cell. equations (2.32) and (2.33) can be rewritten as

$$S_{11} = \frac{(1 - \Gamma^2)\, Z}{1 - \Gamma^2 Z^2} \tag{2.34}$$

$$S_{21} = \frac{(1 - Z^2)\, Z}{1 - \Gamma^2 Z^2} \tag{2.35}$$

From equations (2.34) and (2.35),

$$V_1 = S_{11} + S_{21} \tag{2.36}$$

$$V_2 = S_{21} - S_{11} \tag{2.37}$$

The effective parameters of the MeTM planar unit cell structure are given as [147, 148]

$$\varepsilon_r = \frac{2}{j\pi f s_h} \times \left(\frac{1 - V_1}{1 + V_1}\right) \tag{2.38}$$

$$\mu_r = \frac{2}{j\pi f s_h} \times \left(\frac{1 - V_2}{1 + V_2}\right) \tag{2.39}$$

$$\eta_r = \frac{2}{j\pi f S_h} \times \sqrt{\frac{(S_{21} - 1)^2 - {S_{11}}^2}{(S_{21} + 1)^2 - {S_{11}}^2}} \tag{2.40}$$

$$\eta = \frac{1}{k_o s_h}\left\{\left[\left[In\left(e^{j\eta_r k_{os_h}}\right)\right]\right] + 2m\pi - j\left[In\left(e^{j\eta_r k_o s_h}\right)\right]\right\} \tag{2.41}$$

where,

$$e^{j\eta_r k_o s_h} = \frac{S_{21}}{1 - S_{11}\frac{Z-1}{Z+1}} \tag{2.42}$$

where *f* is the operating frequency. Equations (2.32) – (2.42) have been used to analyze the scattering parameters of the MeTM unit cell.

2.13 Methodological Approach

The literatures reviewed in this chapter serve as a guide in performing theoretical design of MPA and the proposed MeTM structure. This is carried out to ensure the design correspond and align with the expectation of theory. By utilizing simulations and design to perform any necessary alterations to improve the overall antenna performance, the CST microwave studio has helped in the design and optimization of the theoretical studies that have been developed. This approach will assist in establishing a validation of the theoretical aspect regarding the practical application.

2.14 Chapter Summary

In this chapter, the introduction to antennas, antenna parameters, MPAs, feeding techniques, the design criteria for MPA etc. have been discussed. Various approaches to improving the antenna performance have also been presented. A brief review of the history of metamaterials, and its classifications are presented in this chapter. The theoretical information of metamaterial, applications, as well as its effective parameters have also been presented. The metamaterial is employed in the enhancement of the MPA performance such as bandwidth, improvement, gain enhancement, minimization of antenna structure etc. Lastly, the methodological approach for the simulation, fabrication of the antenna is discussed.

CHAPTER 3

I-Shaped Metamaterial Using SRR for Multi-Band Wireless Communication

3.1 Introduction

In this chapter, the design and analysis of a novel I-Shaped Metamaterial (ISMETM) structure is presented. The MeTM is designed and simulated on the FR-4 dielectric substrate with a dielectric constant and height of 4.3 and 1.6 mm respectively metallic copper rings with thickness of 0.035 mm. The geometry, theoretical model and equivalent circuit, and design methodology of the proposed metamaterial unit cell is presented. A comprehensive analysis of 1 x 2, 2 x 2, and 2 x 4 array of the proposed MeTM is also investigated. The design and simulation of the MeTM is carried out using the CST Studio Suite and MATLAB while the equivalent circuit of the unit cell is designed using the Advance Design System (ADS) software.

3.2 MeTM Unit Cell Geometry and Design

The geometrical configuration of the proposed ISMeTM unit cell and its simulated model are illustrated in Figure 3.1. A perfect electric conductor (PEC) is used for the metallic part, and it is designed on the FR-4 dielectric substrate. The dielectric constant and loss tangent ($tan\delta$) of the FR-4 substrate material are 4.3 and 0.025, respectively. The thickness of the substrate and the thickness of the annealed copper used for the SRR are 1.6 mm and 0.035 mm, respectively. The primary function of splits in the ring resonators is to ensure that the inductance and capacitance interact with one another to determine the operating frequency. The unit cell's total optimum size is $10 \times 10 \times 1.6$ mm^3 (sw × ls × s_h). The parameters of the ISMeTM unit cell are presented in Table 3.1. The configuration and the comprehensive analysis of the MeTM properties is carried out using the Finite Integration Technique (FIT)-based electromagnetic CST simulator.

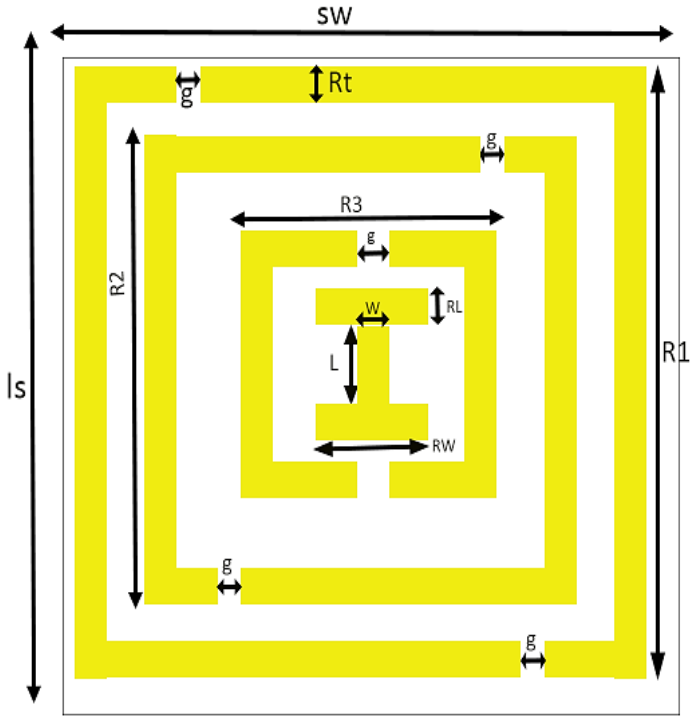

(a)

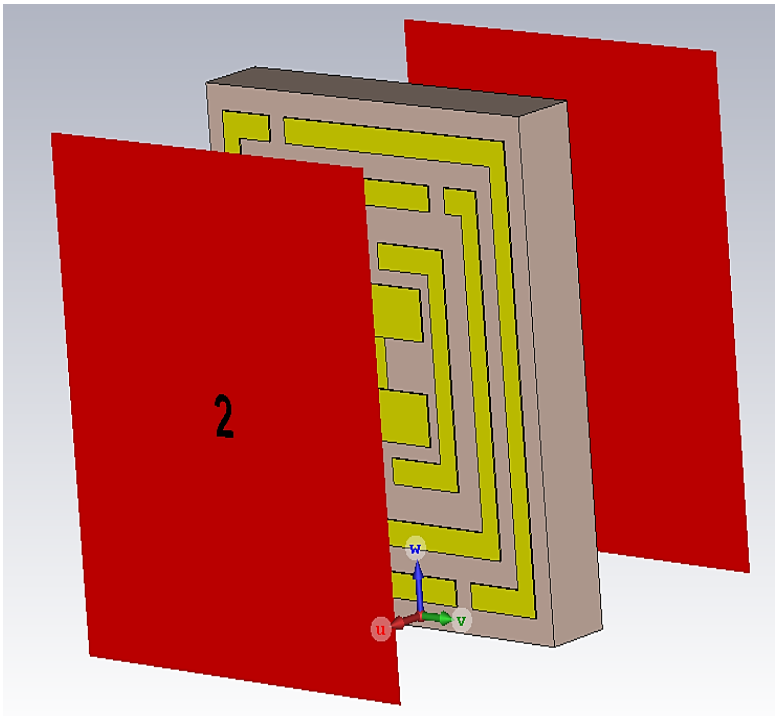

(b)

Figure 3.1: Proposed ISMeTM (a) Unit Cell Configuration, (b) Simulated Model.

Table 3.1 Parameters of the ISMeTM Unit Cell

Parameter	Dimension (mm)	Parameter	Dimension (mm)
Sw	10	Rw	1.25
Ls	10	L	0.5
R1	9	W	0.5
R2	4	g	0.5
R3	2.8	sh	1.6
Rt	0.5	ch	0.035
Rl	2	tw	0.5

3.3 Theoretical Model and Equivalent Circuit of the ISMeTM

The proposed ISMeTM metal structure was designed on an FR-4 dielectric substrate layer. The time-varying EM field changes over time. The electron density engulfs the MeTM structure. Metal bars have been used to enhance the formation of a new distinct electromagnetic wave. The sensing response is handled by the metallic ring, while the split gap between the rings provides a strong electric field for the design. The transmission line approach was utilized to analyse the ISMeTM unit cell, which allows an individual strip or patch to duplicate an RLC series circuit. The passive LC circuit is connected to the resonance frequency. The equivalent circuit of the proposed ISMeTM is presented in Figure 3.2 which consists of the capacitance- and inductance-generating resonance on the proposed ISMeTM unit cell.

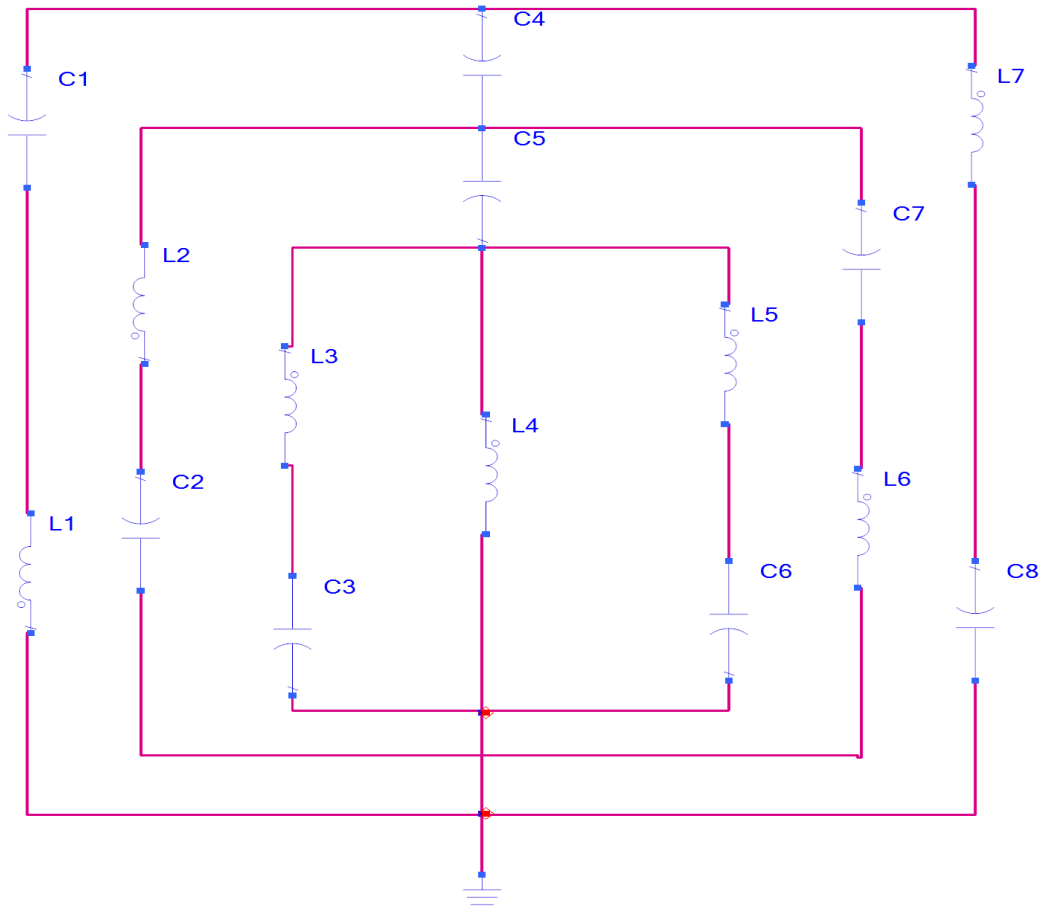

Figure 3.2: The Equivalent Circuit of the Proposed ISMeTM Structure.

The resonance frequency (f_{re}) is expressed as [149,150]

$$f_{re} = \frac{1}{2\pi\sqrt{L_E C_E}} \tag{3.1}$$

where L_E and C_E represent the inductance and capacitance of the structure, respectively. Similarly, the split ring's inner loop's gap functions as a capacitor, while the metallic ring itself functions as an inductor. The electric resonance in the structure is created by interaction of the split ring and electric field while the interaction of magnetic fields with metallic loops during EM propagation in the structure causes magnetic resonance. The total capacitance between the ring gap (C_g) can be defined as the capacitor of the parallel plate (C_{pl}) which compensate for the fringing field by extending the parameters plate width and thickness and is expressed as [151]

$$C_g = \varepsilon_0 \frac{hw}{g} + \varepsilon_0(h + w + g) \tag{3.2}$$

$$C_g = C_{fringe} + C_{pl} = \varepsilon_0 \left[\frac{(h+g)(w+g)}{g}\right] \tag{3.3}$$

where ε_0 denotes the free space permittivity, h, w, and g represent the height, width, and gap of the ring, respectively. The inductance of the SSRR can be derived from the inductance of a rectangular loop [152]. By using a rectangular cross-sectional area with the conductor of a rectangular loop [153], we have

$$L = \frac{\mu_0}{\pi}\left\{ \begin{array}{c} (h+w)\ \ln\left(\frac{2h\,\mathrm{w}}{h_c + w_c}\right) - \ h\ln\left(h + \sqrt{h^2+w^2}\right) - w\ln\left(h + \sqrt{h^2+w^2}\right) - \frac{h+w}{2} \\ +2\sqrt{h^2+w^2} + 0.447(h_c\ + w_c\,) \end{array} \right\} \tag{3.4}$$

where h and w are the height and width of the rectangular loop, respectively. h_c and w_c denote the height and the width of the conductor's cross section, respectively. The length and the width of the SSRR for the proposed ISMeTM structure R_1 and $R_t\ = R$, and the weighting factor $\rho_e = 1 - g/4R$ Equation (3.4) is used to analyze the perimeter of the SSRR. By rewriting Equation (3.4) we have

$$L = \rho_e \frac{\mu_0}{\pi}\left\{2R\ln\left(\frac{2R^2}{h_c + w_c}\right) - 2R\ln\ \left[R\left(1+\sqrt{2}\right)\right] - R + 2R\sqrt{2}\ + 0.447(h_c + w_c)\right\} \tag{3.5}$$

The parameter values for μ_0 and ε_0 are $8.854 \times 10^{-12}\,F/m$ and $4\pi \times 10^{-7}\,H/m$, respectively. In the equivalent circuit presented in Figure 3.2, C1, C2, C3, C4, C5, C6, C7, and C8 are the capacitors, and L1, L2, L3, L4, L5, L6, and L7 are the inductors. The circuit is designed using the ADS software.

3.4 Design Methodology

In microwave communication application, various factors must be considered to provide multi-band operating frequencies. To increase the efficiency and effectiveness of the design for the proposed ISMeTM structure, the configuration is optimized using CST microwave studio. An iterative approach is used to obtain the response of the ISMeTM unit cell. Hence, modifying the resonance frequency is feasible by adjusting the dimensions and thickness of the substrate. However, because of the capacitance and inductance variation, some major parameters such as the length and width of the ring resonator, the

ring gap between the rings, spilt gap and the ring length are responsible for producing the multi-band operating frequencies. The design steps for the proposed ISMeTM unit cell are shown in Figure 3.3.

(a) (b) (c) (d)

Figure 3.3: Design Steps for the Proposed ISMeTM Unit Cell: (a) Design step-a, (b) Design step-b, (c) Design step-c, (d) Design step-d (ISMeTM).

The reflection coefficient, transmission coefficient and permittivity for various design steps are shown in Figure 3.4a–c, respectively. In design step-a, double copper wire cut was introduced into the outer ring. From the S21 graph, it can be observed that the resonant frequencies are 6.4, 10.02 and 11.82 GHz. A second copper ring is introduced to the unit cell and five resonances at 6.23, 7.81, 10.17, 11.98 and 14.68 GHz are realized for design step-b. A third copper ring is introduced into the structure in design step-c. This design produces six resonances at 6.32, 7.81, 9.98, 11.46, 12.21 and 15.67 GHz. In design step-d (ISMeTM), an I-shaped metallic structure is introduced into the internal ring of the unit cell. Furthermore, seven resonances are obtained at 6.31, 7.79, 9.98, 10.82, 11.86, 13.36 and 15.5 GHz. The parameters for various design steps are summarized in Table 3.2.

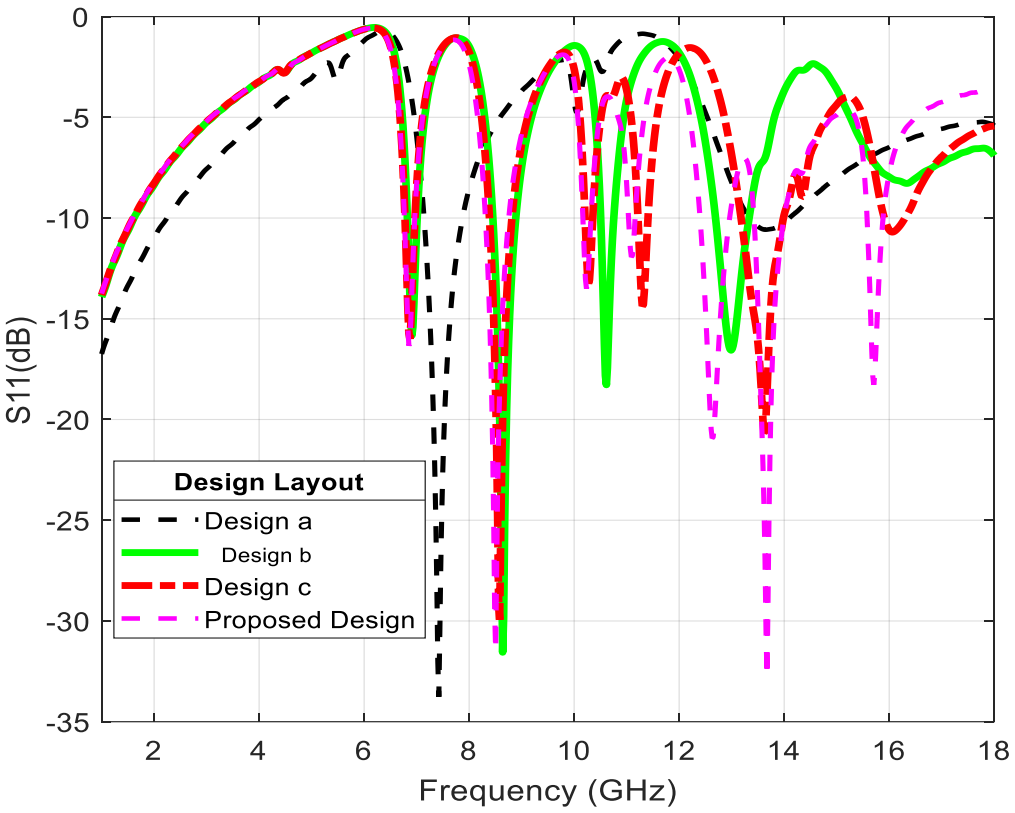
S11(dB)
Frequency (GHz)
Design Layout
Design a
Design b
Design c
Proposed Design

(a)

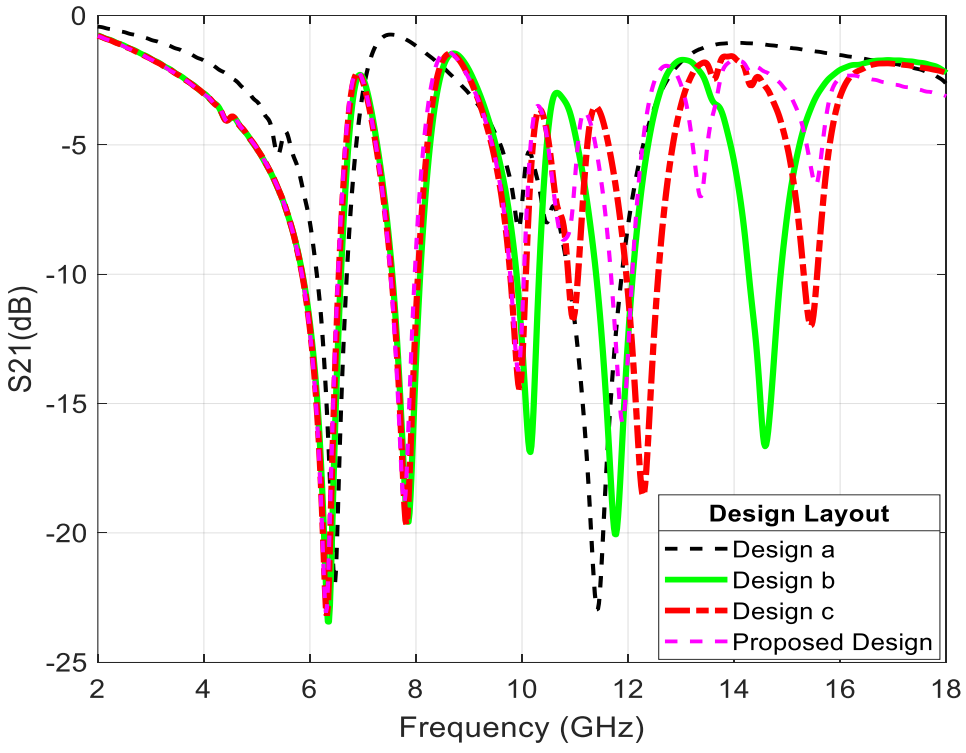
S21(dB)
Frequency (GHz)
Design Layout
Design a
Design b
Design c
Proposed Design

(b)

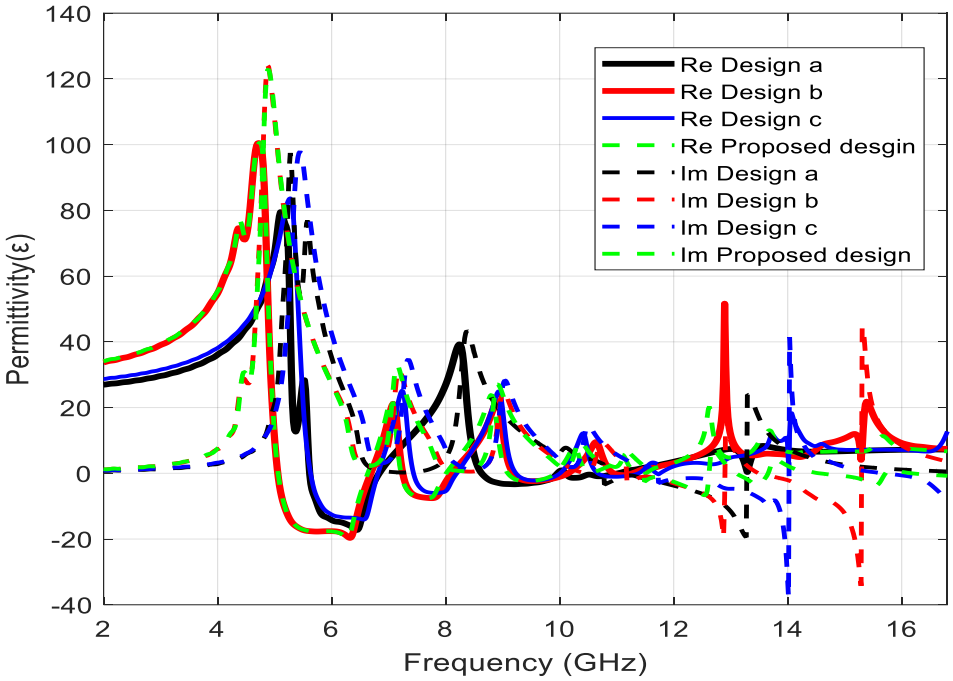

(c)

Figure 3.4: Reflection and Transmission Parameters of Various Configurations (a) S_{11}, (b) S_{21}, (c) Permittivity.

Table 3.2 Parameters of Various Design Steps

Design Layout	**Frequency (GHz)**	**S21 (dB)**
Design a	6.4, 10.02, 11.82	-21.99, -8.23, -22.96
Design b	6.23, 7.81, 10.17, 11.98, 14.68	-23.12, -19.53, -16.81, -19.97, -16.41
Design c	6.32, 7.81, 9.98, 11.46, 12.21, 15.67	-18.15, -16.14, -11.75, -7.34, -19.13, -8.32
Proposed design (ISMeTM)	6.31, 7.79, 9.98, 10.82, 11.86, 13.36, 15.5	-22.96, -18.89, -13.47, -8.64, -15.49, -6.87, -6.45

3.5 Methodology for Extracting the Unit Cell's Effective Medium Parameters

The effective parameters of the proposed ISMeTM unit cell can be determined by placing the structure between two waveguides (ports) such that the electromagnetic wave (EM) has magnetic field along the *y*-axis and electric field in the direction of the *x*-axis. Thus, the wave is propagated at the *z*-axis. This means that the first port acts as the reflecting signal's transmitting port, while the second port acts as the signal's receiving port. In addition, a tetrahedral mesh from frequency domain solver has been used for simulating the unit cell and array structure. The impedance has been set to 50Ω. The operating frequency range is from 2 to 18 GHz. Figure 3.1(b) shows the simulation arrangement of the proposed ISMeTM unit cell inside the waveguide. The ratio of effective medium depends on both the dimension of the unit cell and the wavelength, provided that the wavelength is less than the operating wavelength. The mathematical extraction model for extracting the effective medium parameters of the unit cell has been presented in Section 2.12 in the previous chapter.

3.6 ISMeTM Unit Cell Analysis

This section discusses the analysis of the proposed ISMeTM unit cell parameters. The Nicolson–Ross–Weir method has been used to extract the MeTM parameters. Detailed electromagnetic characteristic in terms of permeability, permittivity, relative index, and the scattering parameters of the MeTM are shown in Figure 3.5. The CST Microwave Studio software is used to investigate the performance of the proposed ISMeTM. The analysis validates that the effective magnetic permittivity (ε_r) is negative, the electric permeability (μ_r) is positive, and relative refractive index (η_r) is positive and negative within the same resonance frequency bands. As a result, these characteristics show that the proposed ISMeTM unit cell shows SNG metamaterial properties. The structure is designed to produce multi-band operation. Due to the compact nature of the ISMeTM, it can be utilized in antenna design for improving antenna performance. The proposed ISMeTM can also be used in satellite communications, Wi-Fi devices, weather radar systems, surveillance etc.

The S-parameters and the effective parameters of the proposed ISMeTM unit cell are presented in Figure 3.5(a), (b), respectively. The obtained simulated S_{21} parameter of ISMeTM shows the resonance frequencies at 6.31, 7.79, 9.98, 10.82, 11.86, 13.36 and at 15.5 GHz in the C/X/Ku-bands.

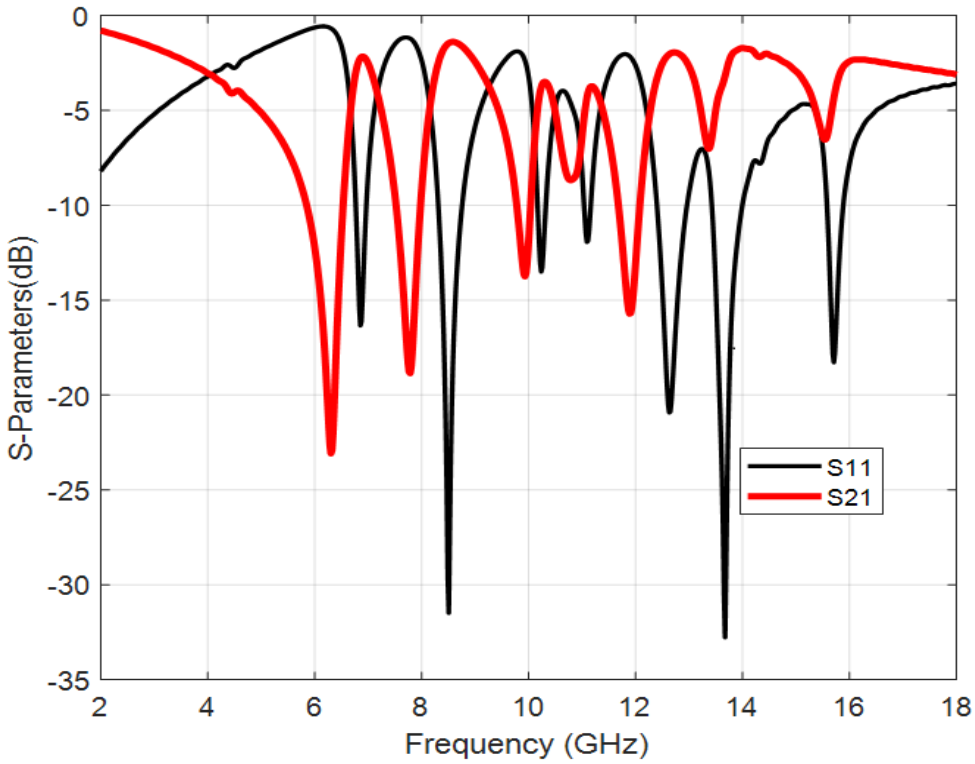

(a)

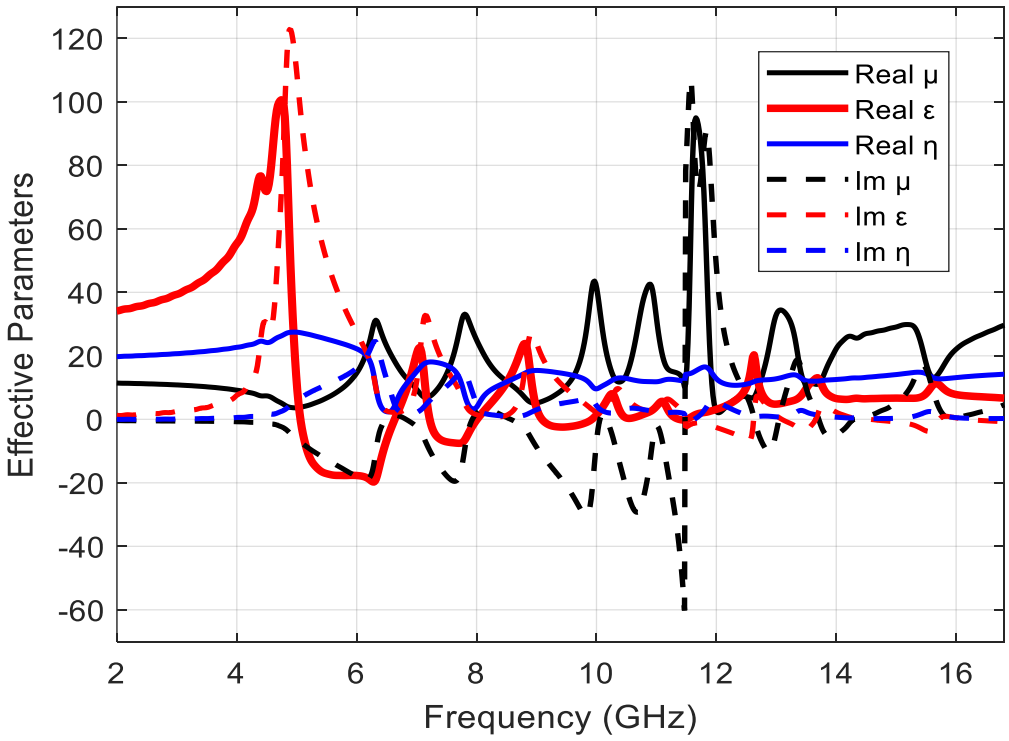

(b)

Figure 3.5: S-parameters and Effective Parameters of the ISMeTM (a) S- Parameter, (b) Effective Parameters.

Simulation of a time-dependent electromagnetic (EM) wave is the effective parameter utilized to measure the response of the MeTM cell design. Modifications in the geometric shape of the design can affect the permittivity and permeability characteristics. The real and imaginary values of the effective permittivity, effective permeability, and effective refractive index are shown in Figure 3.5(b). From Figure 3.5(a), it can be observed that the S21 shows the dips at 6.31, 7.79, 9.98, 10.82, 11.86, 13.36 and at 15.5 GHz. The 3-dB bands can be observed from the Figure 3.5a as 3.99–6.77 GHz (frequency band = 2.78 GHz, fractional BW = 51.67%), 7.07–8.27 GHz (frequency band = 1.2 GHz, fractional BW = 15.65%), 9.14–12.44 GHz (frequency band = 3.3 GHz, fractional BW = 30.58%), 13.01–13.70 GHz (frequency band = 0.69 GHz, fractional BW = 5.17%) and 15.04–15.83 GHz (frequency band = 0.79 GHz, fractional BW = 5.12%). The proposed structure shows the wideband operation and the maximum fractional bandwidth of 51.67% is achieved. Hence, the proposed structure can be used for wideband applications for different bands. From Figure 3.5(b) it can be observed that the ISMeTM produces the SNG characteristics for the frequency ranges 5.46–6.29, 11.6–11.8, 13.8–15 and 15.8–16.8 GHz. The analysis validates the following: the values of the effective electric permittivity (ε_r) are negative; those of the magnetic permeability (μ_r) are positive; and relative refractive index (η_r) are positive and negative within the same resonance frequency bands. As a result, these characteristics show that the proposed ISMeTM unit cell shows the MeTM properties. The proposed ISMeTM is useful for filtering applications, remote aerospace applications, electromagnetic cloaking devices which could be useful for military applications, etc.

3.7 Result and Discussion

The parametric analysis for the ring gap (g) is carried out and presented in Figure 3.6. This analysis provides a suitable dimension for the ISMeTM design. It can be observed from Figure 3.6(a) that when the dimension of the ring gap (g) is varied, the operating band changes. It can be observed that for g = 0.5 mm and 1 mm the MeTM have the same number of resonance frequencies, while at g =1.5 mm and 2 mm the MeTM have five and six resonance frequencies, respectively.

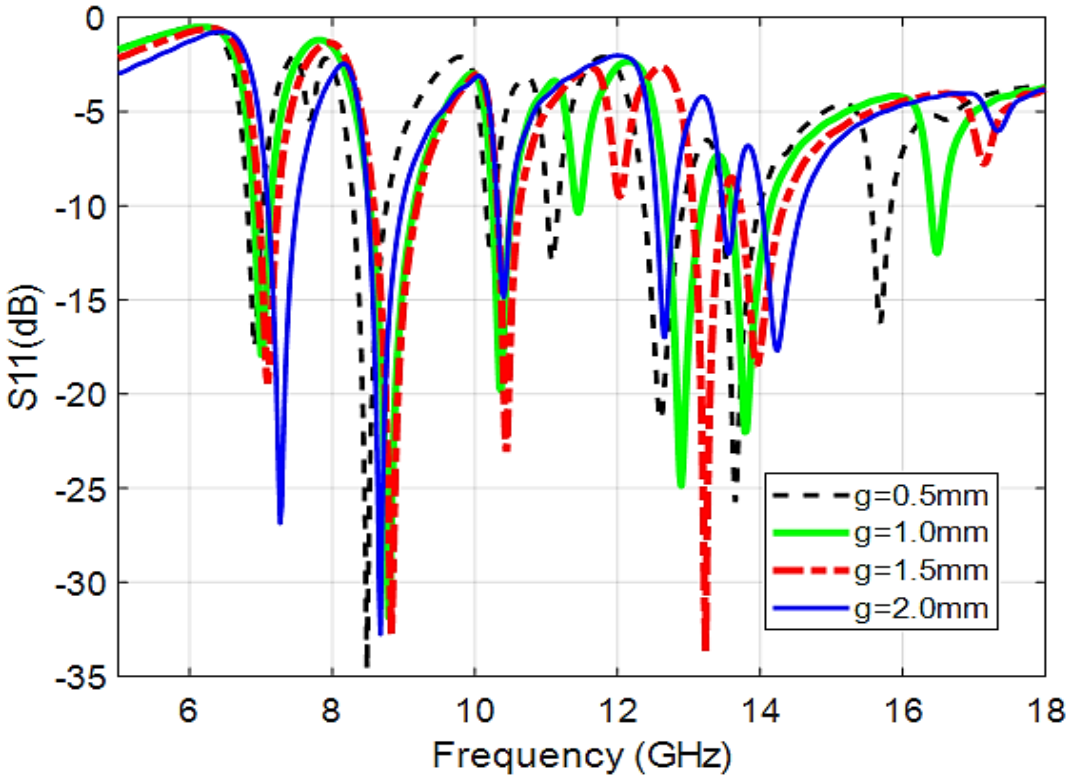
S11(dB)
Frequency (GHz)
g=0.5mm
g=1.0mm
g=1.5mm
g=2.0mm

(a)

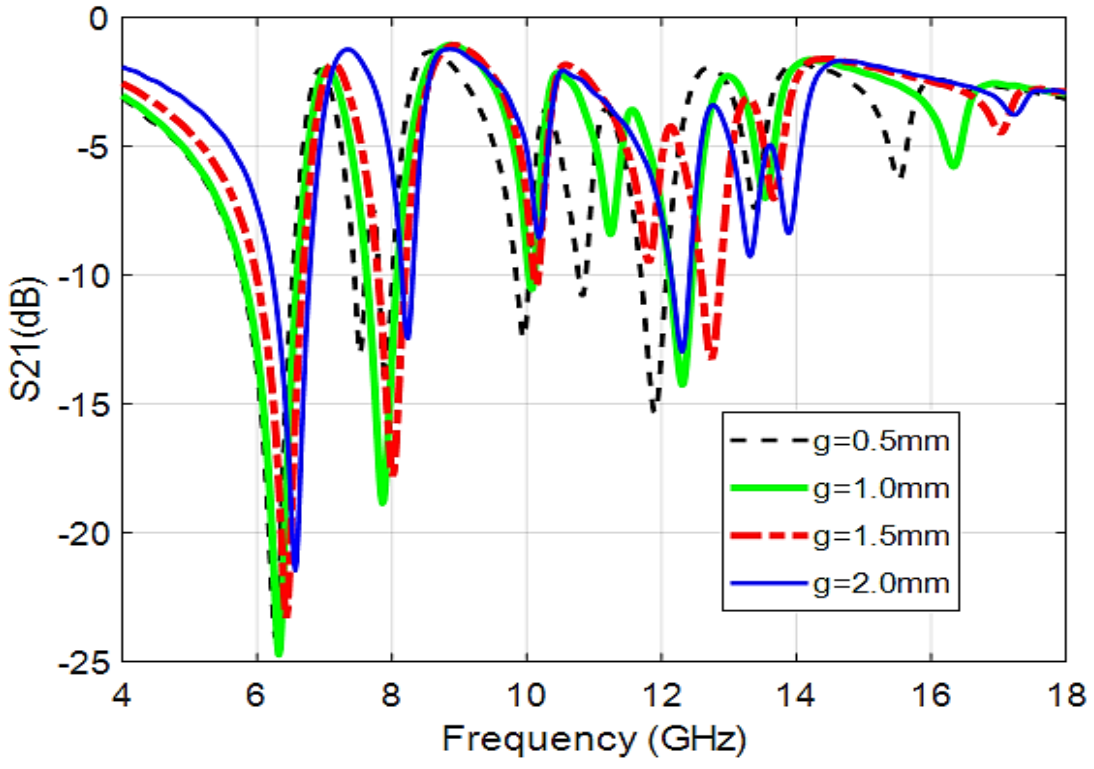
S21(dB)
Frequency (GHz)
g=0.5mm
g=1.0mm
g=1.5mm
g=2.0mm

(b)

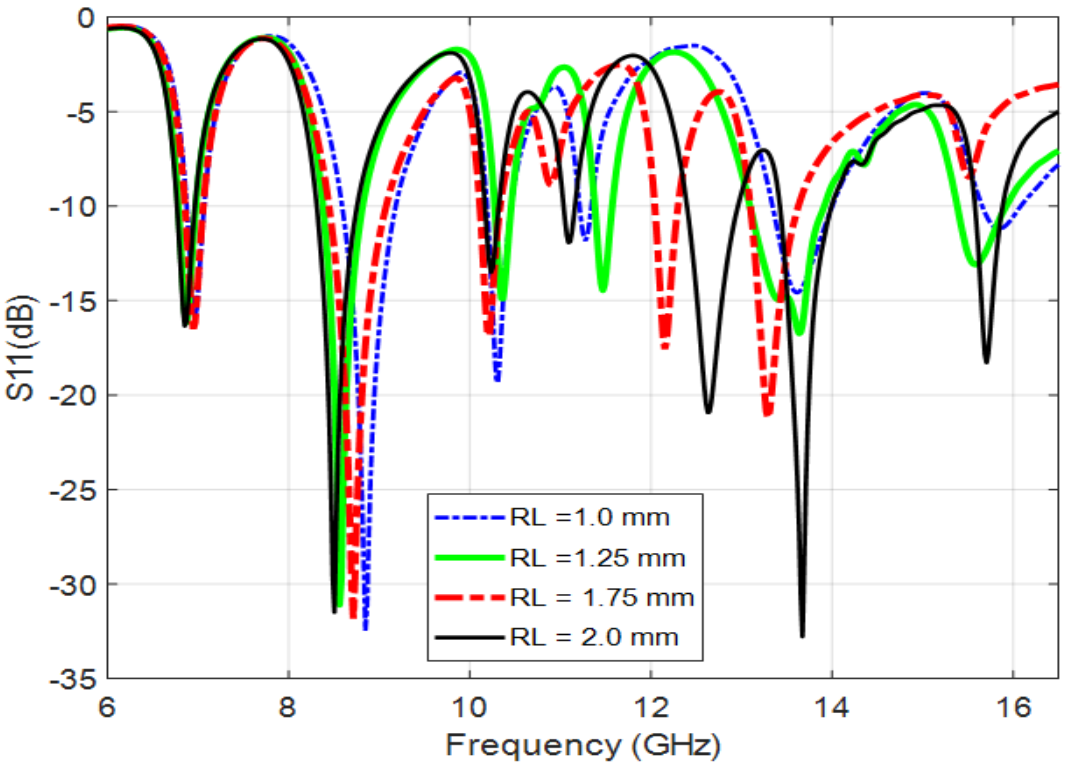

(c)

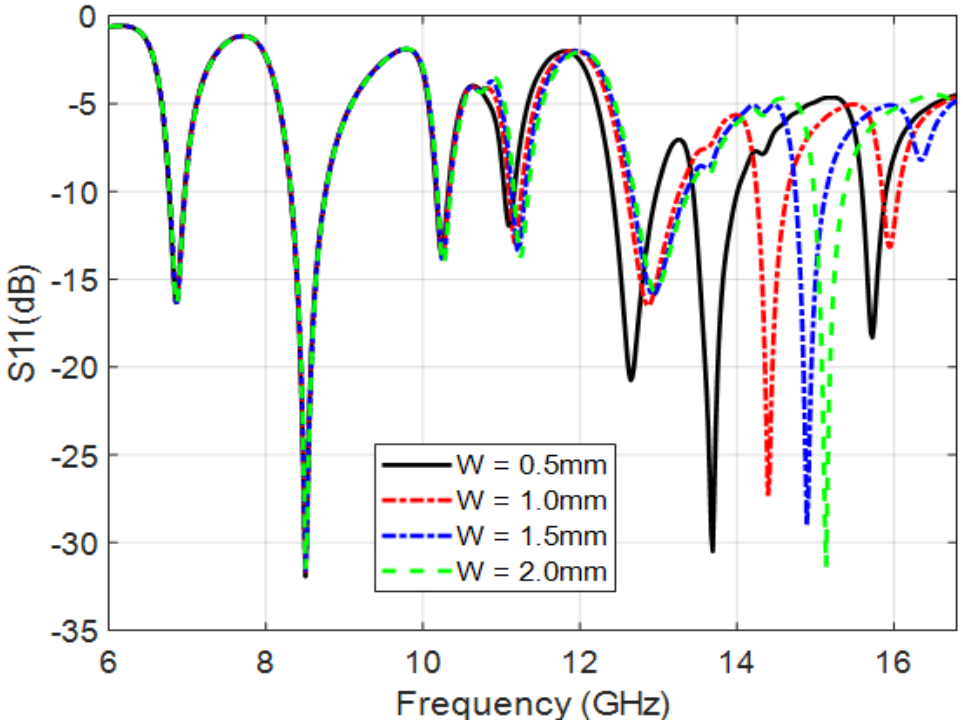

(d)

Figure 3.6: ISMeTM Unit Cell Parameters (a) Variation of S11 with g, (b) Variation of S21 with g, (c) Variation of S11 with RL, (d) Variation of S11 with W.

However, the MeTM has its best performance at the dimension of g = 0.5 mm. Furthermore, the variation of S21(dB) parameter with the variation of the ring gap (g) is displayed in Figure 3.6(b). At g = 1 mm, 1.5 mm, and 2 mm, the ISMeTM has four and three resonance frequencies, respectively. Thus, when g is at 0.5 mm seven resonances are realized, making it the best dimension for optimal performance of the design.

The variation of the strip length (RL) of the unit cell is presented in Figure 3.6(c). It is observed that the most suitable dimension of RL for the ISMeTM unit cell is 2 mm. Similarly, the strip width (W) of the unit cell is varied and presented in Figure 3.6(d).

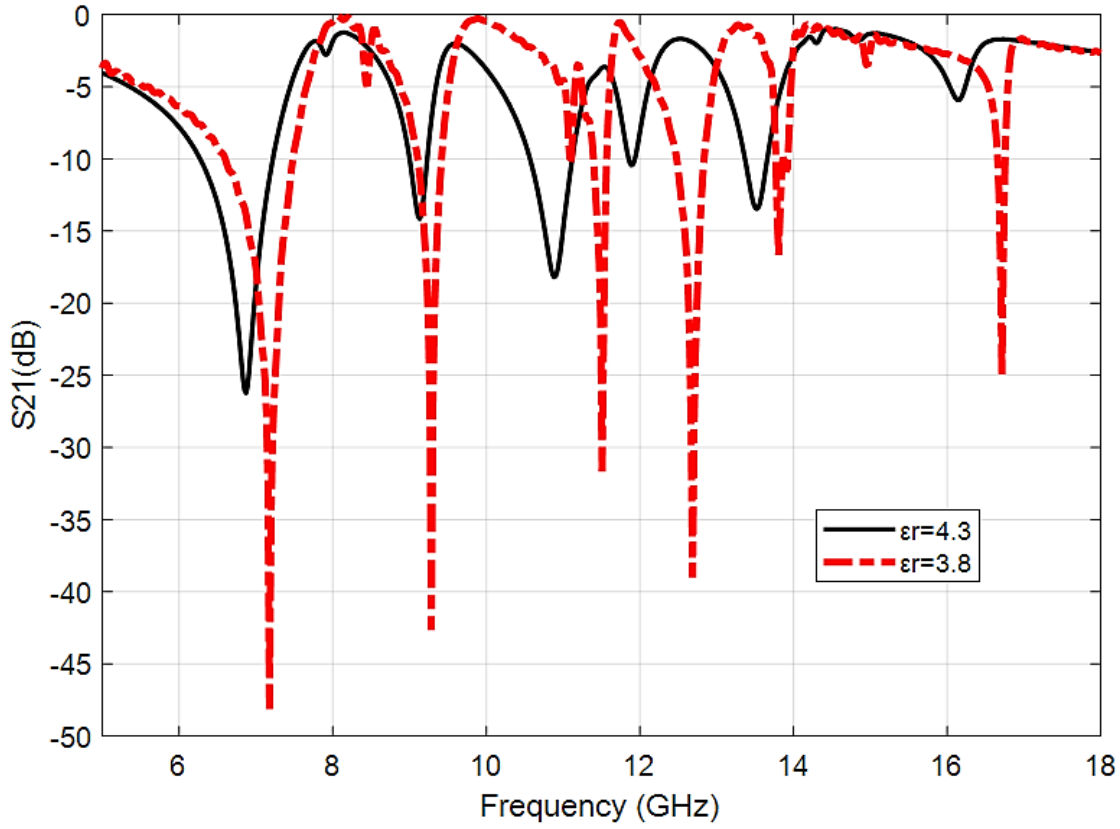

(a)

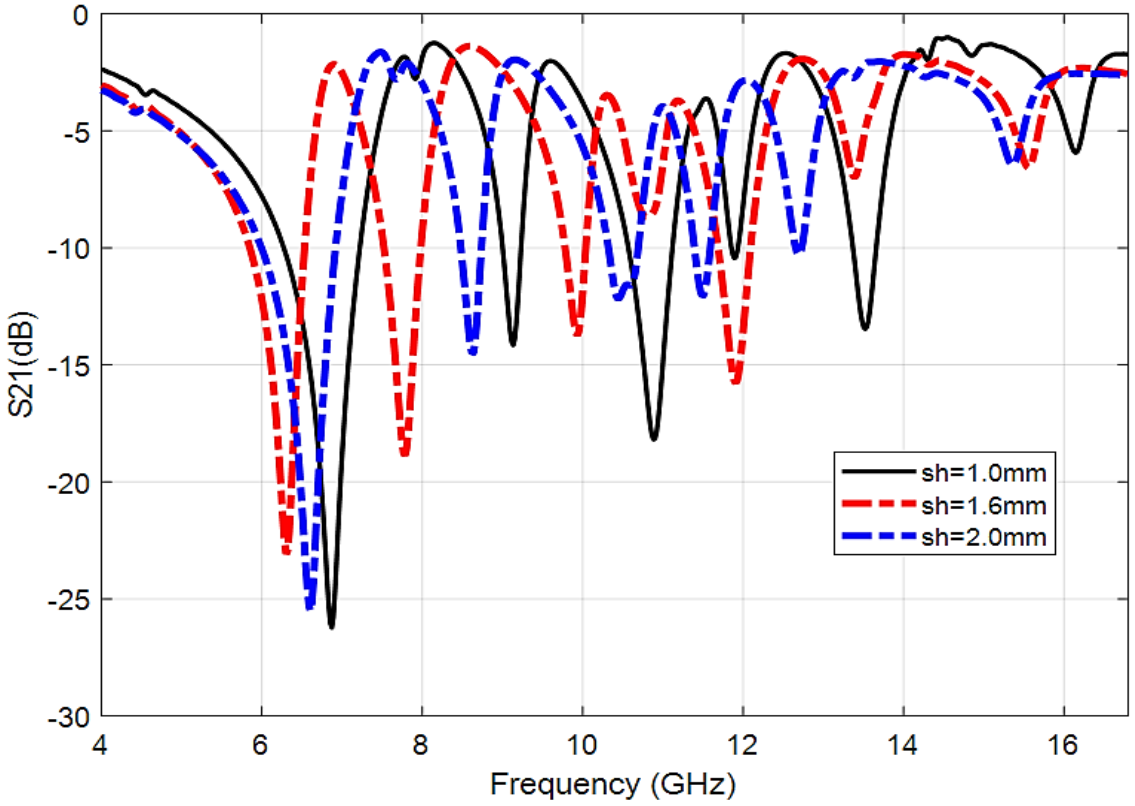
S21(dB)
Frequency (GHz)
sh=1.0mm
sh=1.6mm
sh=2.0mm

(b)

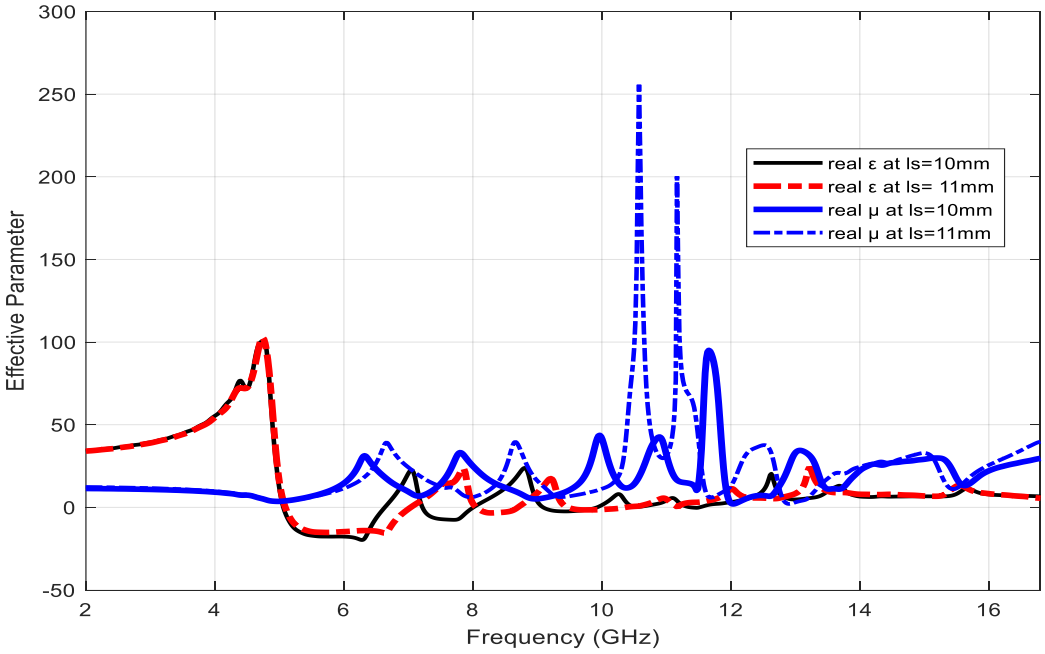
Effective Parameter
Frequency (GHz)
real ε at ls=10mm
real ε at ls= 11mm
real μ at ls=10mm
real μ at ls=11mm

(c)

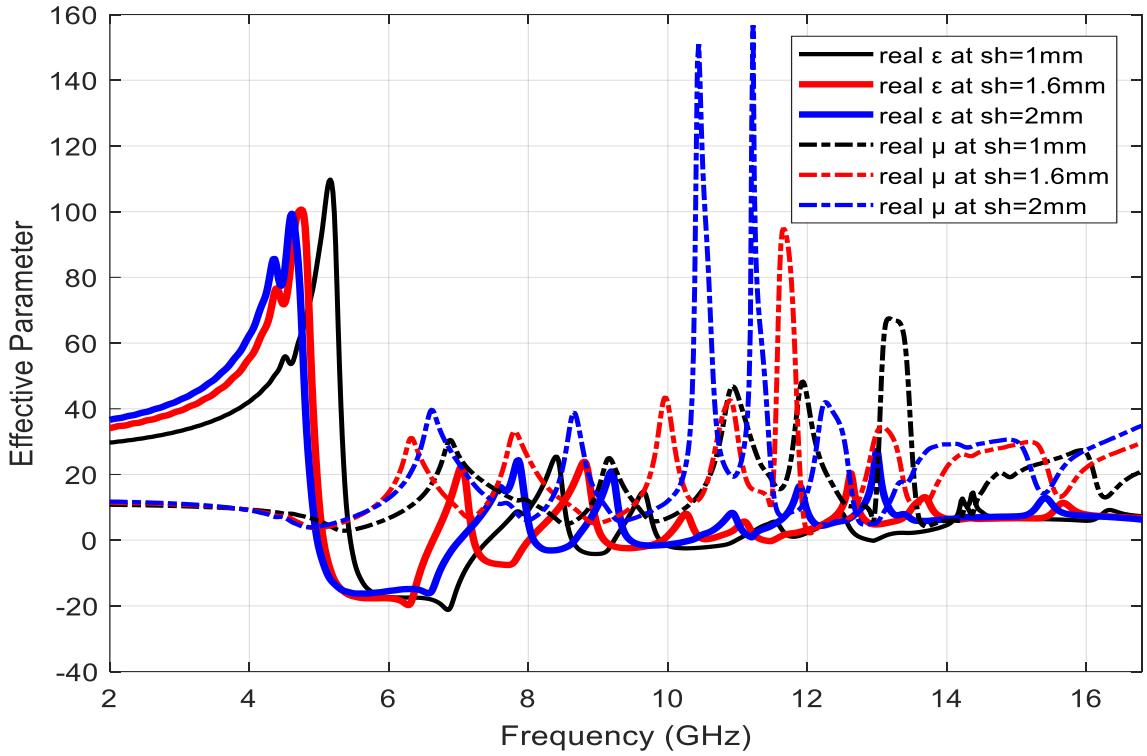

(d)

Figure 3.7: ISMeTM Unit Cell Parameter Variation (a) S21 with Dielectric Constant of the Substrate, (b) S21 with sh, (c) Permittivity and Permeability with ls, (d) Permittivity and Permeability with sh.

It can be studied that at W = 0.5 mm the unit cell exhibits the optimum multi-band behavior. The variation of the S21 parameter with the dielectric constant and sh are shown in Figures 3.7(a) and 3.7(b), respectively. From these figures, it can be observed that the center frequencies and the frequency bands can be modified by varying the dimensional parameters of the structure. The variation of permittivity and permeability with ls is shown in Figure 3.7(c). The variation of permittivity and permeability with sh is shown in Figure 3.7(c). From Figures 3.7(c) and 3.7(d), it can be observed that the frequency band with SNG property and the values of permittivity and permeability can be varied by changing the dimensional parameters of the structure.

3.8 ISMeTM Array Analysis

The performance analysis of the ISMeTM unit cell's 1 × 2 array, 2 × 2array, and 2 × 4 array configurations are presented in this section. The overall dimensions are 10 × 20 mm^2, 20 × 20 mm^2, and 20 × 40 mm^2. To validate the results of the ISMeTM unit cell configuration, the three array configurations are investigated. The Nicolson–Ross–Weir (NRW) is used evaluate the array's effective parameters. The schematic diagram of 1 × 2 array, 2 × 2array, and 2 × 4 array configuration is presented in Figure 3.8. The arrays are formed by combining two-unit cells horizontally. The S11 and S21 parameters of the array configurations are simulated for the frequency range of 2–18 GHz, and the same approach is used to retrieve their effective parameters.

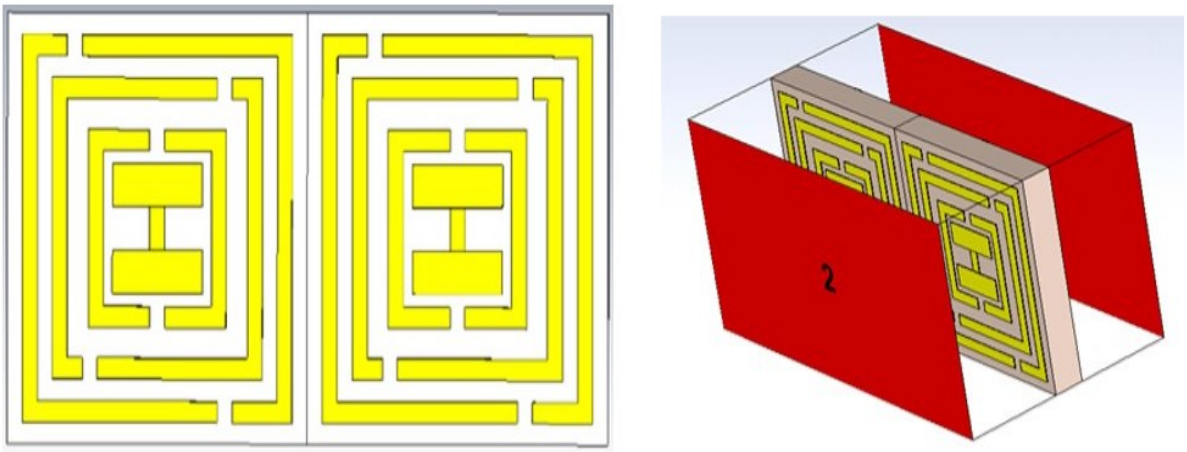

(a)

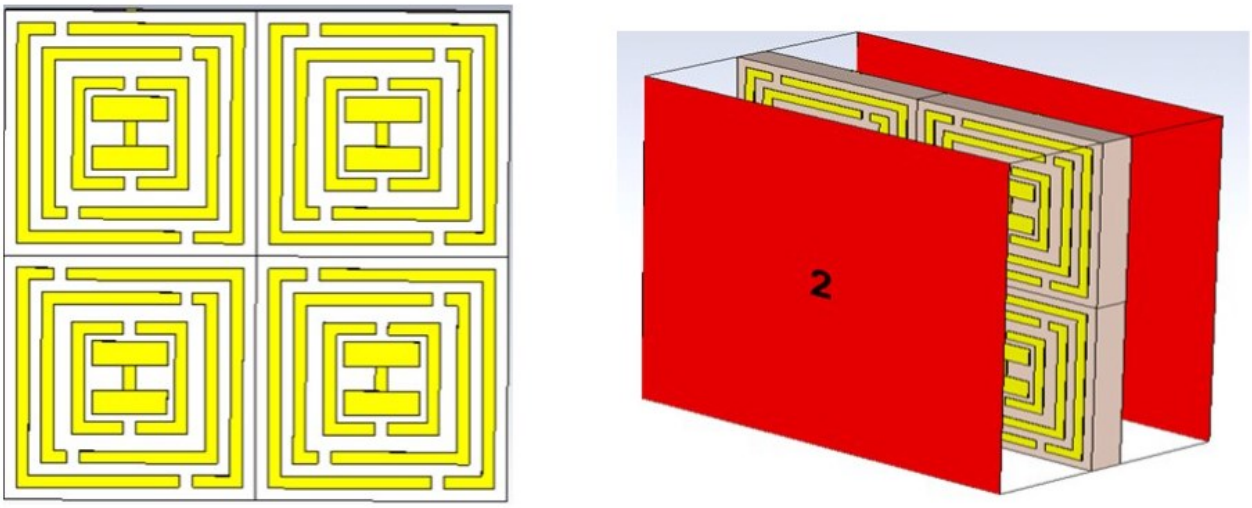

(b)

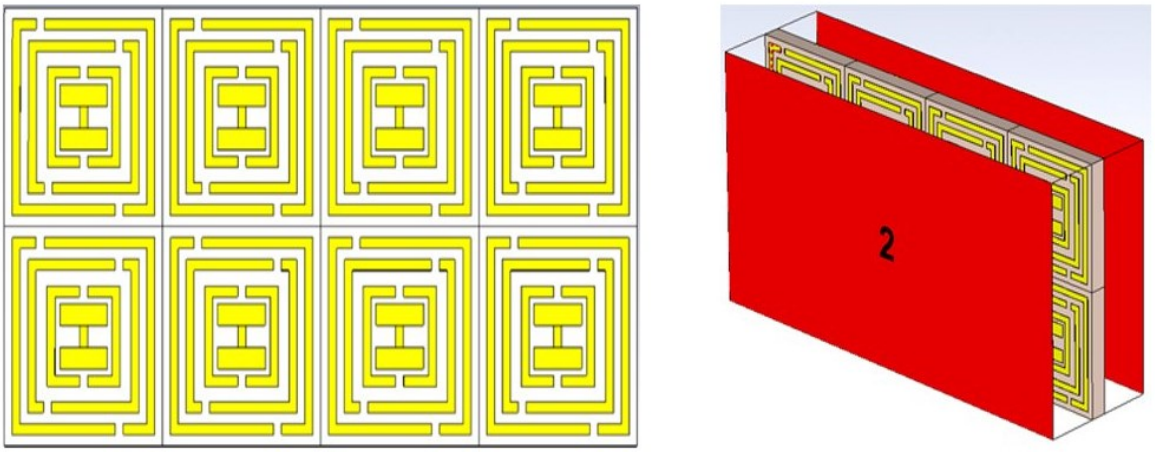

(c)

Figure 3.8: Schematic Diagram of ISMeTM arrays: (a) Geometry and Simulated Model of 1 × 2 Array (b) Geometry and Simulated model of 2 × 2 Array (c) Geometry and Simulated Model of 2 × 4 Array.

In Figure 3.9, the S-parameters S_{11} (dB) and S_{21} (dB) are presented for the three array configurations. The 1 × 2 array shows the transmission dips at 6.23, 7.76, 10.10, 10.78, 11.72, 13.36 and 15.5 GHz, which are much closed to the ISMeTM unit cell. The 2 × 2 array structure generate transmission minima at frequencies 4.63, 6.05, 6.64, 7.44, 8.12 and 10.4 GHz. The dips of transmission coefficient $|S_{21}|$ of 2

× 4 array are observed at frequencies 4.69, 5.96, 6.52, 7.30, 7.84, 8.20 and 10.52 GHz. The permittivity of the array configurations is shown in Figure 3.10b. The SNG frequency ranges for 1 × 2 array; 2 × 2 array and 4 × 4 array are 5.46–6.29, 11.35–11.44, 13.2–14.9, 15.8–16.4; 5.44–6.31, 13.3–13.9, 14.6–15.8, 16.1–16.3 GHz and 5.46–6.28 GHz, 13.6–14.2 GHz, 14.9–15.3 GHz, 15.9–16.4 GHz, respectively.

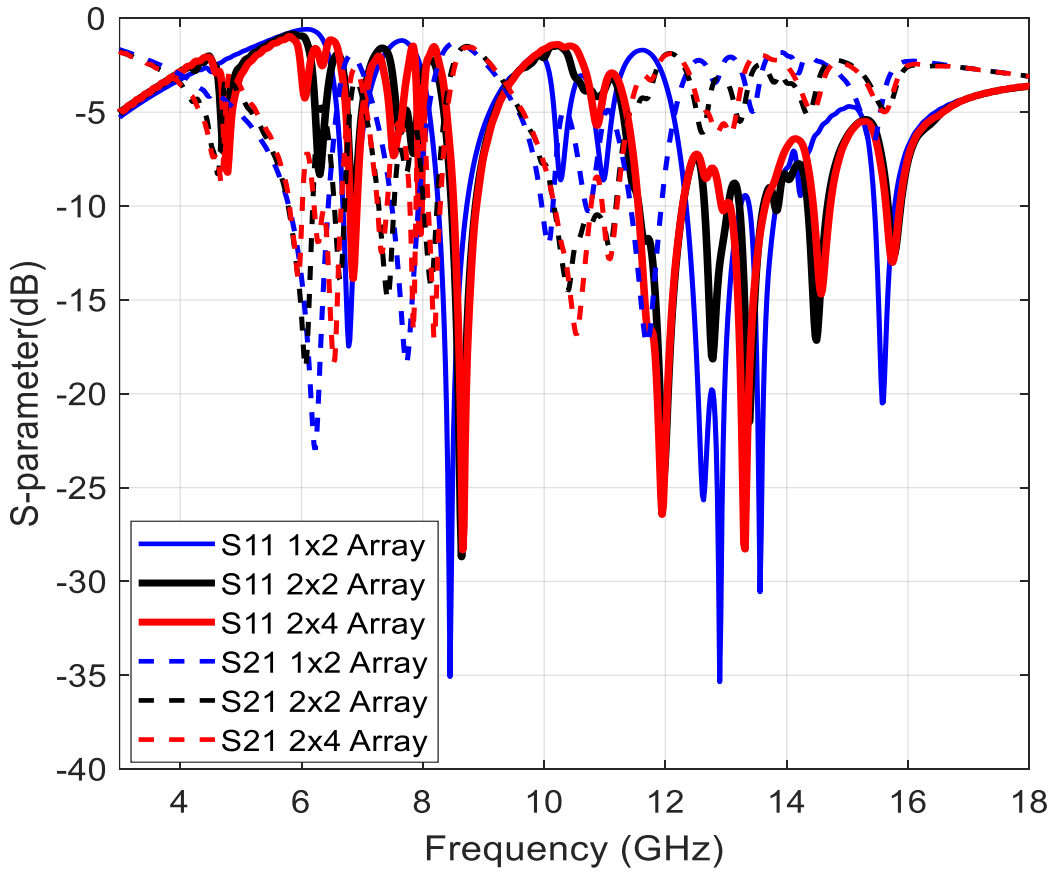

Figure 3.9: S-Parameters of Array Configuration.

The parameters of various array configurations are summarized in Table 3.3. The frequency ranges for the parameters in the three array structures are nearly identical to the single unit cell, except variation for a few frequency bands. Due to mutual coupling effect between the array elements, there may be little variation in the array characteristics as compared to the unit cell [61].

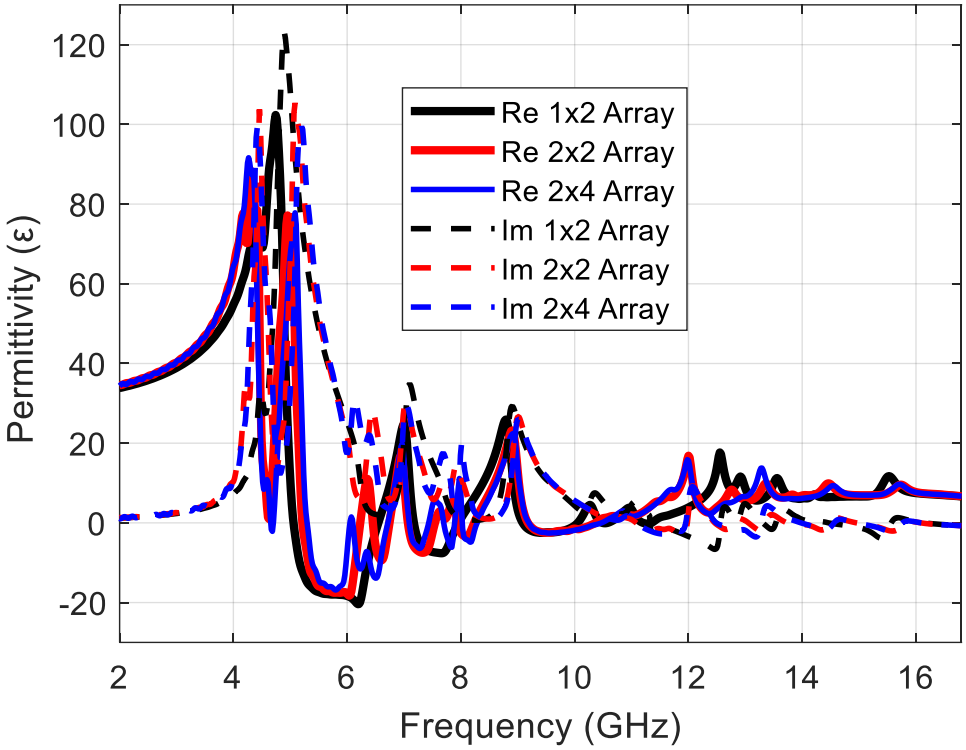
Re 1x2 Array
Re 2x2 Array
Re 2x4 Array
Im 1x2 Array
Im 2x2 Array
Im 2x4 Array
Permittivity (ε)
Frequency (GHz)
120
100
80
60
40
20
0
-20
2
4
6
8
10
12
14
16

(a)

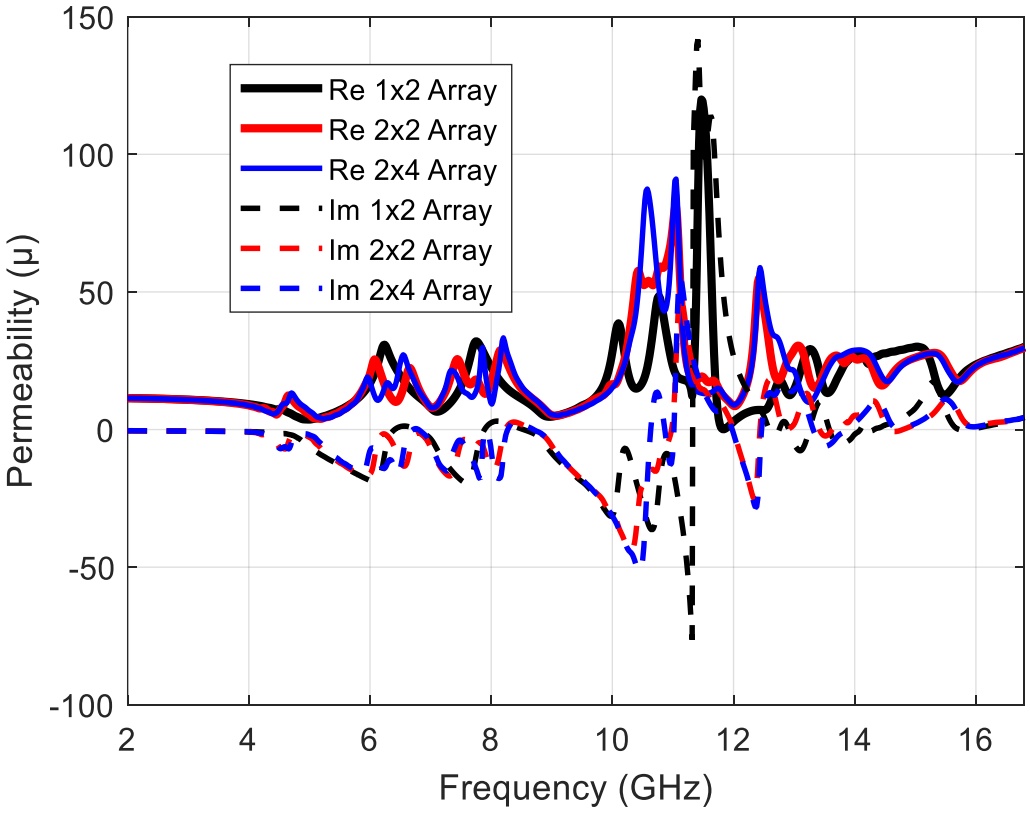
Re 1x2 Array
Re 2x2 Array
Re 2x4 Array
Im 1x2 Array
Im 2x2 Array
Im 2x4 Array
Permeability (μ)
Frequency (GHz)
150
100
50
0
-50
-100
2
4
6
8
10
12
14
16

(b)

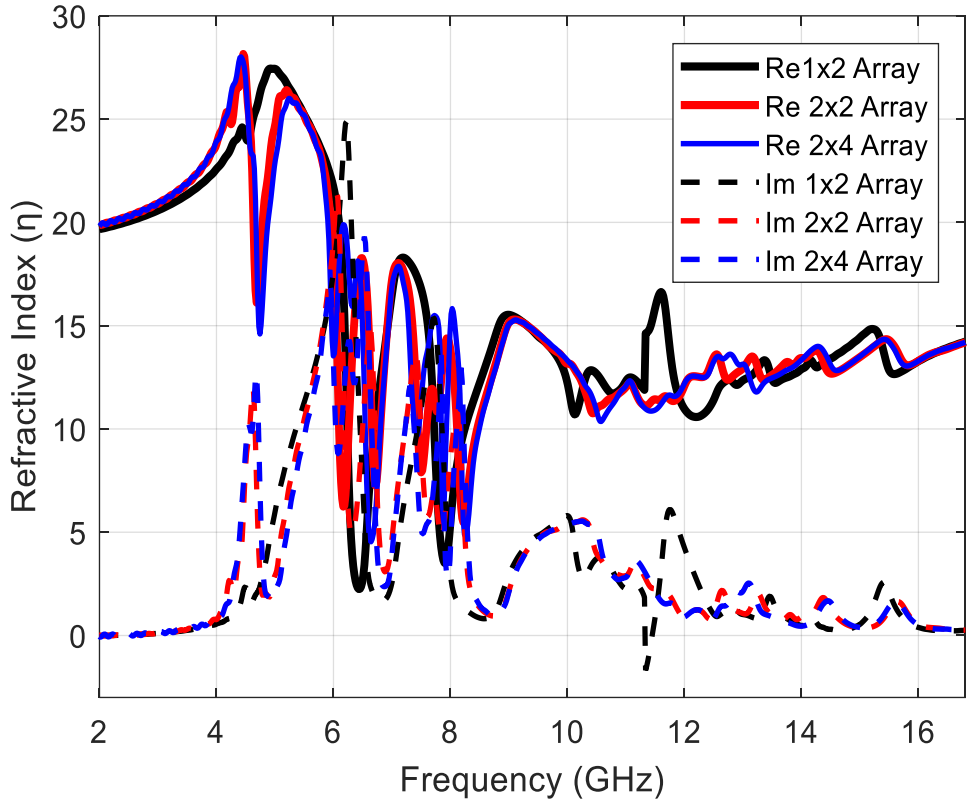

(c)

Figure 3.10:Parameters of Array Configurations (a) Permittivity, (b) Permeability, (c) Refractive Index.

In the proposed array, it can be observed that the array arrangements show similarities with the unit cell except for a few frequency bands that changes slightly which is due to the mutual coupling effect between the array elements. This occurs when two or more-unit cells are vertically oriented on the *y*-axis. However, the arrays still exhibit multi-band properties. The comparative analysis of the proposed ISMeTM is presented in Table 3.4. From this table, it can be observed that the proposed ISMeTM is low cost, compact in size and produces seven resonances. The proposed ISMeTM is suitable for multi-band C/X/Ku-band applications.

Table 3.3 Parameter of ISMeTM Unit Cell, ISMeTM 1 x 2 Array, ISMeTM 2 x 2 Array, and ISMeTM 2 x 4 Array

Configuration	**SNG Frequency range (GHZ)**	**S21 Dips frequencies (GHz)**	**S21 (dB)**
ISMeTM unit cell	5.46-6.29, 11.6-11.8, 13.8-15, 15.8-16.8	6.31, 7.79, 9.98, 10.82, 11.86, 13.36, 15.5	-22.96, -18.89, -13.47, -8.84, -15.49, -6.87, -6.45
ISMeTM 1 x 2 array	5.46–6.29, 11.35–11.44, 13.2–14.9, 15.8–16.4	6.23, 7.76, 10.10, 10.78, 11.72, 13.36, 15.5	−22.40, −17.91, −11.64, −9.84, −17.16, −4.56, −6.35
ISMeTM 2 x 2 array	5.44–6.31, 13.3–13.9, 14.6 15.8, 16.1–16.3	4.63, 6.05, 6.64, 7.44, 8.12, 10.4	−8.33, −18.46, −13.97, −14.67, −14.04, −14.21
ISMeTM 2 x 4 array	5.46–6.28, 13.6–14.2, 14.9–15.3, 15.9–16.4	4.69, 5.96, 6.52, 7.30 7.84, 8.20, 10.52	−8.67, −13.57, −17.35, −12.33, −16.41, −16.49, −16.76

Table 3.4 Comparative analysis of the proposed ISMeTM with the structures in literature

Ref	Dimension $(mm)^2$	Shape	Substrate	Band	Resonant Frequency (GHz)
[80]	4 x 4	Double S	FR-4	Ku-	1
[81]	30 x 22 x 0.8	CSSR	Roger Duroid TM 5880	C	1
[82]	25 x 25 x 1	U-shaped	Glass	C	1
[83]	12 x 11 x 1.6	Aztec	FR-4	C, X, Ku	4
[84]	5 x 5 x 0.25	V- shaped	Fused Quartz	X	1
[85]	12.5 x 12. 5	I- shaped	FR-4	X	1
[86]	10 x 10	Inverse double L	Roger RT 5880	C. X, Ku	4

[88]	12 x 12 x 1.635	C- shaped	Roger RT 6010	S, C, X, Ku	4
[89]	30 x 30	H-shaped	FR-4	S, C, X, Ku	4
[90]	9 x 9 x 1.6	Double C	FR-4	S, C, X, Ku	5
Proposed	10 x 10 x 1.6	I-shaped	FR-4	C, X, Ku	7

3.9 Chapter Summary

A novel ISMeTM unit cell using the SSRR along with its arrays has been designed, simulated, and analyzed in this paper. The structure is designed using copper as its metal strip on a FR-4 dielectric substrate. The SSRRs along with an I-shaped patch is utilized for designing the ISMeTM. The detailed theory and equivalent circuit of the ISMeTM are presented. The proposed structure produced multiple resonances and SNG behavior. The proposed ISMeTM is suitable for use in multi-band microwave applications including C band, X band and Ku band. The design and analysis of 1 × 2, 2 × 2, and 2 × 4 array structures of the proposed ISMeTM unit cell are investigated. The proposed low-cost and compact ISMeTM are suitable for multi-band satellite communication systems, radar applications, sub-6 GHz 5G applications, ultra-wideband applications, etc.

Chapter 4

Microstrip Patch Antennas Using Metamaterial Superstrate with Enhanced Gain

4.1 Introduction

This chapter outlines the design of MPAs using MeTM superstrate to enhance the antenna gain. Two different metamaterial superstrates have been proposed, designed, simulated, and discussed to improve the performance of the antenna. The first MeTM proposed is the novel square split ring resonant (SSRR) which would be referred to as "Design 1" throughout this chapter. The novelty of this work lies in the design MeTM unit cell which has four split gaps in its outer ring and a single cut in the inner ring structure. This feature of the SSRR makes it distinct from other SRR designs in existing works. The second MeTM utilized in this chapter is the ISMeTM which has been analysed in Chapter 3. A 7 x 7-unit cell array of the ISMeTM have been on the FR-4 substrate to create a superstrate layer. This ISMeTM superstrate layer would be referred to as "Design 2" throughout this chapter. The two MeTMs, Design 1 and Design 2 will be evaluated, and the best performing antenna will be fabricated and measured.

4.2 Design and Geometry of the SSRR Inspired Patch Antenna (Design 1)

The proposed MeTM unit cell and antenna parameters are discussed in this section. The MeTM unit cell is designed by using SRR and a thin wire strip notched on the back of the substrate for excitation of the metamaterial structure. The outer ring length (L) = 11mm, width of the outer ring (S) = 1.5mm, inner ring length (n) = 6mm, width of inner ring (p) = 1mm, the gap between the split rings (d, g) = 1mm. To achieve optimal antenna performance, specific factors are being put into consideration. These factors include the size of the antenna, bandwidth, and resonance frequency. The parameters and geometry of the proposed antenna is being illustrated in Table 4.1 and Figure 4.1. This antenna consists of two

metallic layers, the ground plane, and the patch. In this section, the microstrip patch antenna has been designed to operate at a frequency of 5.85 GHz with an input impedance of 50 Ω using a dielectric material FR4 substrate with dielectric constant (ε_r) of 4.3, substrate height (h_s) of 1.6mm, and tangent loss of 0.002. The transmission line model equations (2.15) –(2.24) have been utilized for the antenna design.

Table 4.1 Antenna Dimensional Parameters

Parameter	Dimension (mm)	Parameter	Dimension (mm)
Wg	25	n	6
Lg	21.403	g,p,d	1
Wp	15.89	S	1.5
Lp	11.803	hc	0.035
gpf	0.008	ag	9
fi	4.43	Wf	3.039
W	13	hs	1.6
L	11	m	8

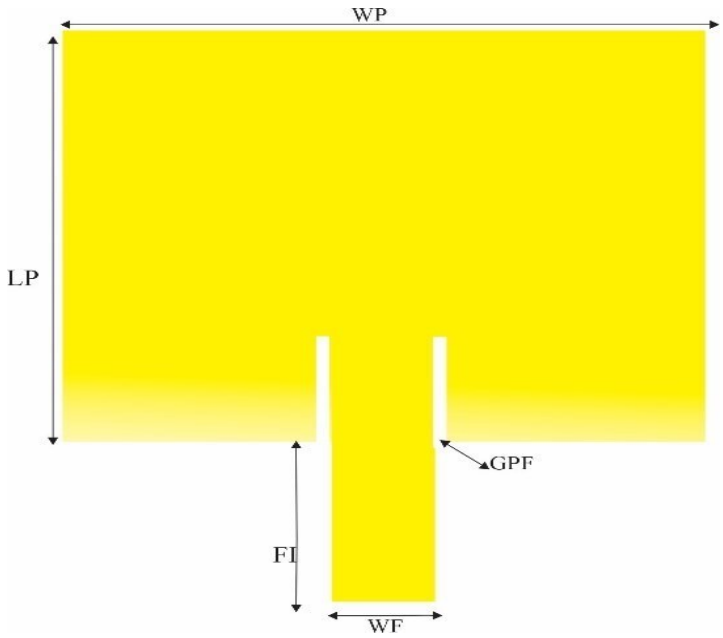

(a)

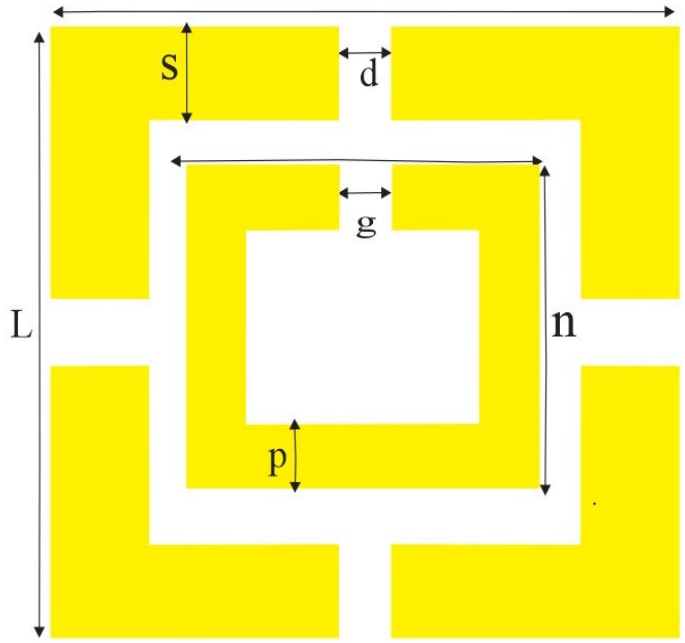

(b)

(c)

Figure 4.1: Geometry of the Proposed Antenna (a) Radiating Patch (b) SRR Unit Cell (c) Side View.

4.3 Result of the SSRR Inspired Patch Antenna (Design 1)

The proposed antenna is simulated using the CST Studio Suite. The antenna geometry shown in Figure 4.1(a) produces a resonance frequency at 5.85 GHz with it S11 greater than 10 dB with bandwidth ranging from 5.69 - 6.04 GHz and a return loss of -16.89 dB. Hence, with the SSRR loaded directly above the radiating patch with 9mm to the ground plane. The antenna resonance at 5.902 GHz with bandwidth ranging from 5.73-6.16 GHz and a return loss of -30.87 dB as shown in Figure 4.2. It is observed that the antenna is a single band antenna. We can also see a gain improvement by placing the SSRR superstrate directly above the patch of the antenna. When the SSRR was made as to the same dimension as the substrate on the ground plane, a significant loss was experienced on the gain field pattern. The size of the superstrate is the same as the size of the radiating patch.

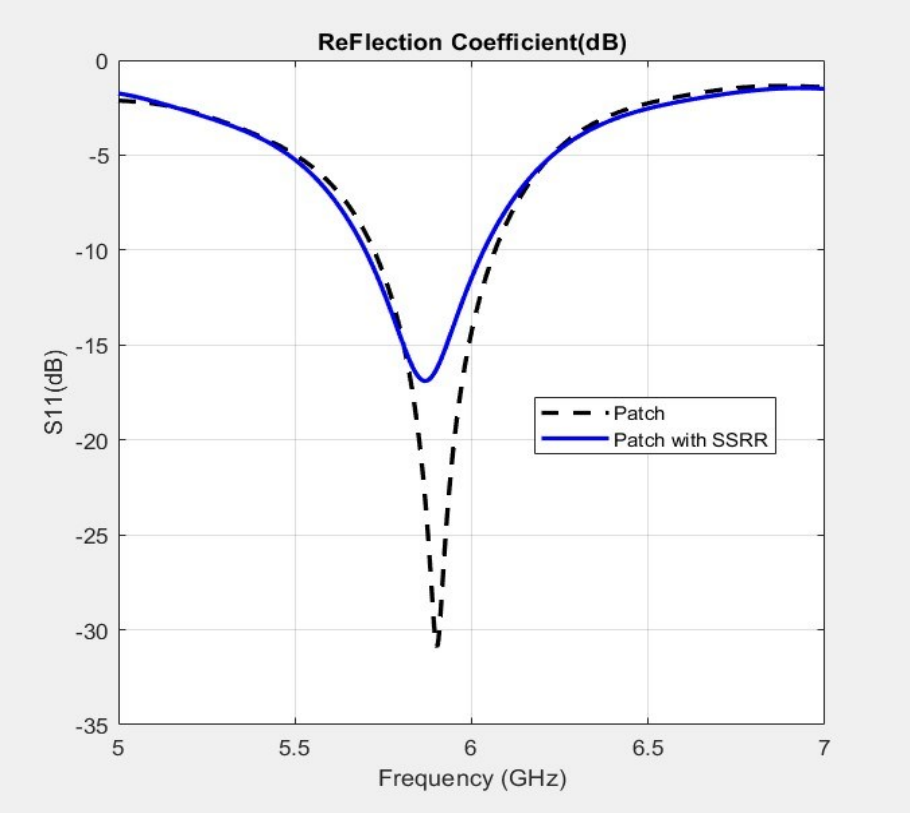

Figure 4.2: Reflection Coefficient Curve of Antenna Loaded with the Square Split Ring Resonator (SSRR).

The comparison of different air gaps between the radiating patch and the SSRR is shown in Figure 4.3. At different distance, the return loss of the antenna varies. It is observed that at ag = 5 mm, ag = 7 mm, and ag =11mm a return loss of -17.47 dB, 21.24 dB, and 17.52 dB, respectively are achieved. The SSRR loaded antenna has its optimal performance at 9 mm with a return loss of -30.87 dB and with a gain of 5.28 dBi.

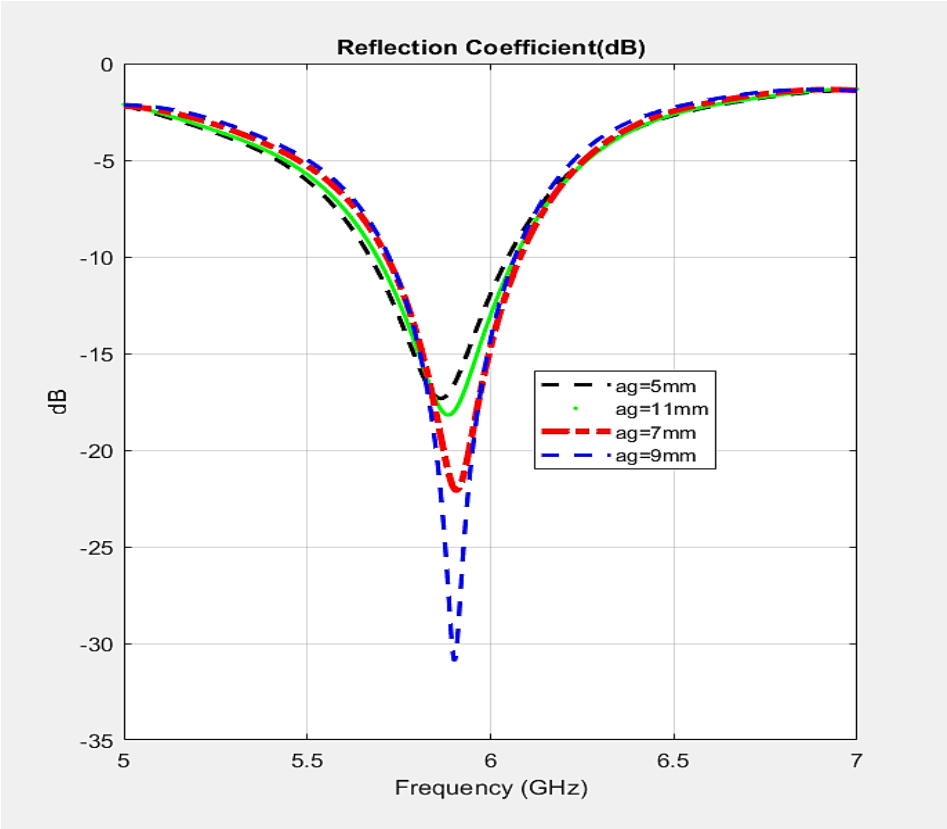

Figure 4.3: Reflection Coefficient for Variation of Air Gap (ag).

Figure 4.4 depicts the 3-D radiation pattern of the proposed antenna. At the radiating frequency of 5.85 GHz, it can be observed that a gain of 5.278 dBi was achieved.

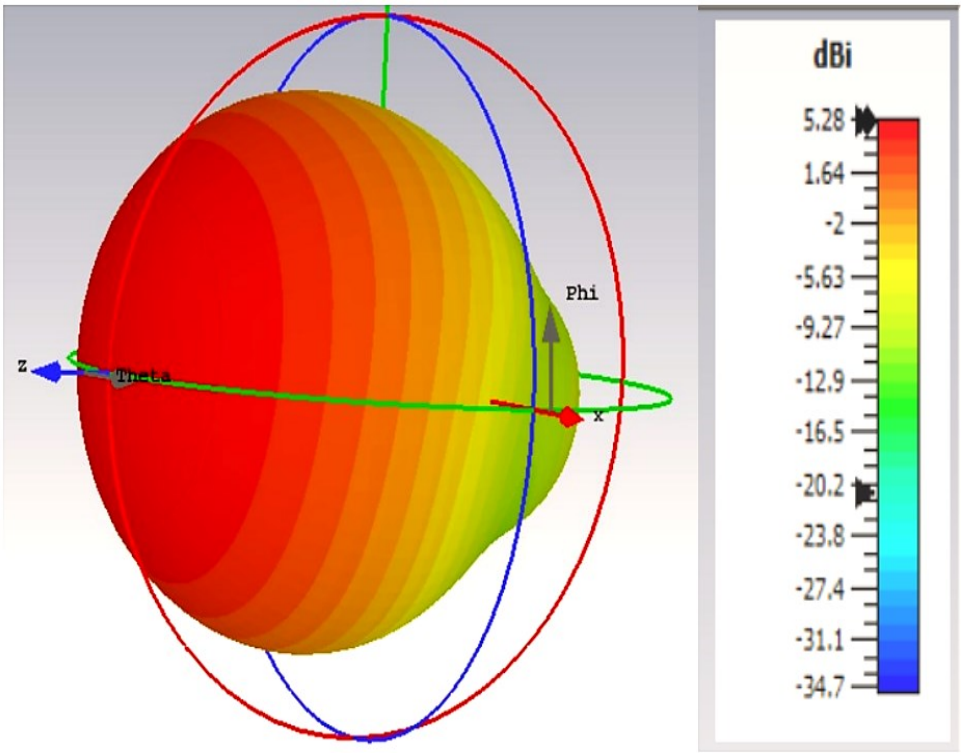

Figure 4.4: 3D- Radiation Pattern (a) Patch only (b) SSRR inspired Antenna.

The normalized patterns of the SSRR loaded antenna are shown in Figure 4.5. The 2-D simulated radiation patterns at 5.0, 5.4, and 5.8 GHz are shown in Figure 4.5(a), Figure 4.5(b) and Figure 4.5(c), respectively.

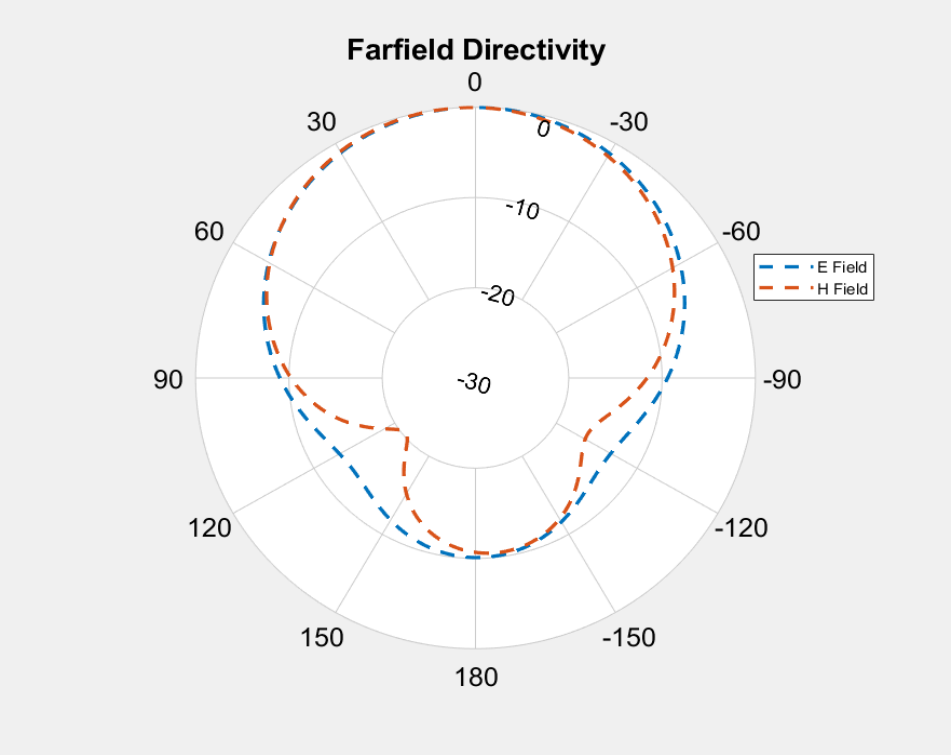
Farfield Directivity
0
30
-30
60
-60
90
-90
120
-120
150
-150
180
0
-10
-20
-30
E Field
H Field

(a)

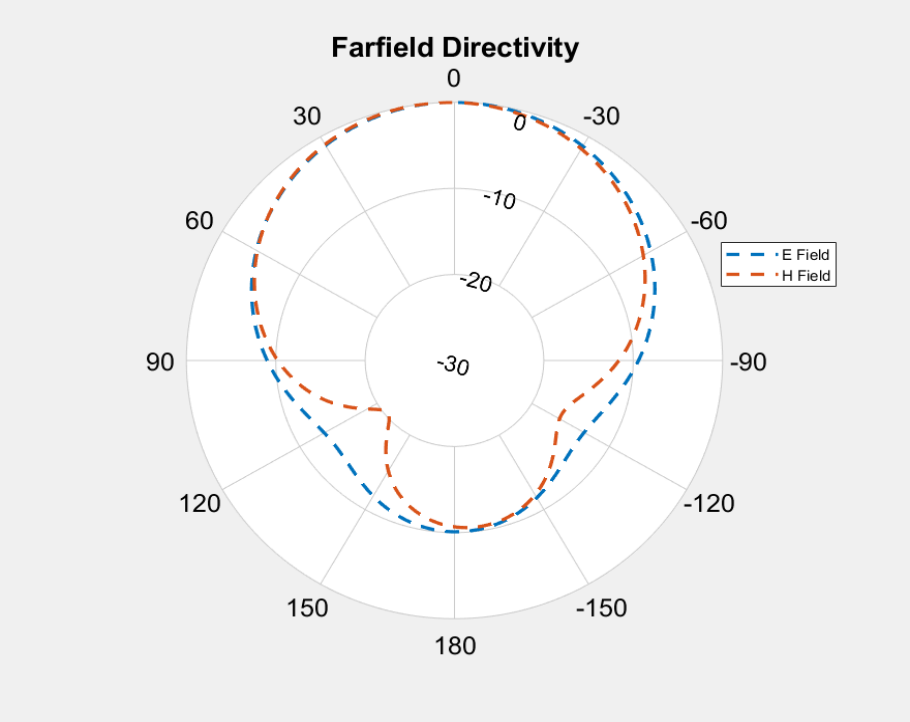
Farfield Directivity
0
30
-30
60
-60
90
-90
120
-120
150
-150
180
0
-10
-20
-30
E Field
H Field

(b)

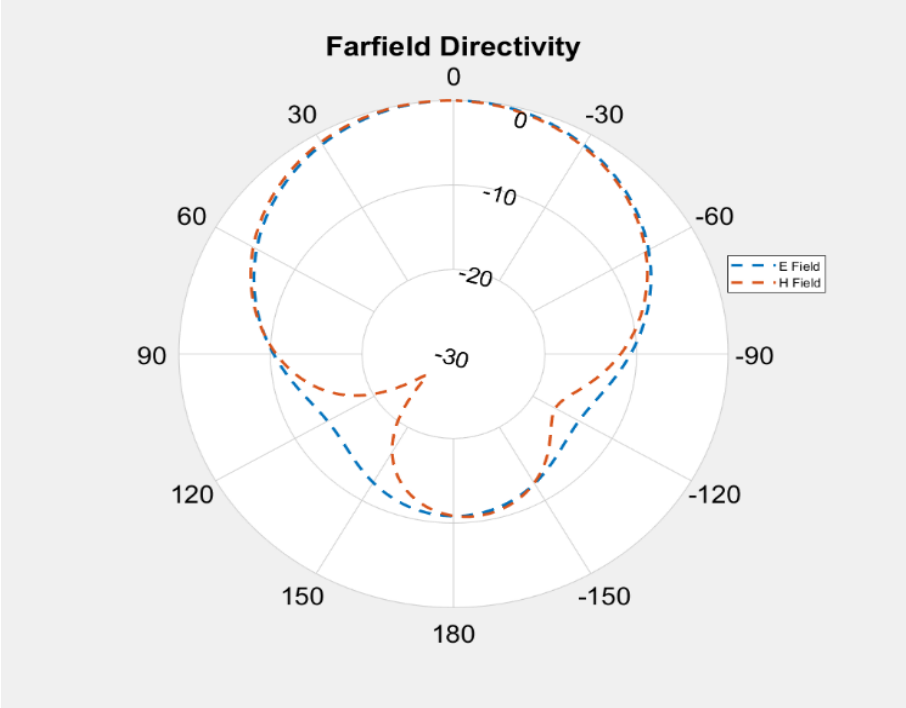

(c)

Figure 4.5: Normalized radiation patterns of the antenna at (a) 5.0 GHz, (b) 5.4 GHz (c) 5.8 GHz.

It can be observed there is an increase in the radiation pattern at 5.8 GHz as compared to that of 5.0 GHz and 5.4 GHz. The gain of the conventional MPA was improved from 4.04 dBi to 5.278 dBi by loading the SSRR superstrate to the patch of the antenna as shown in Table 4.2. The effect of variation of the distance between the radiating patch and the SSRR MeTM on the gain is shown in Table 4.3.

Table 4.2. Comparison with Conventional Patch and Proposed Antenna

Antenna Type	F_r (GHz)	Bandwidth (MHZ)	Directivity (dBi)	Gain (dB)
Conventional patch	5.8	350	5.812	4.04
Proposed Antenna	5.85	430	6.709	5.278

An increase in the antenna bandwidth and directivity is observed. The comparison of the main lobe at phi=0^0, phi=90^0 and beamwidth at various frequencies is shown in Table 4.4. The angular beamwidth (3dB) at phi=0^0 and phi=90^0 tends to decrease as the operating frequency increases. This implies that as the antenna gain increases, the antenna beamwidth becomes smaller.

Table 4.3. Distance Between the Radiating Patch and SSRR Metamaterial

Frequency (GHZ)	**Gain ag=5 (mm)**	**Gain ag=7 (mm)**	**Gain ag=9 (mm)**	**Gain ag=11 (mm)**
5.6	4.56	5.13	5.20	4.91
5.8	4.57	5.22	5.28	5.19
6.0	4.40	5.07	5.13	5.02

Table 4.4. The Main Lobe and Beamwidth at Various Frequencies

Frequency (GHz)	**Main Lobe Phi=0^0**	**Main lobe Phi=90^0**	**Angular beamwidth (3dB) phi=0^0**	**Angular beamwidth (3dB) phi=90^0**
5.0	0.0	2.0	95.3	93.3
5.2	0.0	2.0	93.6	92.2
5.4	0.0	3.0	91.5	91.3
5.6	0.0	3.0	89.0	90.5
5.8	0.0	3.0	86.6	89.7
6.0	0.0	2.0	83.9	89.0

The maximum gain, directivity, and efficiency of the antenna at various frequencies are presented in Table 4.5. It can be observed that the radiating and total efficiency of the antenna tends to decrease as the frequency of the antenna is increased.

Table 4.5 Maximum Gain, Maximum Directivity, and Efficiency of the Antenna

Frequency (GHz)	**Max. Gain (dB)**	**Max. Directivity (dBi)**	**Total Efficiency (dB)**	**Radiating Efficiency (dB)**
5.0	4.455	6.262	-5.834	-1.802
5.2	4.668	6.373	-4.442	-1.673
5.4	4.940	6.478	-3.262	-1.516
5.6	5.073	6.589	-2.120	-1.369
5.8	5.278	6.709	-1.730	-1.419
6.0	5.028	6.838	-1.903	-1.616

The comparison of the existing antennas with the square SRR metamaterial inspired antenna is presented in Table 4.6. The comparison is done in terms of the permittivity of the substrate, the technique used, bandwidth, and the antenna gain. It can be observed that the proposed antenna has the highest gain compared to others. We can see that as the gain of the antenna increased the antenna becomes more directive and this is most suitable for wireless mobile communication.

Table 4.6 Comparison with Similar Antennas

Ref.	**F_r (GHz)**	**MeTMs**	**Dielectric Constant**	**Bandwidth (MHZ)**	**Gain (dBi)**
[135]	2.4	SRR	4.4	800	2.586
[137]	2.48 / 3.49	SRR	4.3	350 / 390	2.4 / 3.5
[154]	2.4	CSRR	4.2	1 GHz	4.90

[155]	3.31 / 3.88 /4.61	SRR & CSRR	4.4	190 / 125 / 90	-
Proposed Antenna	5.85	SSRR	4.4	430	5.278

4.4 Design of MPA using I-Shaped Metamaterial (Design 2)

In this section , we utilize the ISMeTM superstrate for the performance enhancement of the MPA. The work done in Section 4. 2 and 4. 3 was extended by introducing a 7 x 7-unit cell array of the ISMeTM is etched over an MSP as a superstrate at a distance of 7mm. An in-phase electric field area is created on the top layer of the superstrate to improve the performance of the antenna. Three operating frequencies were obtained with the structure as compared to the single band obtained in Section 4.3. This structure is fabricated, and measurement was carried out to verify the performance.

4.4.1 Geometry of the ISMeTM Superstrate

The geometry and fabricated structure of the 7 x 7 I-shaped MeTM array is illustrated in Figure 4.6. The MeTM array is printed on the FR-4 substrate with a dielectric constant of 4.3 and a loss tangent ($tan\delta$) of 0.025. The thickness of the substrate (S_h) and the thickness of the annealed copper *(hc)* used for the split ring resonator are 1.6 mm and 0.035 mm, respectively. The primary function of splits in the ring resonators is to ensure that the inductance and capacitance interact with one another to determine the operating frequency. The unit cell's total optimum size is 10 x 10 x 1.6 mm^3 ($0.2\lambda_0 \times 0.2\lambda_0 \times 0.03\lambda_0)\lambda_0$. The dimensional parameters of the 7 x 7 ISMeTM array cell are presented in Table 4.7.

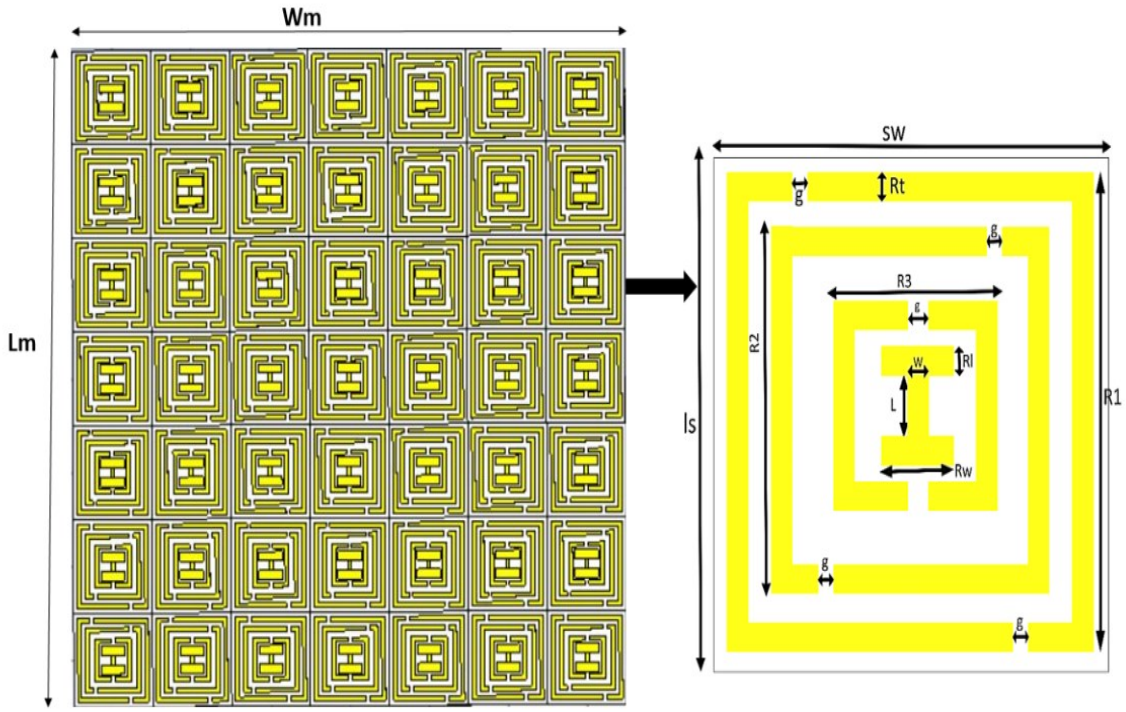

(a)

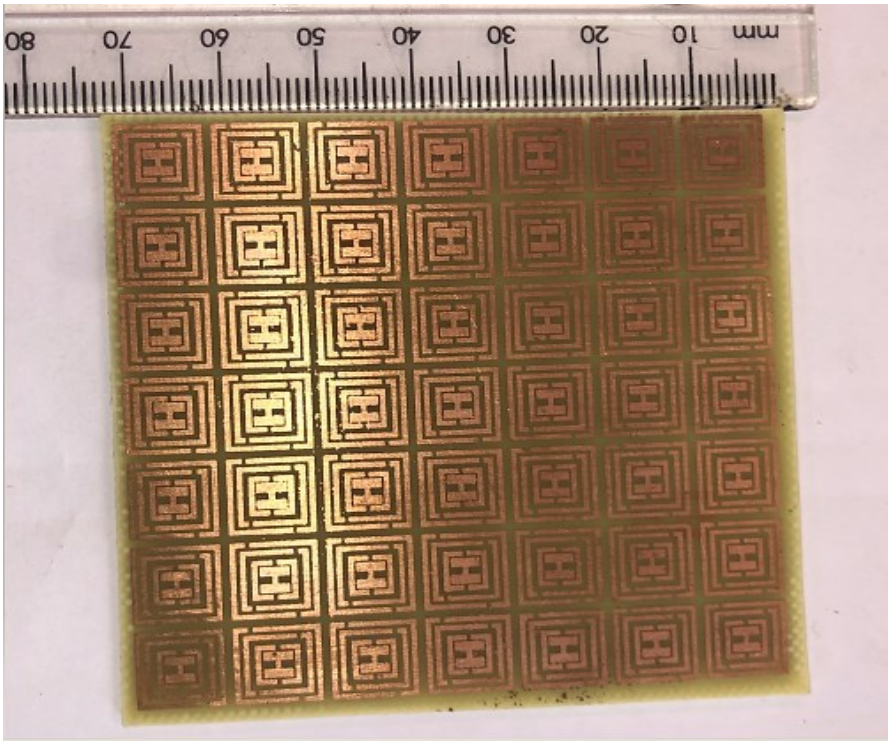

(b)

Figure 4.6: 7 X 7 Array Structure of the ISMeTM: (a) Array and Unit Cell (b) Fabricated Array.

Table 4.7 Dimensional Parameters of the 7 X 7 Array Cell

Parameter	Dimension (mm)	Parameter	Dimension (mm)
Wm	70	R3	2.8
Lm	70	Rt	0.5
Sw	10	Rl	2
Ls	10	W	0.5
Rw	1.25	sh	1.6
R1	9	ch	0.035
R2	4	g	0.5

The effective parameters of ISMeTM superstrate were extracted by using the NRW techniques equations (2.32) – (2.42). The S-parameters and the effective parameters of the proposed 7 x 7 ISMeTM array superstrate are shown in Figure 4.7. The operating frequency range is from 3 to 18 GHz. The simulated S_{21} parameter shows resonance frequencies at 4.31, 5.45, 6.07, 7.42, 8.29, 10.85, 12.38, and 15.01 GHz in the C, X, and Ku- bands. The S-parameters for the unit cell and 7 x 7 ISMeTM array are presented in Figure 4.7(a). The real and imaginary values of the effective permeability and permittivity are shown in Figure 4.7(b). The structure produces permittivity characteristics for the frequency ranges 4.3, 5.1-5.5, 5.9-8.2, and 9.1-18 GHz. The 7 x 7 ISMeTM array exhibit multi-band properties.

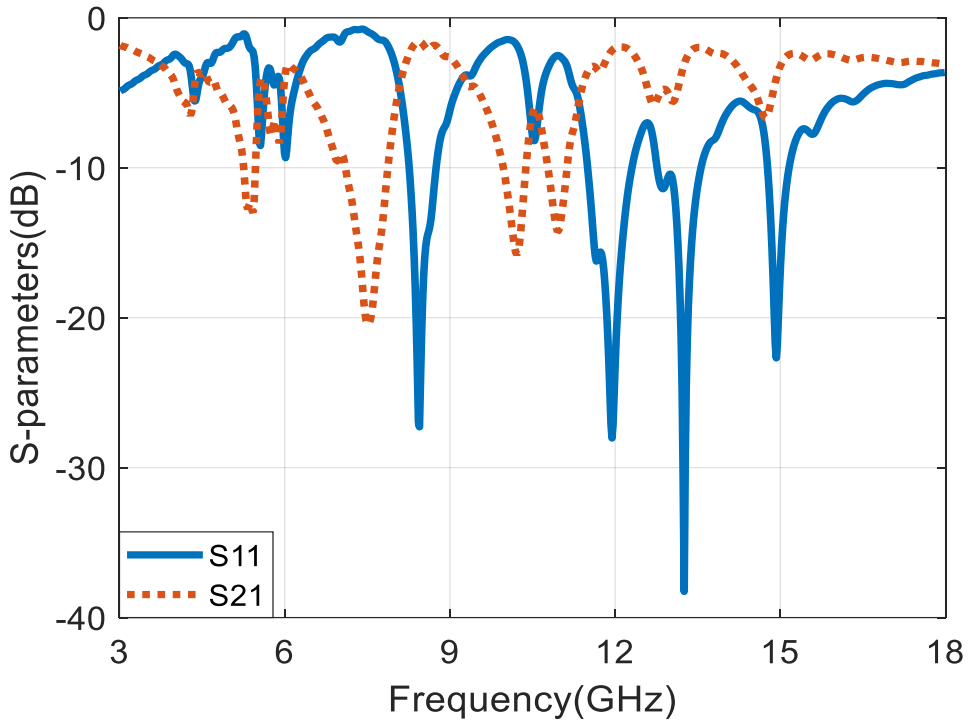

(a)

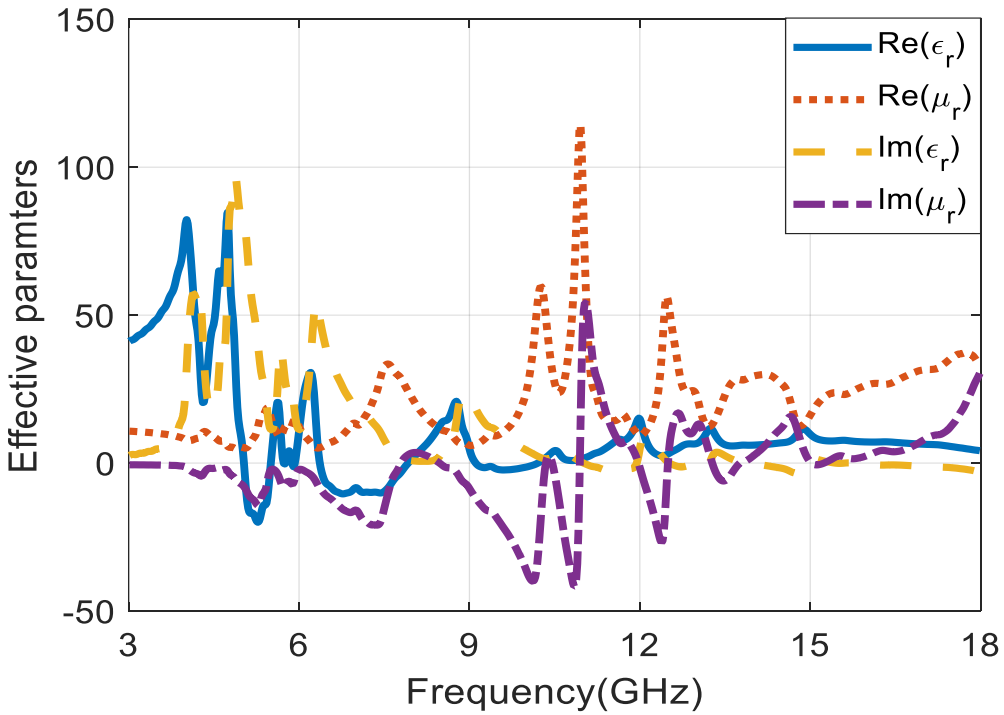

(b)

Figure 4.7: ISMeTM Unit Cell Analysis (a) S11 and S12 (b) Effective Parameters.

4.4.2 Rectangular Microstrip Antenna (ReMPA) Design

The geometrical structure and the side view of the rectangular microstrip patch antenna (ReMPA) are depicted in Figure 4.8. The substrate of the ReMPA is designed and fabricated on the FR-4 dielectric substrate and the SMA coaxial connector of 50Ω is used for the antenna feed. The antenna configuration and simulation are done using the Finite Integration Technique (FIT)- based electromagnetic CST simulator. The dimensions of the ReMPA are presented in Table 4.8. The geometric parameters of ReMPA such as width and length are calculated by using the transmission line model equations (2.15) – (2.24).

Table 4.8 Dimensional Parameters of the ReMPA

Parameter	**Dimension (mm)**	**Parameter**	**Dimension (mm)**
Wg	24.96	Gpf	0.085
Lg	20.98	Fi	4.36
Wp = W	15.4	Sh	1.5
Lp	11.38	hc	0.035
Wf	3.01	ag	7

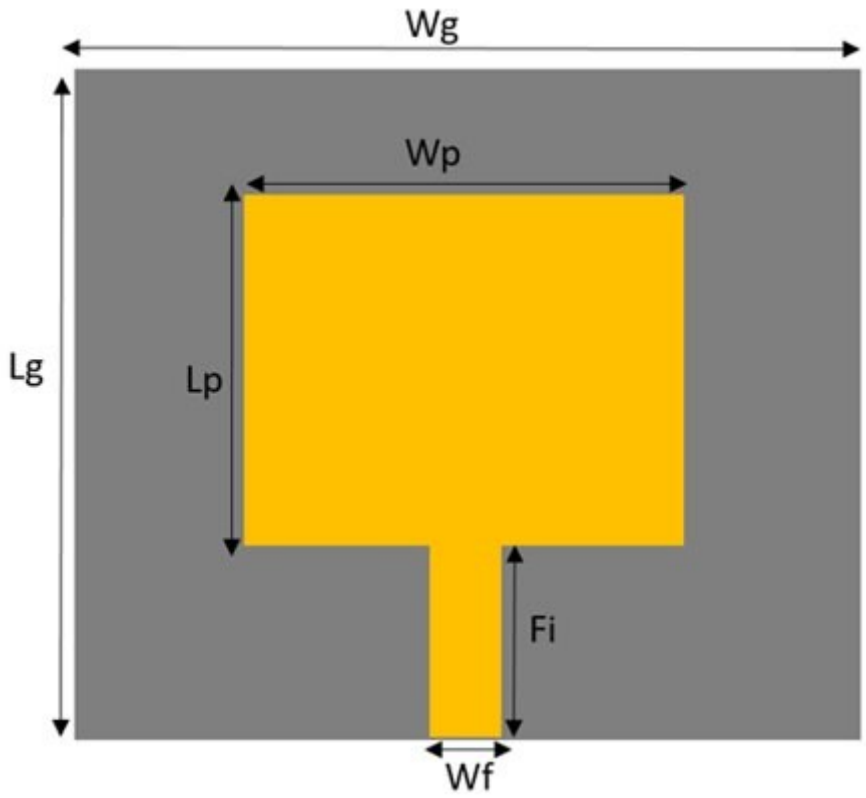

(a)

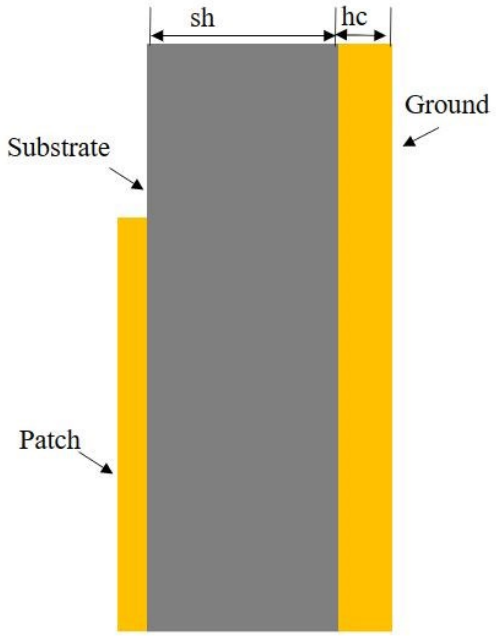

(b)

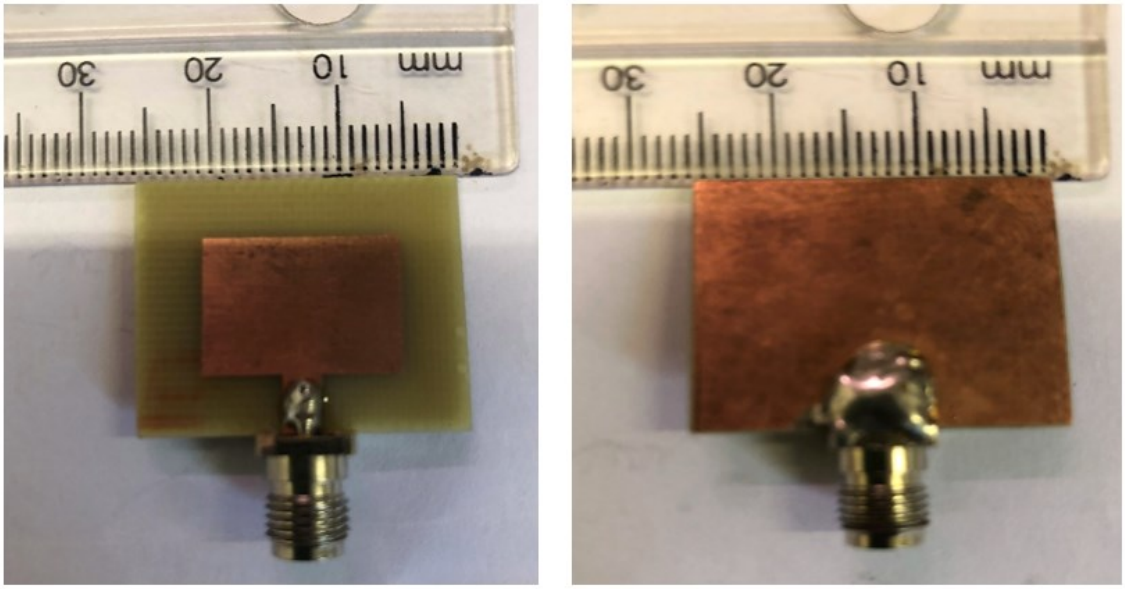

(c)

Figure 4.8: ReMPA Design (a) Top View (b) Side View (c) Fabricated Top and Back View.

The effect of the width of the patch (W) on the reflection coefficient is presented in Figure 4.9. The W is varied from 10 mm to 20 mm. It was observed at 10 mm the patch produced one resonance frequency at 11. 5 GHz with a return loss of -12.78 dB. At 14 mm, two resonance frequencies were observed at 6.03 GHz and 10. 4 GHz with a return loss of -13.4 dB and -34.97 dB. When the patch dimension was increased to 20 mm it produced three frequencies at 6.22 GHz, 10.6 GHz, and 11.5 GHz. The return loss at these frequencies is -11.1 dB, -18 dB, and -17.3 dB. It can be observed that the ReMPA has its better performance at 15.3 mm with three operating frequencies at 6.18 GHz, 9.09 GHz, and 11.48 GHz with a return loss of -17.9 dB, -17.6 dB, and -34.4 dB, respectively. The presented antenna is suitable for the C/X-band high gain multi-band wireless communication applications. The operating frequencies 9.09 GHz and 11.48 GHz are due to higher order 589 modes. The analysis of the resonant frequencies for different modes done using the equation (4.1) [11]

$$f_{r(m,n,p)} = \frac{c}{2\sqrt{\varepsilon_{reff}}}\sqrt{\left(\frac{m}{sh}\right)^2 + \left(\frac{n}{L_p}\right)^2 + \left(\frac{p}{W_p}\right)^2} \tag{4.1}$$

where $f_{r(m,n,p)}$ is the resonant frequency of the TM_{mnp} mode. For the computation of the resonant frequencies, the variation of the dielectric constant with the frequency is considered as given in Table

4.9. The computed and simulated resonant frequencies of ReMPA is given in Table 4.10. From the Table 4.10, it can be observed that the analytical resonant frequencies and simulated resonant frequencies are closely matched. Hence, using the higher mode resonant frequencies analysis and optimization in CST microwave studio, the presented antenna can be designed for the other specified frequency bands.

Table 4.9 Dielectric Constant and Loss Tangent at Various Frequencies

Parameter	Value (at 5.45 GHz)	Value (at 6.07 GHz)	Value (at 7.27 GHz)	Value (at 8.29 GHz)	Value (at 10.85 GHz)	Value (at 12.38 GHz)
Dielectric constant	4.34	4.33	4.32	4.31	4.29	4.28
Loss tangent	0.0235	0.0239	0.0245	0.0248	0.0250	0.0249

Table 4.10 Computed and Simulated Resonant Frequencies of Various TM_{mnp} Modes for ReMPA

S. No.	Mode	Resonant Frequency (Computed)	Resonant Frequency (Simulated)
1.	TM_{010}	6.043 GHz	6.18 GHz
2.	TM_{002}	8.950 GHz	9.09 GHz
3.	TM_{020}	12.138 GHz	11.48 GHz

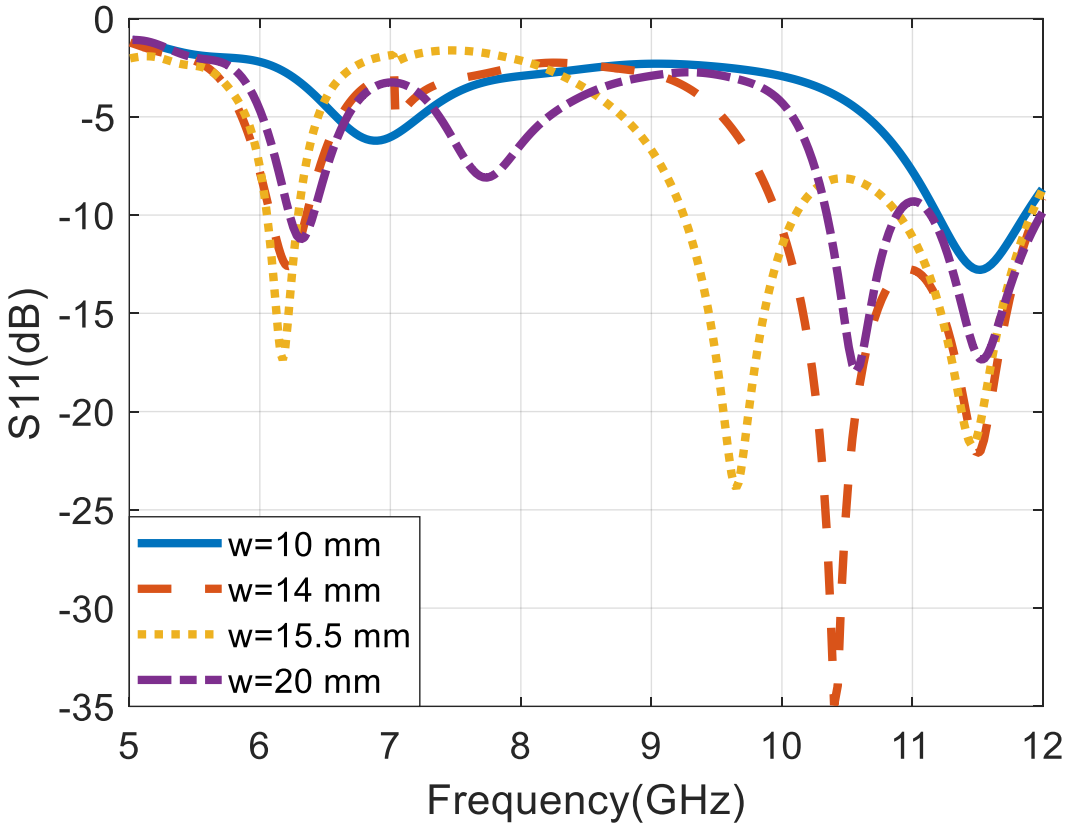

Figure 4.9: Variation of W

4.4.3 ReMPA based ISMeTM Superstrate

The configuration and detailed dimensions of the proposed antenna are shown in Figure 4.10(a) and Table 4.8, respectively. The final structure is obtained by using the superstrate designed with a 7 x 7 array of the proposed ISMeTM etched over the ReMPA. The configuration and the fabricated prototype of the proposed antenna are shown in Figure 4.10(b). The term ("ReMPA-based ISMETM") and ('proposed antenna") are interchangeably used throughout this chapter.

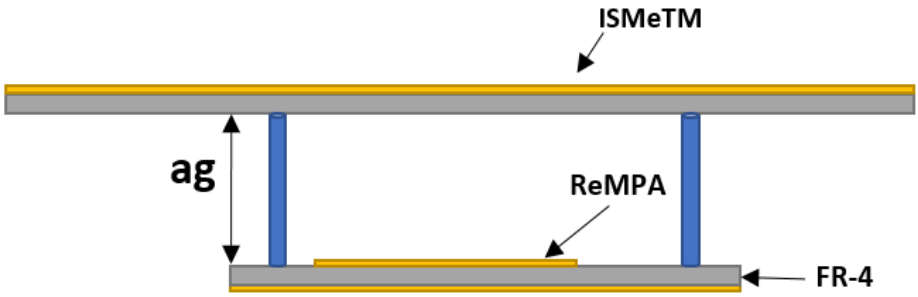

(a)

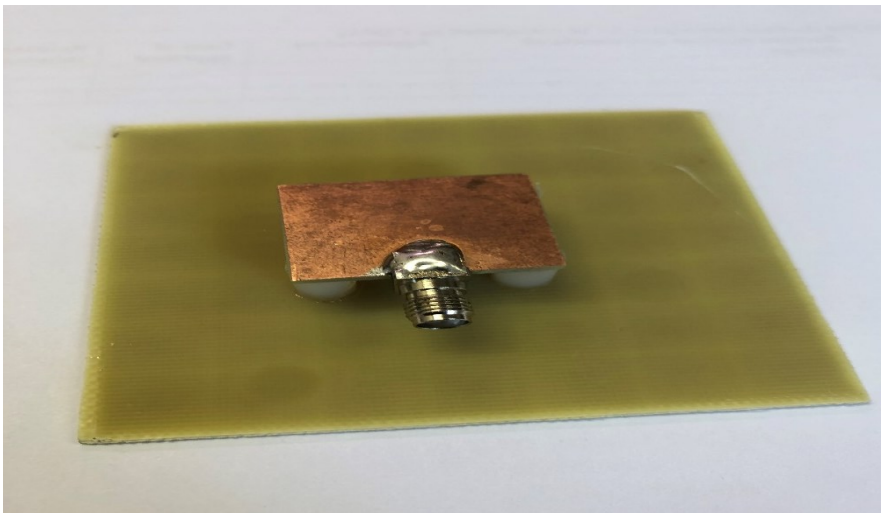

(b)

Figure 4.10: Proposed ReMPA Based ISMeTM (a) Configuration (b) Fabricated Prototype.

4.5 Equivalent Circuit of the ISMeTM based ReMPA

The equivalent circuit of the proposed antenna is antenna, which is covered with the ISMeTM superstrate is depicted in Figure 4.11. The RLC circuit with *Rm, Cm*, and *Lm* is used to model the ReMPA's radiating element. The ReMPA port is represented by Lp. The ISMeTM superstrate unit cell is modelled as resonant LC circuit with L1, L2, L3, L4, L5, L6, and L7 are the inductors, and C2, C3, C4, C5, C6, C7, C8, and C9 are the capacitors. The inductance (L) of the SSRR can be calculated by [156]

$$L = \frac{\mu_0}{2}\frac{L_{avg}}{4}4.86\left[\ln\frac{0.98}{\rho} + 1.84\rho\right] \tag{4.2}$$

where L_{avg}, μ_0, ρ denote the average length of the SSRR, permeability of free space, and filling ratio, respectively. The average length of the N split rings is given as $L_{avg} = 4[L_s - (N-1)(w+s)]$. The capacitance (C) of the SSRR can be expressed as [156]

$$C = \varepsilon_0\frac{N-1}{2}\left[2L_s - (2N-1)(w+s)\frac{\sqrt[K]{1-K_1^2}}{K(K_1)}\right] \tag{4.3}$$

The integral with argument *K1*, known as the elliptic integral of the first kind, is denoted by *K*, while ε_0 represents the permittivity of free space. The SSRR unit cells of the ISMeTM are connected in parallel in the resonator circuit. Mutual inductance (ML) occurs between the ISMeTM and the ReMPA as both structures are placed closely to each other. Under the loaded conditions, the ISMeTM superstrate's capacitance balances the ReMPA's inductance to produce good impedance matching.

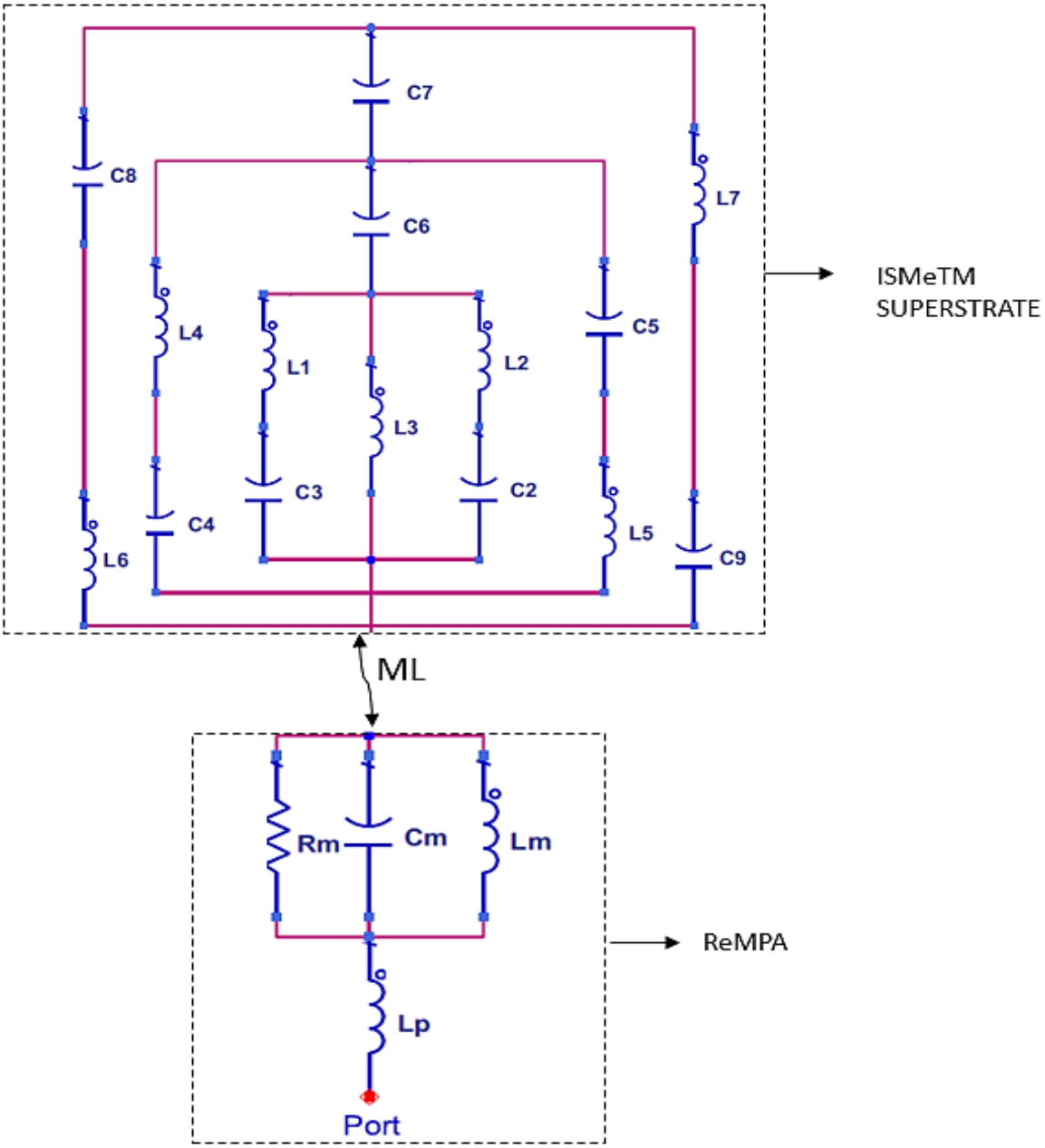

Figure 4.11: Equivalent Circuit of the Proposed ISMeTM-ReMPA.

4.6 Result of the Proposed ISMeTM (Design 2)

The simulated reflection coefficient S_{11} (dB) for the ReMPA and ReMPA-based ISMeTM is presented in Figure 4.12. It is seen that the ReMPA resonates at three frequencies of 6.18 GHz, 9.14 GHz, and 11.48 GHz, with corresponding bandwidths of 330 MHz, 700 MHz, and 800 MHz, respectively. When the I-shaped MeTM is integrated with the rectangular MPA, the resonant frequencies are at 6.18 GHz,

9.65 GHz, 11.5 GHz with a bandwidth of 240 MHz, 850 MHz, and 1010 MHz, respectively. The bandwidth of the first resonant frequency became narrower when the rectangular MPA was loaded with the superstrate. However, significant increment in the bandwidth and reduction in reflection coefficient for the second band and third band is observed.

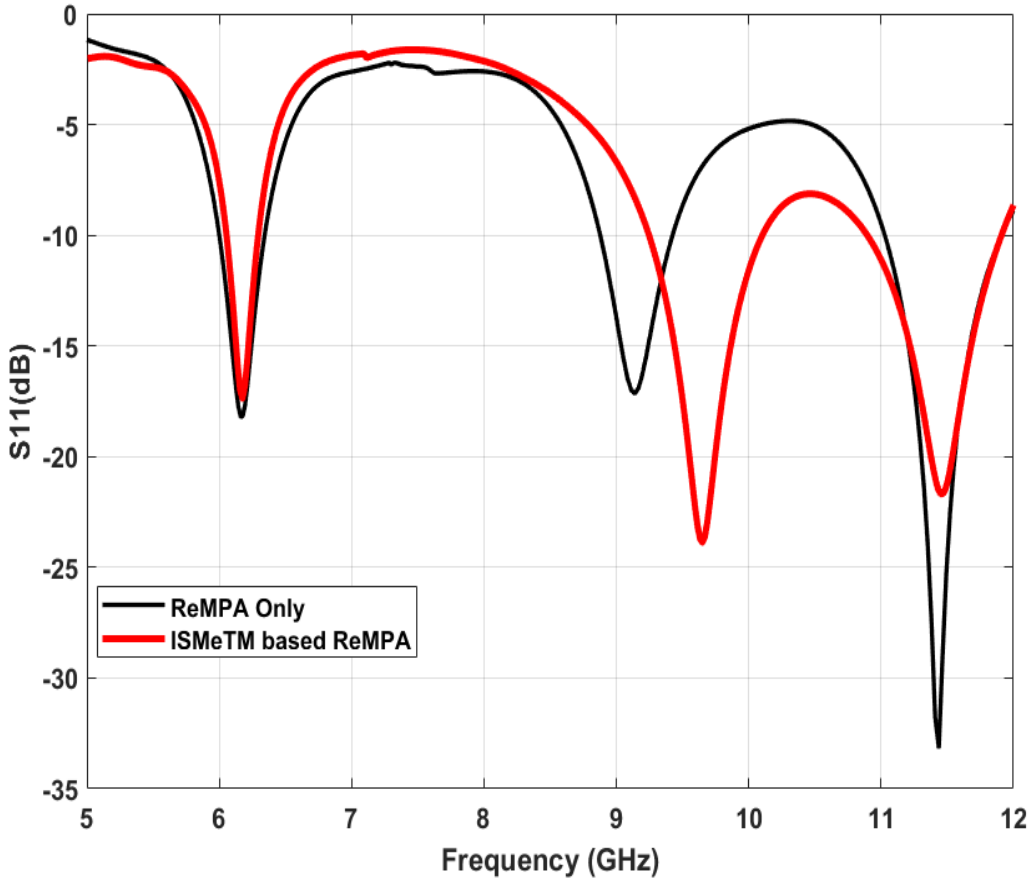

Figure 4.12: Simulated S-parameter of the ReMPA with and without ISMeTM Superstrate.

The Agilent 8719ET network analyzer was used to measure the proposed antenna. Figure 4.13(a) depicts the simulated and measured results of the S_{11} (dB) of the ISMeTM based ReMPA antenna. Figure 4.13(b) illustrates the experimental setup for measuring the fabricated antenna. The operating frequency for $S_{11} \leq$ -10 dB is 6.18 GHz, 9.94 GHz, and 11.7 GHz. A little disparity can be observed between the simulated and measured S-parameter, this can be attributed to fabrication tolerance, variation of material specification, calibration of the network analyzer, and impedance from the connector soldering.

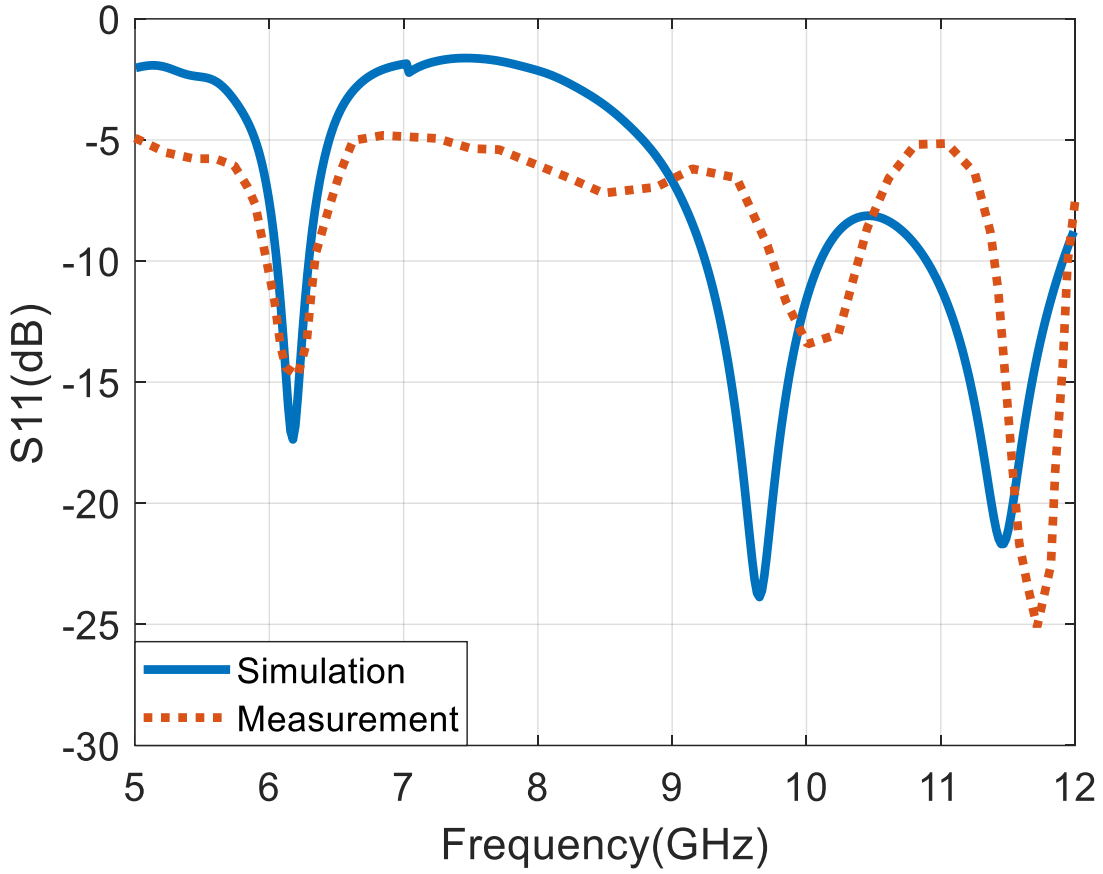

(a)

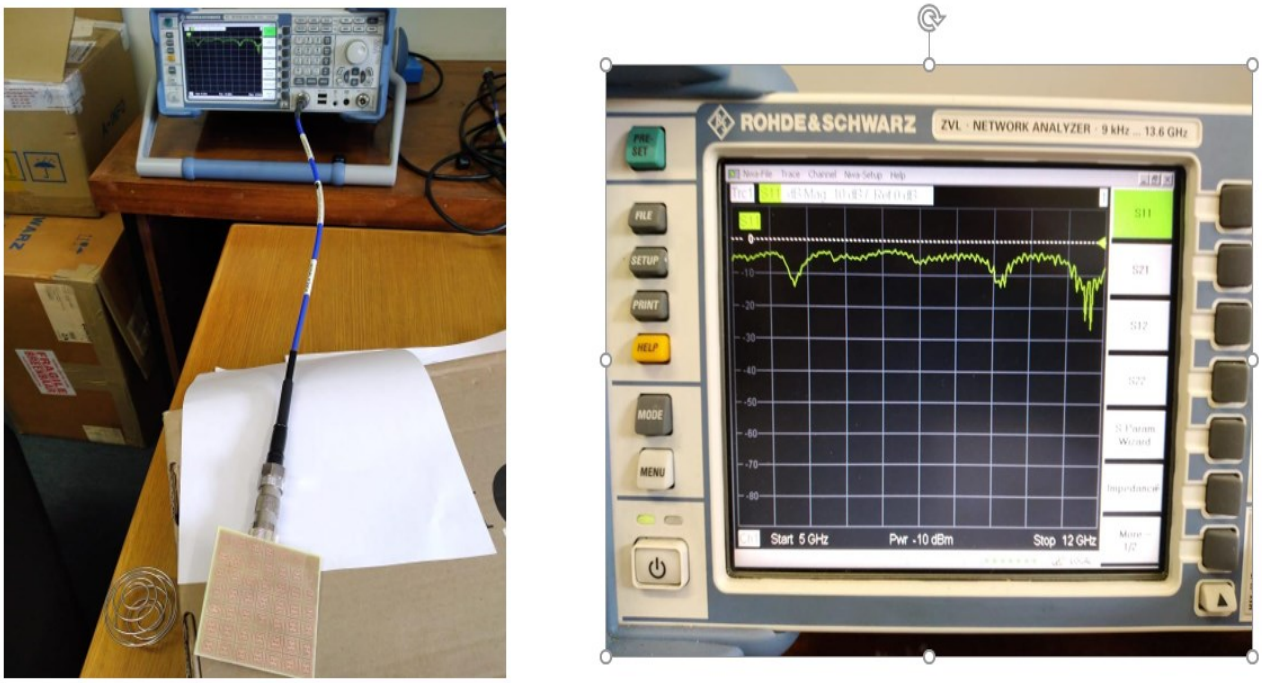

(b)

Figure 4.13: Reflection coefficient S_{11} measurement: (a) Reflection coefficient versus frequency, (b) Measurement Setup.

Figure 4.14 depicts the reflection coefficient of the proposed antenna at various heights (ag). The plastic spacers separate the superstrate and rectangular MPA. The spacers have no significant impact on the antenna's performance. The distance between the rectangular MPA and the I-shaped MeTM superstrate is varied from 6 mm to 15 mm. The reflection coefficient characteristics for the four values of ag i.e. ag =6mm, ag =7mm, ag =10 mm and ag =15mm are presented in Figure 4.14. It is observed that for the first and second bands ag = 7 mm provides minimum reflection coefficient along with the wide bandwidth. However, for the third band, ag =15 mm provides the minimum reflection coefficient with almost same bandwidth as of ag=7 mm. Considering the overall performance for all the frequency bands, for ag = 7 mm, the antenna gives the optimum performance.

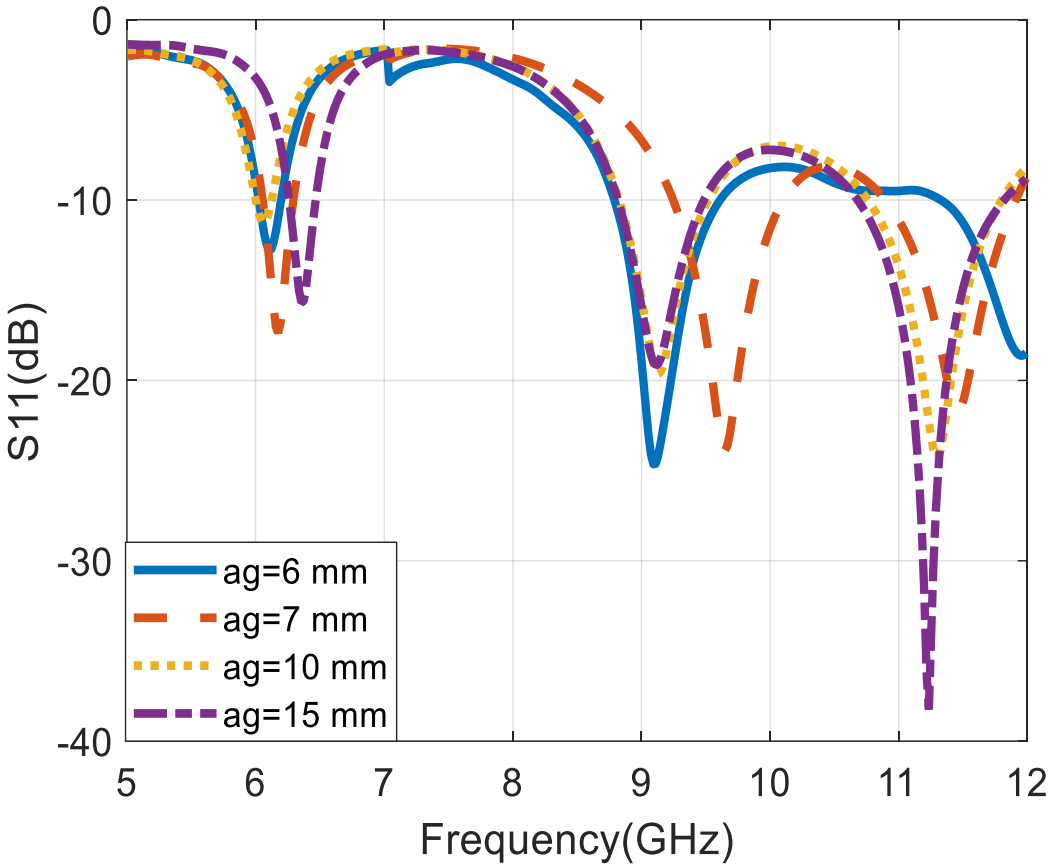

Figure 4.14: S-Parameter for different Values of ag.

The normalized simulated 2-D radiation patterns of the ReMPA and the proposed antenna at three operating frequencies are shown in Figure 4.15. The E- plane (phi = 0^0) and H- plane (phi = 90^0) patterns at resonant frequency 6.18 GHz show a broadside radiation pattern. In Figure 4.15(b), an omnidirectional radiation pattern is observed at 9.65 GHz. In Figure 4.15(c), the antenna shows a dipole-like pattern at E-plane and an omnidirectional pattern at the H-plane.

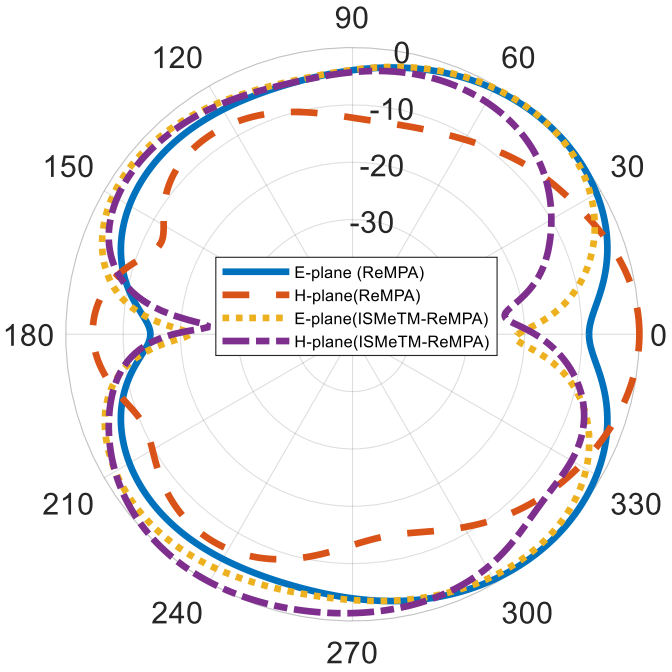
90
120
60
150
30
180
0
210
330
240
300
270
0
-10
-20
-30
E-plane (ReMPA)
H-plane(ReMPA)
E-plane(ISMeTM-ReMPA)
H-plane(ISMeTM-ReMPA)

(a)

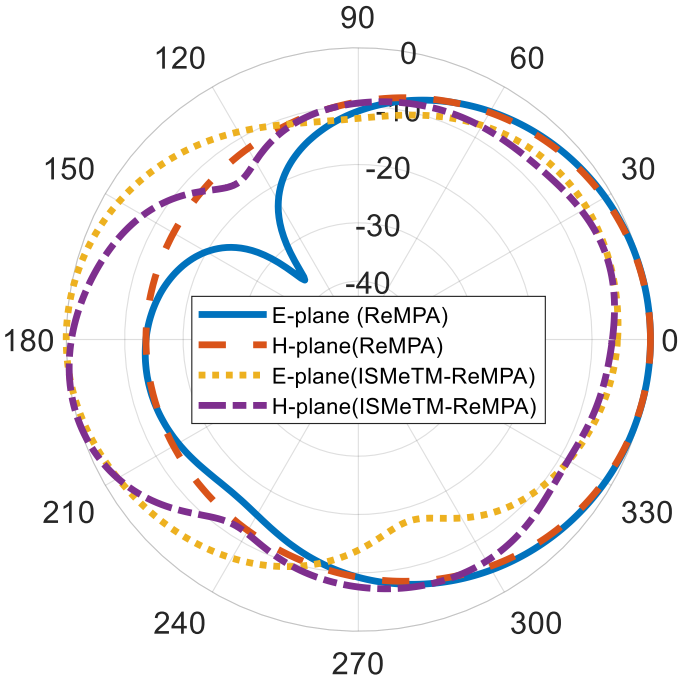
90
120
60
150
30
180
0
210
330
240
300
270
0
-20
-30
-40
E-plane (ReMPA)
H-plane(ReMPA)
E-plane(ISMeTM-ReMPA)
H-plane(ISMeTM-ReMPA)

(b)

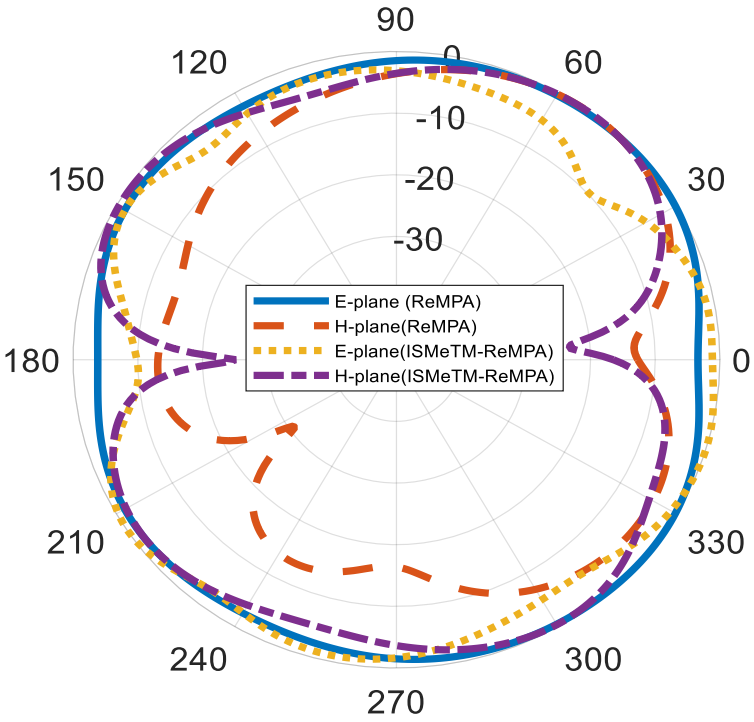

(c)

Figure 4.15: Radiation parameters of the ReMPA and Proposed Antenna (a**)** 6.18 GHz (b) 9.65 GHz (c) 11.5 GHz**.**

The realized gain for both rectangular MPA and the proposed antenna is presented in Figure 4.16(a) and Table 4.11. It can be observed that there is significant improvement in the gain of the antenna integrated with the I-shaped MeTM array. The gain of the rectangular MPA increased significantly for all frequencies for the antenna integrated with the I-shaped MeTM array superstrate. At 6.18 GHz the gain increased from 2 dBi to 4.19 dBi, while at 9.09 GHz a gain of 0.1 dBi was obtained by rectangular MPA. As the I-shaped MeTM array is integrated with the rectangular MPA, an increase in the operating frequency and gain of 2.4 dBi is achieved. The gain increment from 3.23 dBi to 5.68 dBi was experienced at 11.5 GHz. The gain enhancement in % for various frequencies is given. The radiation patterns of the antenna at 6.18 GHz, 9.09 GHz and 11.5 GHz are shown in Figure 4.16(b), Figure 4.16(c), and Figure 4.16(d), respectively. It can be observed that the simulation and measurement patterns are in good agreement.

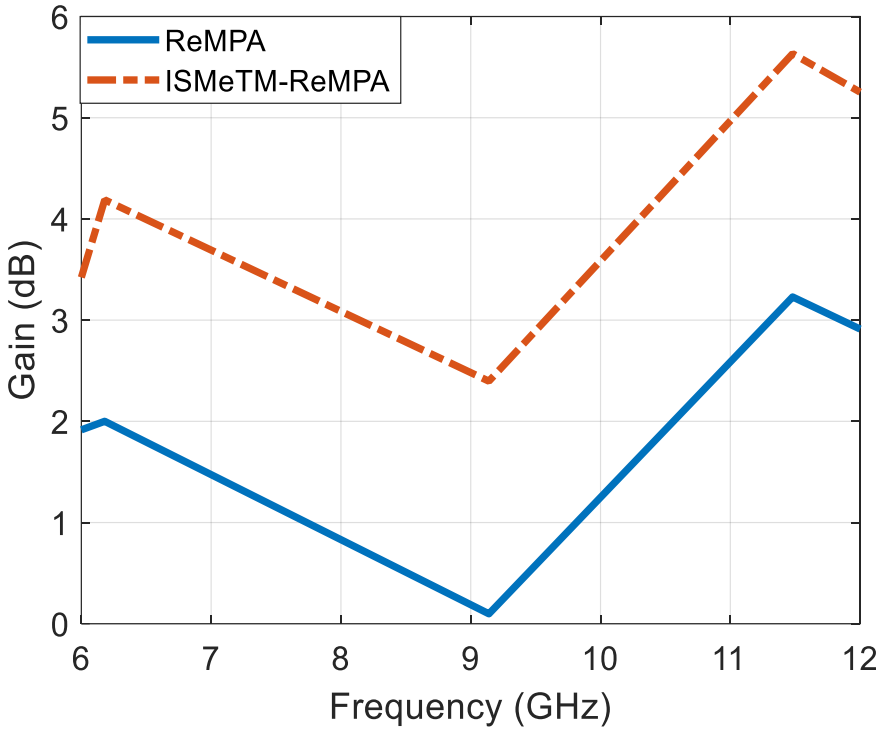
ReMPA
ISMeTM-ReMPA
Gain (dB)
Frequency (GHz)
0
1
2
3
4
5
6
7
8
9
10
11
12

(a)

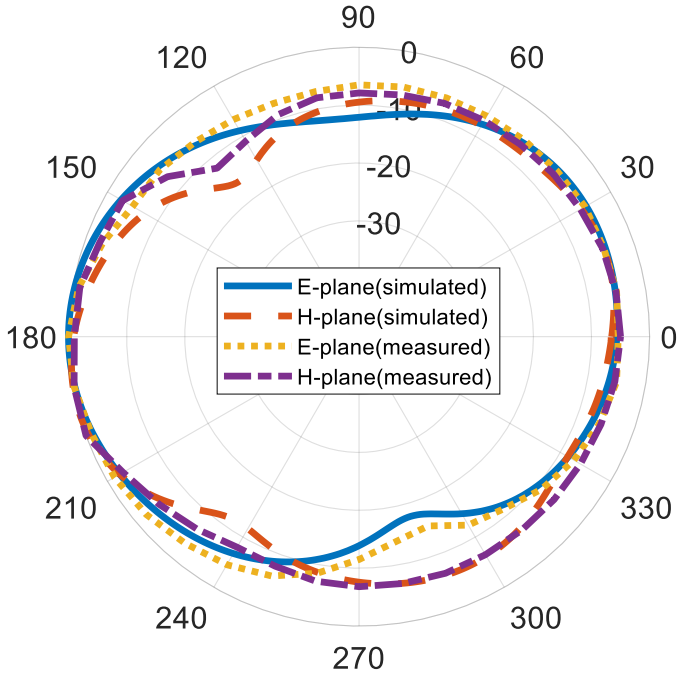
90
120
60
150
30
180
0
210
330
240
300
270
-20
-30
E-plane(simulated)
H-plane(simulated)
E-plane(measured)
H-plane(measured)

(b)

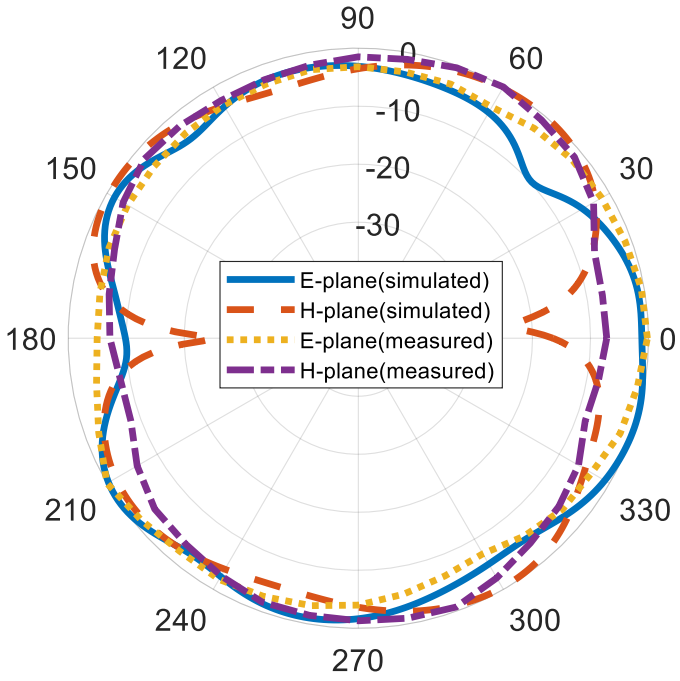

(c)

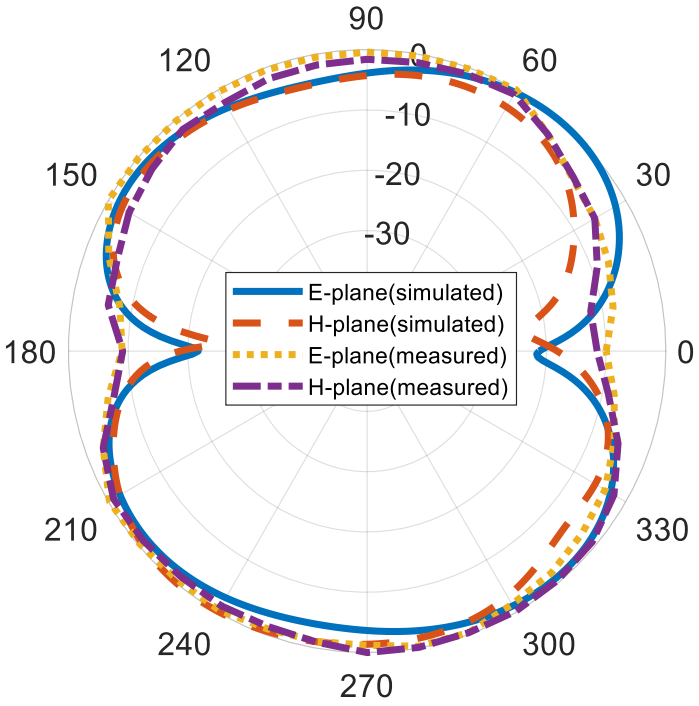

(d)

Figure 4.16: Radiation Characteristics of the Proposed Antenna**:** (a) Realized Gain (b**)** Radiation Patterns at 6.18 GHz **(**c) Radiation Patterns at 9.65 GHz (d) Radiation Patterns at 11.5 GHz.

The angular 3 dB beamwidth, main lobe direction, total and radiating efficiency, maximum gain, and directivity of the proposed antenna are presented in Table 4.12. It can be observed that, as the operating frequency of the antenna increases, the total and the radiating efficiency of the antenna decreases.

Table 4.11 Realized Gain of the ReMPA and the Proposed Antenna

S. No.	Frequency	Gain of rectangular MPA	Gain of proposed antenna	Gain enhancement
1.	6 GHz	1.91 dBi	3.42 dBi	41.62%
2.	6.18 GHz	2 dBi	4.18 dBi	65.17%
3.	9.14 GHz	0.09 dBi	2.39 dBi	69.83%
4.	11.48 GHz	3.22 dBi	5.63 dBi	74.18%
5.	12 GHz	2.91 dB	5.25 dBi	71.44%

Table 4.12 Radiation Parameters of the ISMeTM-ReMPA

Antenna parameters	ReMPA			Proposed Antenna		
	6.18 GHz	**9.14 GHz**	**11.44 GHz**	**6.18 GHz**	**9.65 GHz**	**11.5 GHz**
Angular beamwidth (3dB) (phi=0^0)	91.1	152.0	64.5	66	57	81.1
Angular beamwidth (3dB) (phi=90^0)	98.0	74.8	63.1	43.9	93	56.3
Main lobe direction (phi= 0^0)	0.0	35	0.0	180	49	146
Main lobe direction (phi= 90^0)	30.8	42	54	168	127	51
Radiating efficiency (dB)	-3.670	-5.929	-5.042	-3.894	-3.196	-2.176
Total efficiency (dB)	-4.074	-9.530	-5.352	-4.059	-3.199	-2.168
Maximum gain (dB)	2.000	0.098	3.229	4.192	2.388	5.679
Maximum directivity (dB)	5.671	6.020	8.260	8.005	5.697	7.073

The comparison of the existing works with the ReMPA-based ISMeTM is presented in Table 4.13. From this comparison, it can be observed that the proposed low-cost antenna provides multiband operation,

high gain, and high gain enhancement. Various antenna parameters confirm the suitability of the proposed antenna for multiband C/X-band wireless systems such as Wi-Fi devices, radar systems, short- and long-range tracking systems.

Table 4.13 Comparison of the ReMPA Based ISMeTM with Related Literature

Ref	Dimension $(mm)^2$	Resonance Frequency (GHz)	Substrate	Gain (dBi)	Gain enhancement	Remarks
[155]	180 ×180	2.6	Taconic	9.33	94.7%	Single band
[156]	165 ×165	1.66 2.02 2.40 2.48 2.77	$\varepsilon_r = 2.65$	5.8 0.8 4.2 3.6 8.2	--	Not a low-cost FR-4
[157]	50 ×--	3.51 4.86 7.8	FR-4	--	--	Gain not reported
[158]	48 ×48 m	1.9 2.45 5	Rogers RT5870	1.64 2.07 4.06	--	Low gain
[159]	27.75 ×16.08	2.4 4.1 5.2	FR-4	0.37 1.61 1.88	--	Low gain
[160]	61.25 ×61.25	2.4	FR4 Metamaterial	6.56	30.17%	Single-band, Low gain enhancement
[161]	31 ×30	2.47 3.62	FR-4	1.88 1.35	--	Dual-band, low gain
[162]	45 ×35	1.13 2.47 2.74	FR-4	3.73 6.18 1.35	--	Low gain for two bands
[163]	56 ×56	1.75-2.0 3.01-4.18	FR-4	1.5 2.05		Dual-band, low gain
[164]	25 ×21.4	5.8	FR-4	5.27, 4.04	32.67%	Single band, low gain enhancement
[165]	14 ×12	28	Roger RT/Duroid 6006 and Roger RT/ Duroid 5880	6.36 (5)	37.02%	Single-band, low gain enhancement
[166]	46 ×32	2.45 3.5 4.65	FR4	2.76 (2.4) -7.4 (-8.2) 3.68 (1.4)	8.62% 20% 68.84%	Low gain, Low gain enhancement

[167]	70 ×70	2.53 5.77	FR4	3.64 3.84		Dual band, low gain
[168]	50 ×50	2.41 5.8	FR4	0.29 1.17		Low gain
Proposed antenna	70 ×70	6.18 9.65 11.5	FR-4	4.19 2.4 5.68	65.17% 69.83% 74.18%	Triple-band, low-cost FR4, high gain, high gain enhancement

4.7 Chapter Summary

A square SRR metamaterial (Design 1) for gain enhancement of Microstrip antenna have been proposed and presented in this chapter. The antenna shows maximum directivity of 6.838 *dBi* at 6.0 GHz and a maximum gain of 5.278 *dB* at a single operating band of 5.8 GHz. It can be seen from the various comparison shown at different frequencies that the best performance is obtained at 5.8 GHz. The square SRR metamaterial has shown an improvement in the performance of the antenna. This work was extended by introducing the I-shaped metamaterial superstrate which consists of a 7 x 7 array of unit cells to ReMPA (Design 2). A multi-band rectangular MPA integrated with the I-shaped MeTM superstrate array has been presented. The proposed antenna utilized a 7×7 I-shaped MeTM array to improve the performance of the antenna. The rectangular MPA and the I-shaped MeTM array are designed and fabricated etched on a FR4 substrate. The proposed antenna produces three resonance frequencies at 6.18 GHz, 9.65 GHz, and 11.45 GHz. The performance of Designs 1 and 2 can clearly be compared, with Design 2 having the better performance. Due to its characteristics, Design 2 is a good fit for multi-band wireless communications systems like Wi-Fi, radar, short- and long-range tracking systems, etc.

Chapter 5

Design of a Two-Port MIMO Patch Antenna using I-Shaped Metamaterial Superstrate for Triple-Band Wireless Applications

5.1 Introduction

This chapter presents the design and simulation of a triple-band two-port MIMO patch antenna using ISMeTM superstrate. The proposed antenna utilizes the 3 x 5 array of the ISMeTM as superstrate to improve the bandwidth, gain, and isolation between the ports of the MIMO antenna.

MIMO is vital in wireless communication system because it allows for the simultaneously use of multiple antennas for data transmission. This increases the data transmission rate, bandwidth efficiency, channel capacity, and robustness. However, mutual coupling (Mu-CP) is a major limitation which affects the performance of MIMO antennas (MIMO-ANT) [169-170]. Mu-CP occurs when there is an electromagnetic (EM) connection between the array elements of the antenna [171]. As several antennas elements are placed at closed proximity to each other, the electric field generated by one antenna alters the current distribution on the other antennas, therefore, the radiation pattern and input impedance of each array element are distributed based on the presence of the other elements. As already discussed in Chapter two, MeTMs are planar structures that can be easily integrated with the MPAs. This chapter proposes reducing mutual coupling in MIMO communication systems by utilizing the ISMeTM superstrate integrated with the MIMO antenna.

5.2 Geometry of the Two-Port MIMO-ANT (Antenna A)

The layout of the proposed two port MIMO-ANT system is shown in Figure 5.1. The antenna is designed using the transmission line model. The designed antenna is simulated and optimized using the CST studio suite. The antenna system consists of a ground plane placed on a FR-4 epoxy dielectric substrate

with thickness of 1.6 mm and dielectric constant of 4.3. The antenna's dimensions are given in Table 5.1. The overall dimension of the MIMO-ANT is 49.92 x 20.98 x 1.6 mm^3.

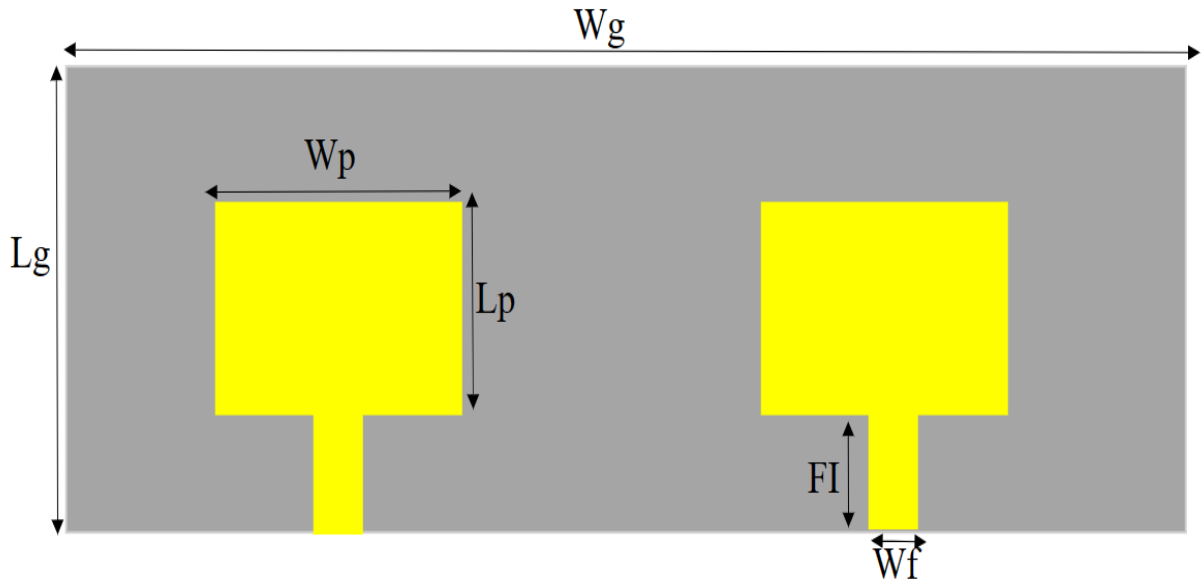

Figure 5.1: Two Port MIMO-ANT.

Table 5.1 Two Port MIMO-ANT Parameters

Parameter	Dimension (mm)	Parameter	Dimension (mm)
Wg	49.92	Wf	3.01
Lg	20.98	fi	4.36
Wp	15.4	hs	1.6
Lp	11.38	Hc	0.035

5.3 ISMeTM Superstrate based MIMO-ANT (Antenna B)

The ISMeTM superstrate is etched over the two port MIMO-Ant for the reduction of mutual coupling (Mu-CP). The superstrate is consisting of a 3 x 5-unit cell array of the ISMeTM. The superstrate is placed at a height of 10mm from the MIMO-ANT. The dimension of the superstrate is 57 x 35 x 1.6 mm^3. The proposed antenna is simulated using the CST studio. The configuration and the design of the proposed antenna is presented in Figure 5.2.

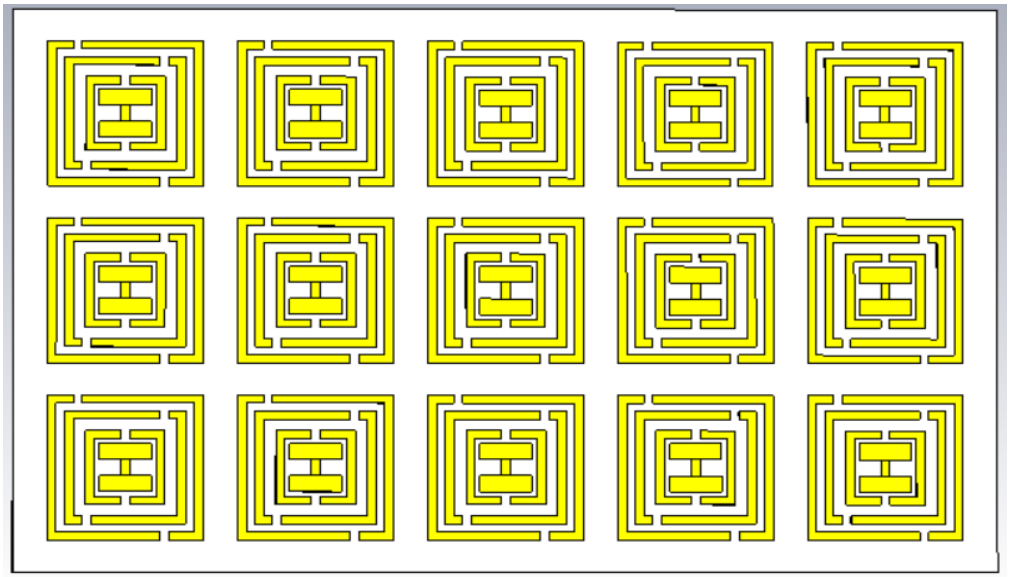

(a)

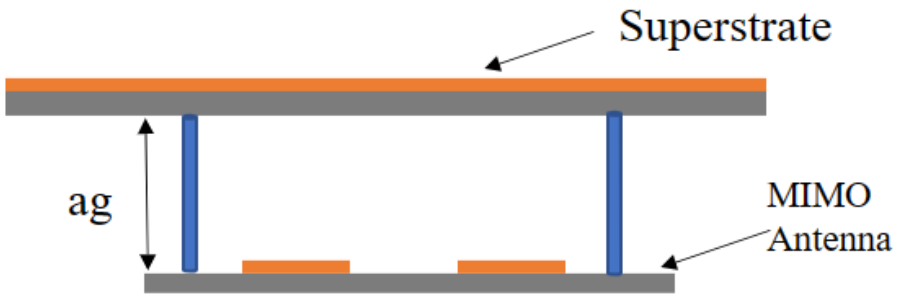

(b)

Figure 5.2: Proposed Antenna (a) 3 x 5 ISMeTM Array (b) Configuration.

5.4 Results and Discussion

The simulated results of the MIMO-ANT (Antenna A) and the ISMeTM superstrate-based MIMO-ANT (Antenna B) are presented in this section. The simulated results include the reflection coefficient, transmission coefficient, envelope correlation coefficient, diversity gain and the radiation patterns. Figure 5.3 depicts the reflection coefficients (S_{11}), (S_{22}) and the mutual coupling (S_{21}),(S_{12}) of Antenna A. It can be observed that Antenna A resonates at 6.05 GHz, 8.9 GHz, and 10.63 GHz with the

bandwidth of 330 MHz, 600MHz, and 630 MHz, respectively. The values of mutual coupling coefficient at 6.03 GHz, 8.9 GHz, and 10.63 GHz are -21.54 dB, -16.4 dB, and -27.2 dB, respectively.

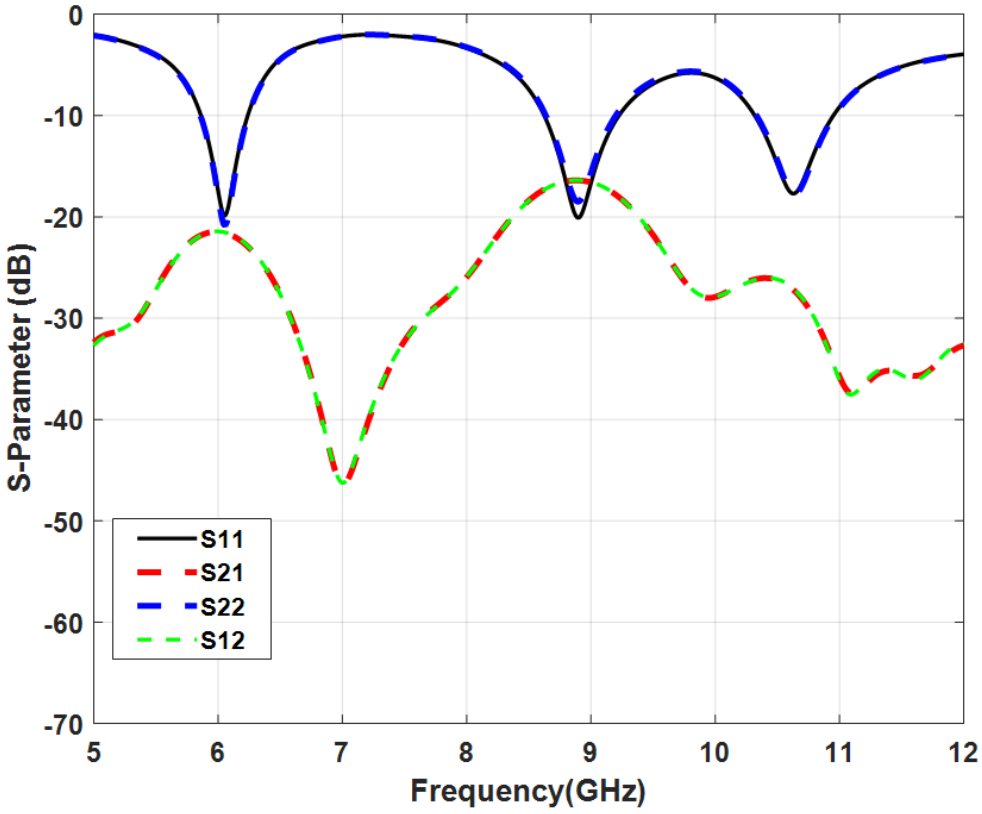

Figure 5.3: Reflection Coefficient and Mutual Coupling of the Antenna A.

Figure 5.4(a) illustrates the reflection coefficient of Antennas A and B. A slight increment in the operating frequencies is observed in Antenna B as it resonates at 6.31 GHz, 9.09 GHz, and 11.4 GHz with the bandwidth of 230 MHz, 890 MHz, and 730 MHz, respectively. The values of reflection coefficients for Antenna B for the second and third frequency bands are -36 dB and -40 dB, respectively. In Figure 5.4(b), the mutual coupling between for the Antennas A and B is presented. The Mu-CP at 6.31 GHz, 9.09 GHz and 11.4 GHz are -47.1 dB, -49.5 dB, and -49.3 dB, respectively. This implies that the Mu-CP for Antenna B is reduced by approximately 26 dB, 33 dB and 22 dB across the three operating frequencies as compared to Antenna A.

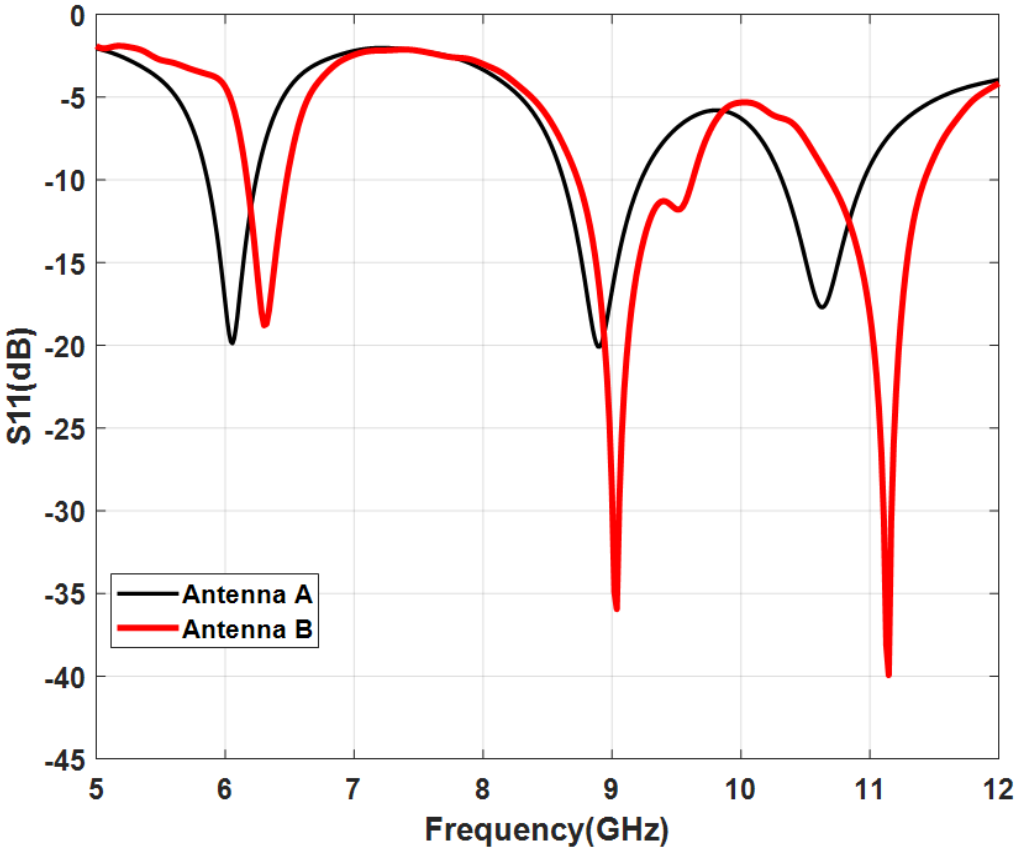
0
-5
-10
-15
-20
-25
-30
-35
-40
-45
S11(dB)
5
6
7
8
9
10
11
12
Frequency(GHz)
Antenna A
Antenna B

(a)

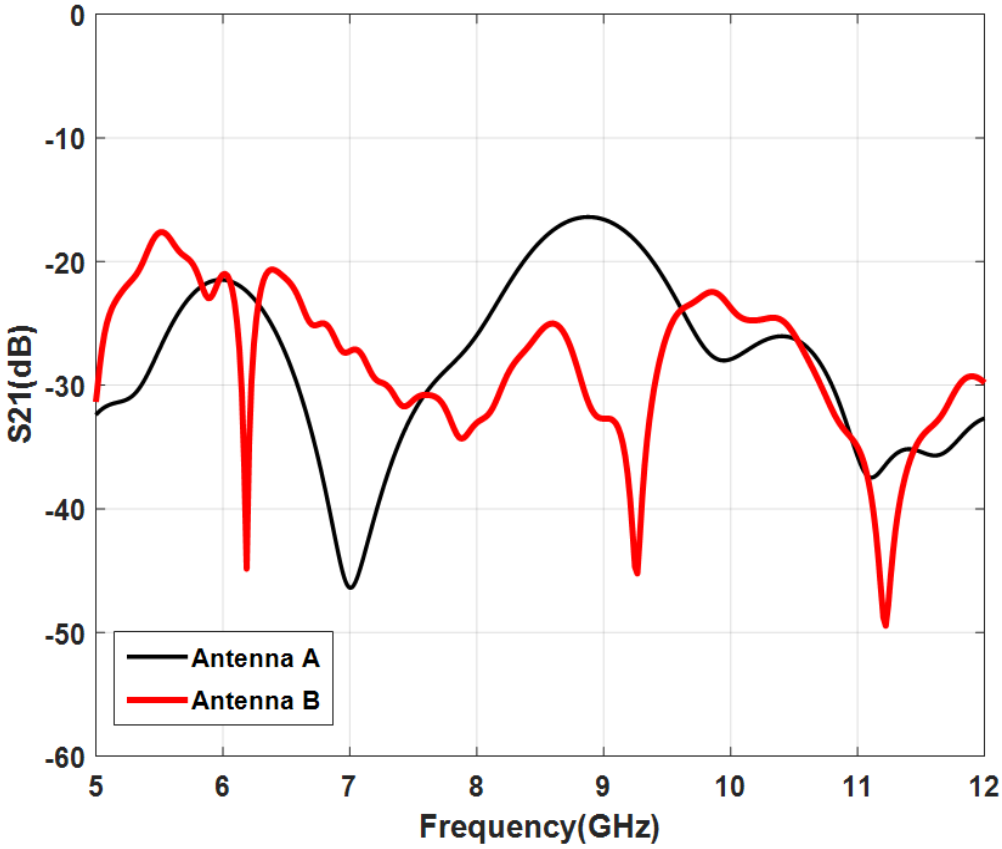

(b)

Figure 5.4: Reflection Coefficient and Mutual Coupling of Antennas A and B.

In Figure 5.5(a), it can be observed that the reflection coefficient behavior at second port is almost similar to that at the first port for both antennas. There is a slight change in the return loss of both Antennas. In Antenna A, the reflection coefficients are -20.81 dB, -18.5 dB, and -17.8 dB while for Antenna B, the reflection coefficients are -24.98 dB, -34.7 dB, and 30.06 dB, respectively. The mutual coupling for Antennas A and B is presented in Figure 5.5(b). The operating bands remains unchanged for both antennas. However, a slight change is observed in Antenna B at 9.09 GHz and 11.41 GHz with Mu-CP of -57.4 dB and -53.8 dB, respectively.

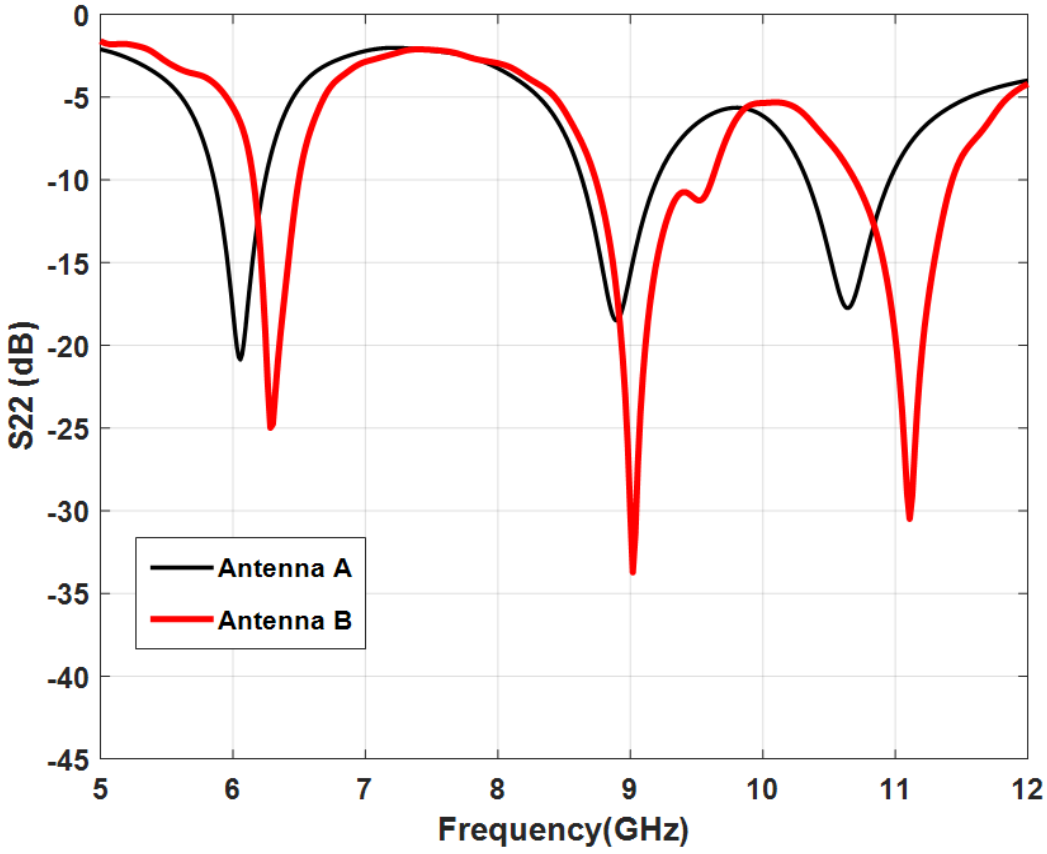
0
-5
-10
-15
-20
-25
-30
-35
-40
-45
S22 (dB)
5
6
7
8
9
10
11
12
Frequency(GHz)
Antenna A
Antenna B

(a)

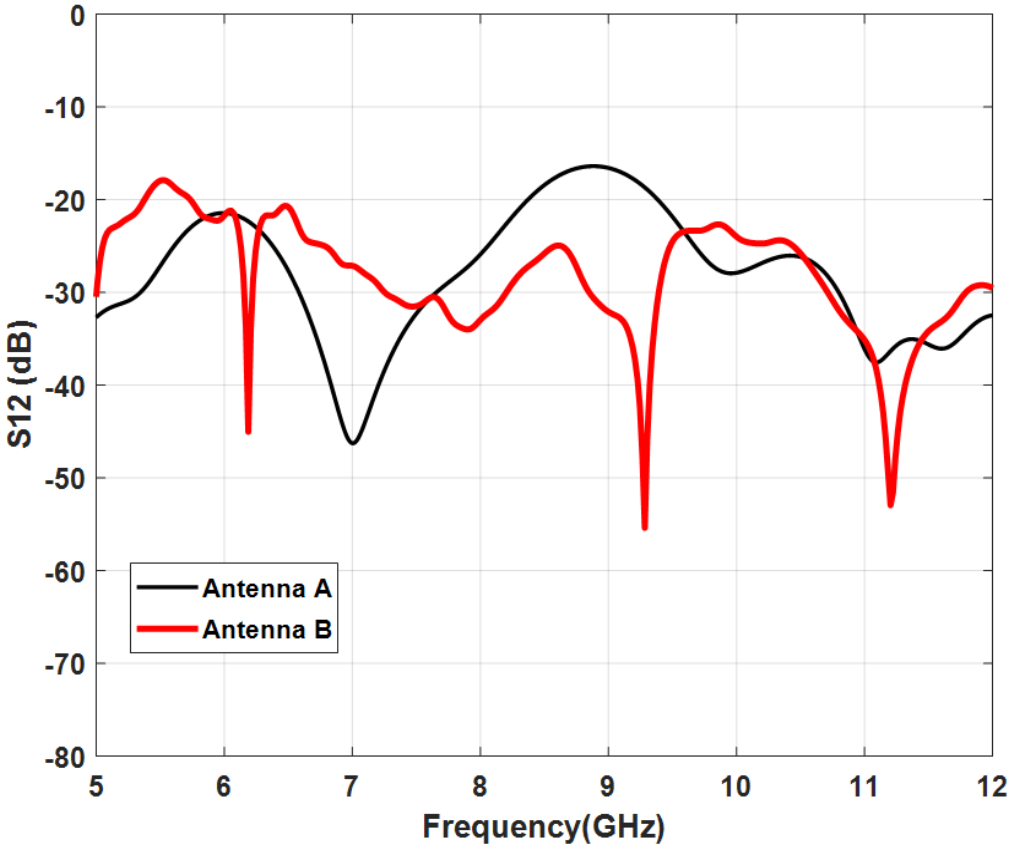

(b)

Figure 5.5: Mutual Coupling and Reflection Coefficient of Antennas A and B.

Figure 5.6 depicts the reflection coefficient of Antenna B at various heights (ag). The distance between the two port MIMO-ANT and the ISMeTM superstrate is varied from 6mm to 15mm. It can be observed that the antenna has its worst performance at ag = 15 mm while at ag = 7 mm, the antenna has its best performance over the desired frequency bands. The normalized radiation patterns of the proposed antenna (Antenna B) at the three operating frequencies are illustrated in Figure 5.7. The gain of Antenna A and Antenna B are presented in Figure 5.8. At 6.31 GHz the gain increased from 2. 21 dBi to 4.44 dBi, while at 9.08 GHz a gain of 6.64 dBi was achieved. A gain increment from 2.32 dBi to 7.38 dBi was obtained at 11.41 GHz.

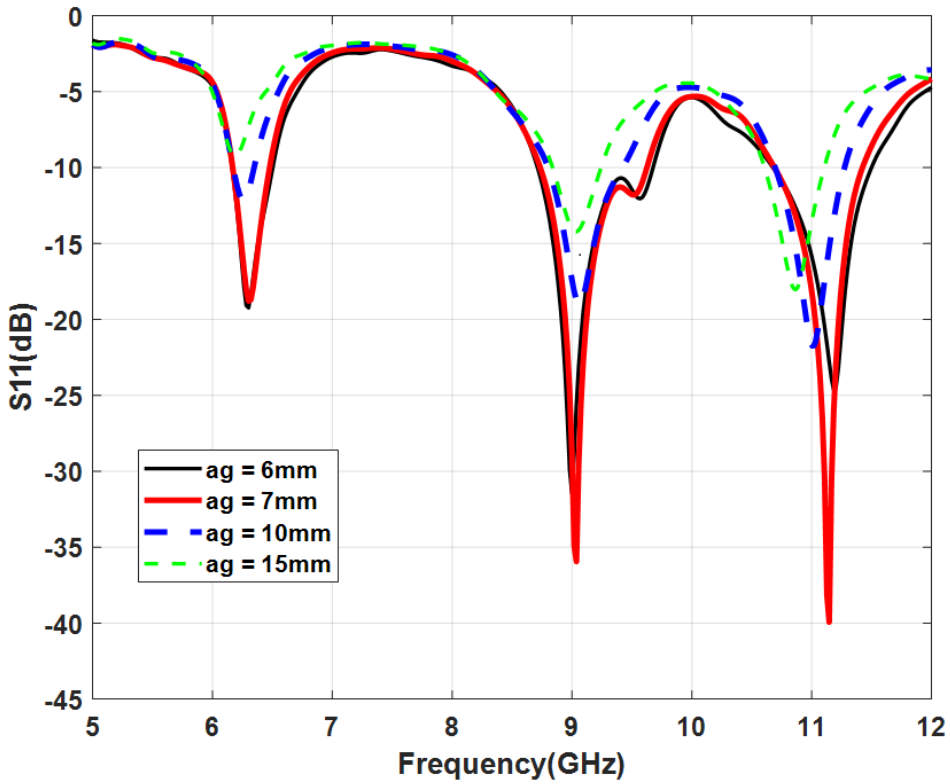

Figure 5.6: Reflection Coefficient of Antenna B various air gaps.

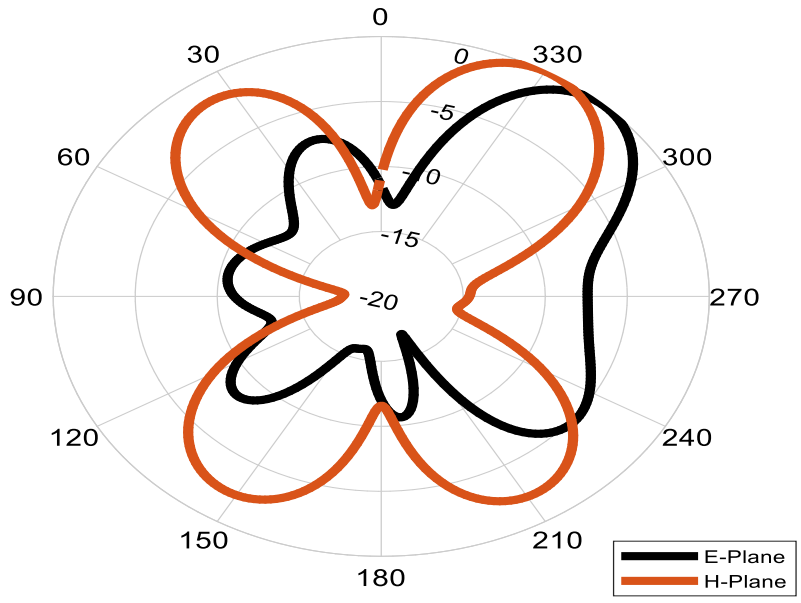

(a)

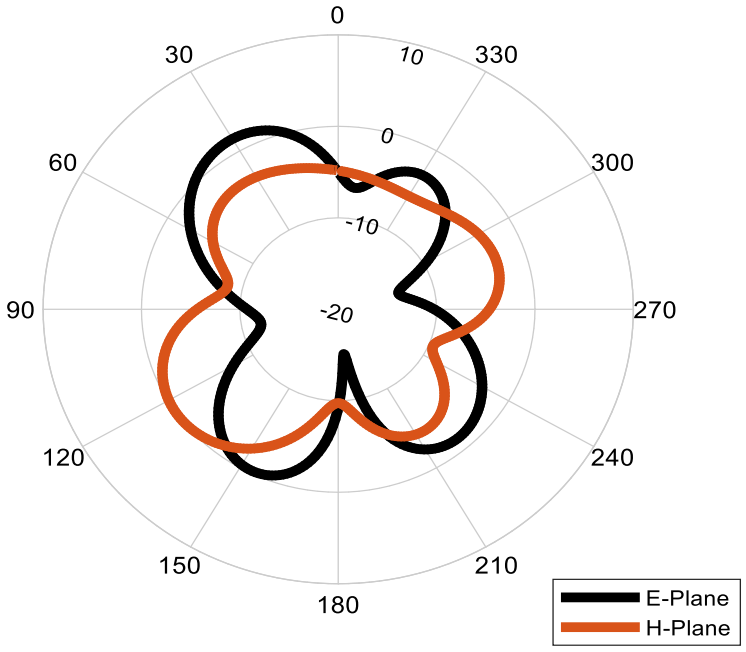

(b)

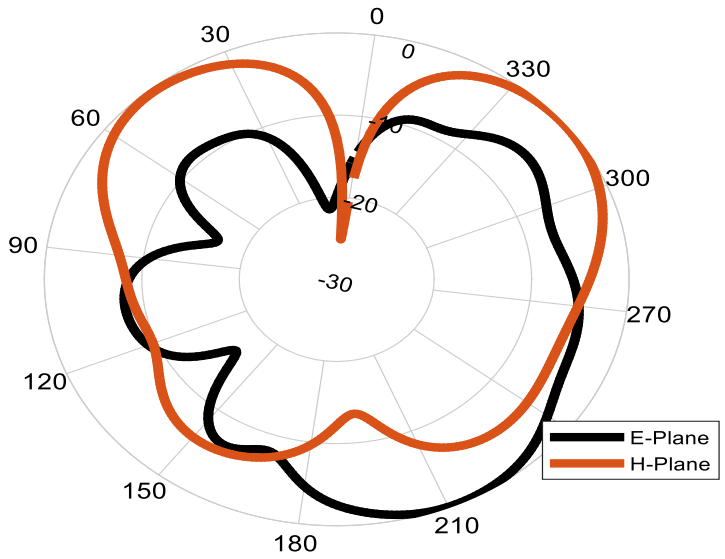

(c)

Figure 5.7: Radiation Patterns of Antenna B (a) 6.31 GHz (b) 9.08 GHz (c) 11.41 GHz.

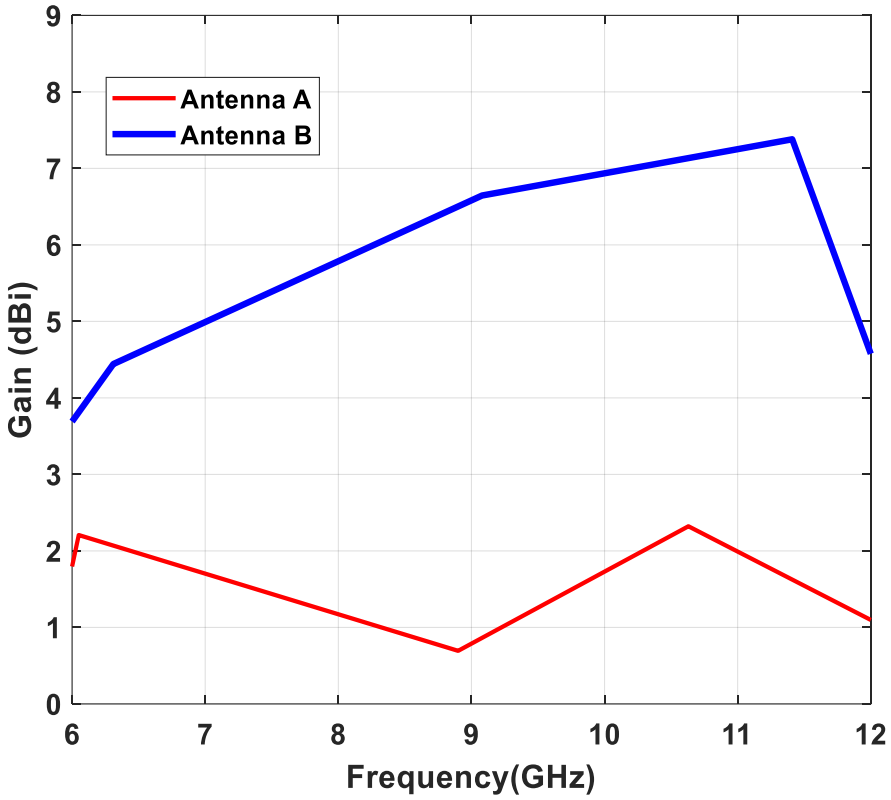

Figure 5.8: Realized Gain of Antennas A and B.

The envelope correlation coefficient (ECC) is a measure of the diversity performance of the MIMO system. The ECC can also be used to measure the distance between two closely antennas. In MIMO system, ρ_e shows the influence of diverse signal that reach the antenna elements by following distinct propagation paths. The value of ρ_e can be calculated by using the S-parameter [172,173]

$$\rho_e = \frac{|S_{11}^* S_{12} + S_{11}^* S_{12}|}{\left(1 - (|S_{11}|^2 + |S_{21}|^2)\right)\left(1 - (|S_{12}|^2 + |S_{12}|^2)\right)} \tag{5.1}$$

The value of ρ_e can also be calculated by using the radiated farfield patterns and it can be expressed as [173]

$$\rho_e = \frac{\left|\iint_{4\pi}[\overrightarrow{F_1}(\theta,\phi) * \overrightarrow{F_2}(\theta,\phi)\, d\Omega]\right|^2}{\left|\iint_{4\pi}[\overrightarrow{F_1}(\theta,\phi)]\right|^2 d\Omega \left|\iint_{4\pi}[\overrightarrow{F_2}(\theta,\phi)]\right|^2 d\Omega} \tag{5.2}$$

The far-field property of the MIMO system after exciting port is denoted as $\overrightarrow{F_1}(\theta,\phi)$. A low ECC is required for the robustness of the antenna. The ECC of the two antennas are shown in Figure 5.9. It is

evident that the ECC in the three various frequency bands is less than 0.009, indicating that the antennas are not correlated, and that Mu-CP has been significantly decreased.

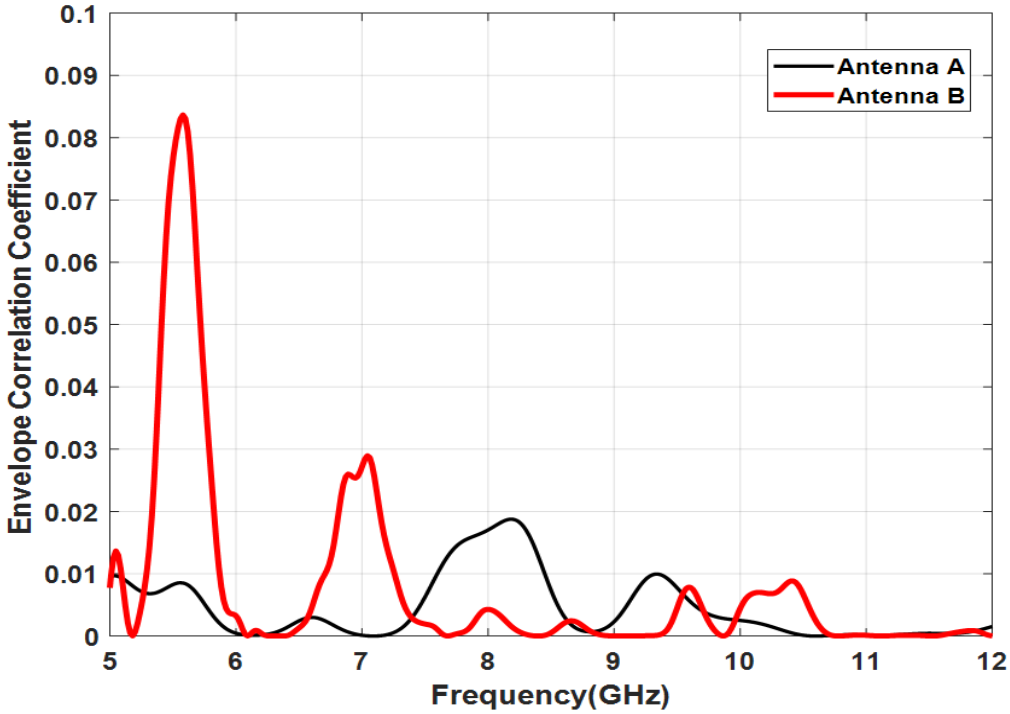

Figure 5.9: Envelope Correlation Coefficient of the Antennas A and B.

The diversity gain (DG) is another important parameter, which characterizes the MIMO antenna. The DG can be calculated using $DG = 10 \times \sqrt{1 - |ECC|}$ [174]. Figure 5.10 shows the DG of the Antennas A and B. It is seen that at the three resonance frequencies, the DG is closed to 10 dB.

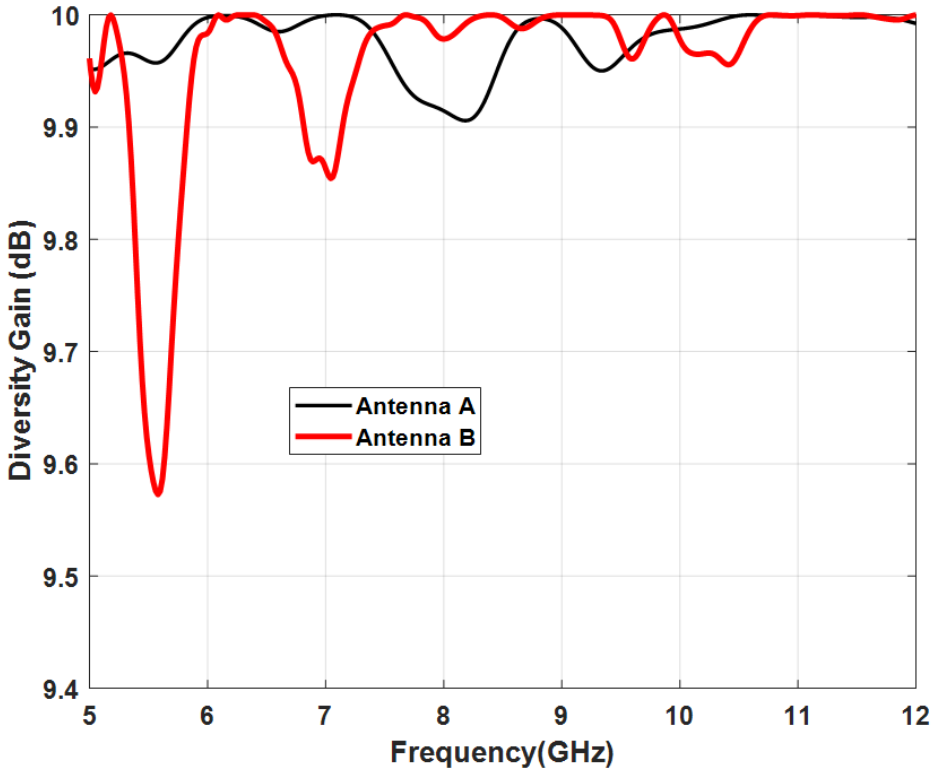

Figure 5.10: Diversity Gain of Antennas A and B.

Table 5.2 shows the 3 dB angular beamwidth, main lobe orientation, total and radiating efficiency, maximum gain, and directivity of Antennas A and B. The overall and radiating efficiency of the antenna are seen to reduce as the operating frequency of the antenna increases. The comparison of the proposed antenna with existing antennas is shown in Table 5.3. From this table, it can be observed that the proposed low-cost compact antenna provides high gain and high isolation. These parameters make the proposed MIMO antenna suitable for multiband communications.

Table 5.2 Radiation Parameters for Antennas A and B

Antenna parameters	**Antenna A**			**Antenna B**		
	6.05 GHz	**8.9 GHz**	**10.63 GHz**	**6.31 GHz**	**9.04 GHz**	**11.41 GHz**
Angular beamwidth (3dB) (phi=0^0)	94.0	52.5	99.8	45.5	35.9	56.2

Angular beamwidth (3dB) (phi=90^0)	98	134.8	62.4	53.6	38.7	59.6
Main lobe direction (phi= 0^0)	5	56	112	30	43	148
Main lobe direction (phi= 90^0)	4.2	54	49	125	31	44
Radiating efficiency (dB)	-2.058	-3.643	-2.458	-5.999	-4.641	-3.671
Total efficiency (dB)	-2.134	-3.787	-2.540	-6.575	-4.833	-3.753
Maximum gain (dB)	2.207	0.694	2.322	4.442	6.645	7.380
Maximum directivity (dB)	4.265	4.336	4.780	10.44	11.29	11.05

Table 5.3 Comparison with Related Works

Ref.	Dimension $(mm)^2$	Frequency (GHz)	Mutual coupling reduction (dB)	ECC	Gain (dBi)	Remarks
[175]	72 x 56	2.4 5.8	20 24	0.04	2.5	Large size, dual-band, low gain
[176]	150 x 75	3.5	20	0.4	Not Specified	Large size, single band
[177]	150 x 75	2.6 3.6 5.8	15 10 13	0.01	2.5 – 4.5	Large size, low gain
[178]	60 x 60	2.46 3.5	26 24	<0.002 <0.007	3.45 2.7	Large size, dual-band, low gain
[179]	65 x 33.9	6	22	<0.01	6.79	Large size, single band
Proposed Antenna	57 x 35	6.13 9.08 11.41	26 33 22	< 0.1[5] < 0.02[6] <0.0011	4.44 6.65 7.38	Compact size, triple-band, high isolation, high gain

5.5 Chapter Summary

This chapter describes the design of a two-port MIMO patch antenna for multi-band communications that uses the ISMeTM superstrate. A superstrate that is etched over the two-port MIMO-ANT at an optimal height of 7 mm has a 3 x 5 array unit cell of the ISMeTM. The CST studio suite is used to simulate the proposed antenna. At frequencies of 6.31 GHz, 9.09 GHz, and 11.41 GHz, three resonances

were achieved. The proposed antenna and the two-port MIMO patch antenna were compared using a variety of parameters, including diversity gain, envelope correlation coefficient, and height (ag). Over the three-frequency band, a mutual coupling reduction of 26 dB, 33 dB, and 22 dB was attained. The proposed antenna is suitable for use in multiband MIMO communications.

Chapter 6

Conclusion and Future Scope

6.1 Conclusion

This thesis presents the design and analysis of a metamaterial-based microstrip patch antenna for wireless application. For multi-band wireless communication, a novel I-shaped metamaterial structure utilizing a split ring resonator is proposed, developed, and examined. The three-square split-ring resonators (SSRRs) and I-shaped copper strip at the middle are used in the design of the proposed ISMeTM unit cell structure. Using the FR-4 dielectric substrate material, the proposed ISMeTM has a dimension of 10 x 10 x1.6 mm^3. To achieve the best possible results for multi-band operation, different array configurations are analysed together with variations in ring gaps, strip lengths, and strip width. The unit cell's effective permittivity, permeability, and refractive index have all been investigated. The ISMeTM structure that has been presented exhibits resonance frequencies at seven operating bands, 6.31, 7.79, 9.98, 10.82, 11.86, 13.36, and 15.5 GHz. The proposed novel ISMeTM possesses multi-band properties that make it suitable for use in medical equipment, remote aerospace applications, electromagnetic cloaking, and other applications.

The design of a wireless communication microstrip antenna with Square Split Ring Resonators (SSRR) as inspired is also explored in this thesis. With dimensions of 25 x 21.4 x 1.6 mm^3 and a frequency of 5.85 GHz, the SSRR is mounted on a rectangular patch antenna. The antenna gain is enhanced by a unique SSRR design. The proposed antenna operates in a single operational band and has a gain of 5.278 dBi with a bandwidth of 430 MHz. This work was furthered by making use of the rectangular microstrip patch antenna performance-improving I-shaped metamaterial (ISMeTM) superstrate. The rectangular patch antenna, which is fed by a 50Ω coaxial connector, was covered with the 7 × 7 array of the unit cells as the superstrate. The proposed antenna achieves gains of 4.19 dBi, 2.4 dBi, and 5.68 dBi at three operational frequencies of 6.18 GHz, 9.65 GHz, and 11.45 GHz. The Agilent 8719ET network analyzer is used to conduct measurements on the proposed antenna, which is fabricated on a low-cost FR-4 substrate. It has an overall dimension of 70 x 70 x 1.6 mm^3 . The obtained results

demonstrate the high gain, improved bandwidth, and excellent radiation efficiency of the proposed antenna.

Additionally, a 3 x 5 array unit cell of the ISMeTM is placed on top of a two-port MIMO patch antenna as a superstrate. The proposed antenna successfully operated at three frequencies: 6.31 GHz, 9.08 GHz, and 11.41 GHz. Over the range of the three operational frequency bands, a combined gain of 4.44 dBi, 6.64 dBi, and 7.38 dBi was attained. There was a 26 dB, 33 dB, and 22 dB reduction in the mutual coupling of the two-port MIMO patch antenna, respectively.

In conclusion, the design and analysis of a novel I-shaped multiband metamaterial, metamaterial-based antenna, I-shaped metamaterial array-based multiband microstrip patch antenna with enhanced gain and I-shaped metamaterial based multiband MIMO antenna have been presented. The proposed I-shaped metamaterial structure utilizing a split ring resonator exhibits resonance frequencies at multiple operating bands, making it suitable for various applications such as medical equipment, remote aerospace applications, electromagnetic cloaking etc. The use of Square Split Ring Resonators (SSRR) is explored, and a unique SSRR design is shown to enhance the gain of microstrip antenna. The proposed antenna with an ISMeTM superstrate achieves high gain, improved bandwidth, and excellent radiation efficiency at three operational frequencies. Moreover, a 3 x 5 array unit cell of the ISMeTM is used as a superstrate on a two-port MIMO patch antenna to attain the gain enhancement and mutual coupling reduction. The presented MIMO antenna is suitable for multiband wireless systems.

6.2 Future Scope

For further works, the miniaturization and compactness of the microstrip patch antenna should be considered when utilizing the proposed metamaterial structure for gain and bandwidth enhancement. Other techniques such as loading the defected ground plane, modifying the substrate, and loading the metamaterial near or on the radiating patch should be considered for improving the performance of the antenna.

References

[1] A. Gokhale, Introduction to telecommunications, 2nd ed., Cengage Learning, 2004.

[2] J. Volakis, R. C. Johnson, and H. Jasik, Antenna engineering Handbook; Fourth Edition. McGraw-Hill's Access Engineering, McGraw-Hill Education, 2007.

[3] J. C. Maxwell, A Treatise on Electricity and Magnetism, Oxford University Press, London, UK, 1873.

[4] D. G. Fang, Antenna Theory and Microstrip Antennas, CRC Press, 2017

[5] C. A. Balanis, "Antenna Theory: A Review," Proc. IEEE, vol. 80, no. 1, pp. 7-23, 1992.

[6] L.V. Blake, "Antennas," Wiley, New York, pp. 289, 1966.

[7] J. D. Kraus, "Antennas," McGraw-Hill, New York, 1988.

[8] M. S. Smith "Introduction to antennas," Palgrave, London pp. 17-32, 1988.

[9] A. R. Harish and M. Sachidananda, "Antennas and Wave Propagation," Oxford university press, 2007.

[10] M. Puneeth and S. J. S. Rajesh, "Design of different types of aperture antennas using HFSS," *International Journal of Advanced Engineering Management and Science (IJAEMS)*, vol. 1, Iss. 2, pp. 39-47, 2015.

[11] C. A. Balanis, Antenna Theory Analysis and Design. Hoboken, New Jersey: John Wiley & Sons, Inc., 4th ed., 2016.

[12] J. Q. Howell, microstrip antenna. IEEE transactions on antennas and propagation, vol. AP-23, pp. 90-93, 1975.

[13] D. M. Pozar, Microwave engineering, 2nd ed. New York (NY): John Wiley & Sons. Inc, 1998.

[14] N. Kaur and S. Malhorta, "A review on significance of design parameters of microstrip patch antennas. In 2016 5th International Conference on Wireless Networks and Embedded Systems (WECON) IEEE, pp. 1-6.

[15] R. Mishra, "An overview of microstrip antenna," *HCTL Open International Journal of Technology Innovations and Research (IJTIR),* vol. 21, Iss. 2, pp. 39-55, 2016.

[16] M. A. Islam and N. C. Karmakar, "A 4 x 4 dual polarized mm- wave ACMPA array for universal mm- wave chipless RFID tag reader," *IEEE. Trans. Ant. Propag*., vol 63, no. 4, pp. 1633-1640, 2015.

[17] H. Errifi, A. Baghdad, A. Badri, and A. Sahel, "Radiation characteristics enhancement of microstrip triangular patch antenna using several array structures," *International Journal of Wireless and Microwave Technologies (IJWMT),* vol. 5, no.3, pp. 1-17, 2015.

[18] M. Asaadi and A. Sebak, "Gain and bandwidth enhancement of 2 x 2 square dense dielectric patch antenna array using a holey superstrate," *IEEE Antennas and Wireless Propagation Letters,* no. 16, pp. 1808- 1811, 2017.

[19] L. C. Paul, M. S. Hosain, S. Sarker, M. H. Morshed, and A. K. Sarkar, "The effect of changing substrate material and thickness on the performance of inset feed microstrip patch antenna," *American Journal of Networks and Communications*, vol 4, no. 3, pp. 54-58, 2015.

[20] J. M. Kovit and Y. R. Samii, "Using thick substrate and capacitive probe compensation to enhance the bandwidth of traditional CP patch antennas," *IEEE Trans. Ant. Propg.,* vol 62, no. 10, pp. 4970-4979, 2014.

[21] M. U. Khan, M. S. Sharawi, and R. Mittra, "Microstrip patch antenna miniaturization techniques: a review," *IET Microw. Ant. Propg.*, vol. 9, no. 9, pp. 913-922, 2015.

[22] T. Ali, B. K. Subhash, S. Pathan, and R. C. Biradar, "A compact decogonal-shaped UWB monopole planar antenna with truncated ground plane," *Microw. Opt. Technol. Lett*., vol. 60, no.12, pp. 2937–2944, 2018.

[23] R. A. Shelby, D. R. Smith, and S. Schultz, "Experimental verification of a negative index of refraction," Science, vol. 292, no. 5514, pp. 77–79, 2001.

[24] R. Marques, F. martin, and M. Sorolla, "Metamaterials with negative parameters: theory, design, and microwave applications," Wiley & Sons, 2011.

[25] V. G. Veselago, "The electrodynamics of substances with simultaneously negative values of ε and μ", Sov. Phy. Usp. 1968, 10, 509–514.

[26] P. Khushnuma, "Metamaterials: Types, applications, development, and future scope," *International Journal of Advance Research, Ideas, and Innovations in Technology*, vol. 4, Iss. 3, pp. 2325-2327, 2018.

[27] K. Gangwar and R. P.S. Gangwar, "Metamaterials: characteristics, process and applications," *Advance in Electronics and Electric Engineering*, vol, 4, no. 1, pp.97-106, 2014.

[28] Y. Rahmat-Samii and A. C. Densmore, "Technology trends and challenges of antennas for satellite communication systems," *IEEE Trans. Ant. Propg*., vol. 63, no. 4, pp. 1191-1204, 2014.

[29] R. James, P. S. Hall, and C. Wood, "Microstrip antenna theory and design", vol. 12, 1986.

[30] M. S. Smith "Introduction to antennas," Palgrave, London pp. 17-32, 1988.

[31] K. P. Vinay, B. A. Sheik, and A. T. Rao, "Design and analysis of slot antenna parameters using HFSS," International journal of innovative technology and exploring engineering *(IJITEE*), vol. 3, 1955.

[32] M. Puneeth and S. J. S. Rajesh, "Design of different types of aperture antennas using HFSS," *International Journal of Advanced Engineering Management and Science (IJAEMS)*, vol. 1, Iss. 2, pp. 39-47, 2015.

[33] R. E. Collin and F. J. Zucker, *Antenna Theory*, parts 1 and 2, McGraw-Hill, New York, 1969.

[34] M. A. Jamshed, F. Heliot, and T. W. Brown, "A survey on electromagnetic risk assessment and evaluation mechanism for future wireless communication systems," *IEEE Journal of electromagnetic, RF and microwaves in medicine and biology*, vol. 4, no. 1, pp. 24-36, 2019.

[35] A. Pandey, Practical Microstrip and Printed Antenna Design. Artech House, 2019.

[36] A. C. MacPherson and D. M. Kerns, "A new technique for the measurement of microwave standing wave ratios," *Proceedings of the IRE*, vol. 44, no. 8, pp. 1024-1030, 1956.

[37] X. L. Bao and M. J. Ammann, "Comparison of several novel annual ring microstrip patch for circular polarization," *Journal of electromagnetic waves and applications*, vol. 20, no. 11, pp. 1427-1438, 2006.

[38] V. L. Subrahmanya, "Pattern analysis of the rectangular microstrip patch antenna," *University college of Boras*, 2009.

[39] R. E. Munson, "Single slot cavity antennas assembly", U.S. patent No. 3713162, January 1975, pp. 90-93.

[40] R. E. Munson, "Conformal microstrip antennas and microstrip phased arrays," *IEEE Trans. Antennas propagation*, vol. AP-22, PP. 74-78, 1974.

[41] M. H. Prio, M. M. U. Rashid, L. C. Paul, and A. K. Sarkar, "total efficiency comparison of different shaped microstrip patch antennas having defected ground structure," *In 2015 International conference on electrical & electronics engineering (ICEEE),* pp. 265-268.

[42] K. Jain and K. Gupta, "Different substrate use in microstrip patch antenna- a survey," *Int. J. Sci. Res.,* vol. 3, Iss. 5, pp.1802-1803, 2014.

[43] I. Khan, D. Geetha, R. Gunjal "Review of MSP antenna design for various substrates," 2018 (https://papers.ssrn.com/sol3/papers.cfm?abstract_id=3230632).

[44] R. Mishra, R. G. Mishra, R. K. Chaurasia, and A. K. Shrivastava, "Design and analysis of microstrip patch antenna for wireless communication," *Int. J. Inno. Tech. Explo. Eng*., vol. 8, no, 7, pp. 663-666, 2019.

[45] B. Mishra, R. K. Vernma, N. Yashwanth, and R. K. Singh, "A review on microstrip patch antenna parameters of different geometry and bandwidth enhancement techniques," *Int. J. Micro. Wirel. Tech.,* vol 14, no. 5, pp. 652-673, 2022.

[46] M. K. Rahim, Z.W. Low, P. J. Soh, A. Asrokin, M. H. Jamaluddin, and T. Masri, "Aperture coupled microstrip antenna with different feed sizes and aperture positions," In 2006 International RF and Microwave Conference, pp. 31-35, September,12, 2006.

[47] T. Yasin and R. Baktur, "Bandwidth enhancement of meshed patch antennas through proximity coupling," vol. 16, pp. 2501-2504, 2017.

[48] A. Bansal and R. Gupta, "A review on microstrip patch antenna and feeding techniques," *Int. J. Info. Tech*., vol. 12, no, 1, pp. 149-154, 2020.

[49] M. Simruni and S. Jam, "Radiation performance improvement of wideband microstrip antenna array using wideband AMC structure," *International Journal of Communication Systems*, vol. 32, no. 11, pp. e3962, 2019.

[50] M. A. Islam and N. C. Karmkar," An 8 x 8 mm- wane LP ACMPA array for long range mm-wave chipless RFID tag sensor reader," *IEEE Journal of radio frequency identification*, vol. 5, no. 1, pp. 53-63, 2020.

[51] M. Nikfalazar, C. Kolerr, A. Wiens, A. Mehmood, M. Sohrabi, H. Maune, J. R. Binder and R. Jakoby, "Beam steering phased array antenna with fully printed phased shifters based on low-temperature sintered BST- composite thick films," *IEEE Microwave and Wireless Components Letters,* Vol. 26, no. 1, pp. 70-72, 2015.

[52] K. L. Wong, C. L. Tang, and H. T. Chen, "A compact meandered circular microstrip antenna with a shorting pin," Microwave and Optical Technology Letters, vol. 15, no. 3, pp. 147- 149, 1997.

[53] C. Sun, H. Zheng, L. Zhang, and Y. Liu, "Analysis and design of a novel coupled shorting strip for compact patch antenna with bandwidth enhancement," *IEEE Antennas and Wireless Propagation Letters*, no. 13, 1477- 1481, 2014.

[54] X. Zhang and L. Zhu, "High gain circularly polarized microstrip patch antenna with loading of shorting pins," *IEEE Trans. Ant. Propg.* Vol. 64, no. 6, pp. 2172-2178, 2016.

[55] T. K. Lo, E. K. W. Hwang, and B. Lee, "Miniature aperture coupled microstrip antenna of very high permittivity," *Electronics Letters*, vol. 33, no. 1, pp. 9-10, 1997.

[56] X. Tang, H. wong, Y. Long, Q. Xue, and K. L. Lau, "Circularly polarized shorted patch antenna on high permittivity substrate with wideband," *IEEE Trans. Ant. Propg*., vol. 60, no. 3, pp. 1588-1592, 2011.

[57] S. Noghanian and L. Shafai, "Control of microstrip antenna radiation characteristics by ground plane and shape," *IEE Proc. Microw. Ant. Propg.*, vol. 145, no. 3, pp. 207-212, 1998.

[58] M. U. Khan, M. S. Sharawi, and R. Mittra, "Microstrip patch antenna miniaturization techniques: a review," *IET Microw. Ant. Propg.*, vol. 9, no. 9, pp. 913-922, 2015.

[59] H. N. Awl, Y. I. Abdulkarim, L. Deng, M. Bakir, F. F. Muhammadsharif, M. Karaasian, E. Unal, and H. Luo, "Bandwidth improvement in bow-tie microstrip antennas: The effect of substrate type and design dimensions," Appl. Sci., vol 10, no. 2, pp. 504, 2020.

[60] M. Palandoken, "Artificial materials based microstrip antenna design," pp.43-50, 2011.

[61] R. pandeeswari and S. Raghavan, "Microstrip antenna with complementary split ring resonator loaded ground plane for gain enhancement," *Microwave and Optical Technology Letters*, vol. 57, no. 2, pp. 292-296, 2015.

[62] A. D. Tadesse, O. P. Acharya, and S. Sahu, "Application of metamaterials for performance enhancement of planar antennas: a review," *International Journal of RF and Microwave Computer- Aided engineering*, vol. 30, no. 5, pp. 22154, 2020.

[63] B. P. Smyth, S. Barth, and A. K. Iyer, "Dual-band microstrip patch antenna using integrated uniplanar metamaterial based EBGs," IEEE Trans. Ant. Propag., vol. 64, no. 12, pp. 5046-5053, 2016.

[64] Y. Alnaiemy and L. Nagy, “Further investigation of the feasibility of using EBG structure based microstrip antenna for gain enhancement,” In 2020 International conference on radar antenna, microwave, electronics, and telecommunications (ICRAMET), 18 November 2020, pp.102-106, IEEE.

[65] W. E. McKinzie, D. M. Nair, B. A. Thrasher, M. A. Smith, E. D. Hughes, and J. M. Parisi, “60-GHz 2 x 2 LTCC patch antenna array with an integrated EBG structure for gain enhancement,” *IEEE Ant. Wirel. Propag. Lett*., vol. 15, pp. 1522-1525, 2016.

[66] E. Thakur, N. Jagian, S. D. Gupta, and B. K. Kanaujia, “Advances in patch antenna design using EBG structures,” *Inprinted Antennas*, CRC Press, pp. 363-400, 2020.

[67] S. X. Ta, T. H.Y. Nguyen, K. K. Nguyen, and C. Dao-Ngoc, “Bandwidth enhancement of circularly polarized fabry-perot antenna using single layer partially reflective surface.” *International journal of RF and microwave computer aided engineering,* vol. 29, no. 8, pp. e21774, 2019.

[68] E. Zhou, Y. Chen, F. Chen, and H. Luo, “Wideband and high gain patch antenna with reflective focusing metasurface.” *AEU- Int. J. Elect. Comm*., vol. 134, pp. 153709, 2021.

[69] S. X. Ta and T. K. Nguyen, “AR bandwidth and gain enhancement of patch antenna using a single dielectric superstrate.” *Elect. Lett*., vol. 53, no. 15, pp.1015-1017, 2017.

[70] N. Bahari, M. F. Jamlos, and M. M. Isa, “Gain enhancement of microstrip patch antenna using artificial magnetic conductor.” *Bull. Elect. Eng. Info.,* vol.8, no. 1, pp. 1667-171, 2019.

[71] K. Belabbas, K. Khedroche, and A. Hocini, “Artificial magnetic conductor-based millimeter-wave microstrip patch antenna for gain enhancement. *Journal of telecommunications and information technology*, vol. 1. pp. 56-63, 2021.

[72] K. Jairath, N. Singh, M. Shabaz, V. Jagota, and B. K. Singh, “Performance analysis of metamaterial inspired structure loaded antennas for narrow range wireless communication,” *Scientific programming*, pp. 1-17, 2022.

[73] L. I. Mandel’shtam, “Group velocity in crystal lattice”. Zh. Eksp. Teor. Fiz. 1945, 15, 475–478.

[74] J. B. Pendry, A. J. Holden, W. J. Stewart, and I. Youngs, “Extremely low frequency plasmons in metallic meostructure,” *Phys. Rev. Lett.,* vol. 76, no. 25, pp. 4773, 1996.

[75] J. B. Pendry, A. J. Holden, D. J. Robbins, and W. J. Stewart, “Magnetism from conductors and enhanced nonlinear phenomena,” *IEEE Trans. Microw. Theory. Tech.*, vol. 47, no. 11, pp. 2075–2084, 1999.

[76] D. R. Smith, W. J. Willie, D. C. Vier, S. C. Nemat-Nasser, and S. Schultz, “Composite medium with simultaneously negative permeability and permittivity,” *Phy. Rev. Lett.,* vol. 84, no. 18, pp. 4184, 2000.

[77] A. K. Iyer and G. V. Eleftheriades, “Negative refractive index metamaterials supporting 2-D waves,” IEEE MTT-S Int. Microw. Symp. Digest. Vol. 2, pp. 1067–1070,2002.

[78] C. Caloz and T. Itoh, "Transmission line approach of left-handed (LH) material and microstrip implementation of an artificial LH transmission line," *IEEE Trans. Antennas Propag.,* vol. 51, pp. 1159–1166, 2004.

[79] P. B. Dash, B. Naik, J. Nayak, and S. Vimal, "Deep belief network-based probabilistic generative model for detection robotic manipulator failure execution," *Soft Computing*, pp. 1-13, 2021.

[80] H. Benosman and N. B. Hacene, "Design and Simulation of Double "S" Shaped Metamaterial," *Int. J. Compt. Sci. Iss.* vol. 9, no. 2, pp. 1694–1814, 2012.

[81] M. Aznabet, O. El Mrabet, J. M. Floc'h, F. Falcone, and M. A. Drissi, "A coplanar waveguide-fed printed antenna with complementary split ring resonator for wireless communication systems," *Waves. Rand. Comp. Media.*, vol. 25, no. 1, pp. 43–51, 2015.

[82] A. Mallik, S. Kundu, and M. O. Goni, "Design of a novel two-rectangular U-shaped negative metamaterial," In Proc. International Conference on Informatics, Electronics and Vision (ICIEV) IEEE, Dhaka, Bangladesh*,* 17 May 2013, pp. 1-6.

[83] M. J. Alam, E. Ahamed, M. R. I. Faruque, J. Hossain, and M. T. Islam, "Aztec shape metamaterial-based bandpass filter for C, X and Ku-band applications," *IOP Conf. Ser. Ear. Enviro. Sci*., vol. *228*, no, 1, pp. 12019, 2019.

[84] E. Ekmekci and G. T. Sayan, "Investigation of effective permittivity and permeability for a novel V-shaped metamaterial using S-parameters," In Proc.5th International Conference on Electrical and Electronics Engineering, Bursa, Turkey, 5–9 December 2007.

[85] P. Jain, A. Thourwal, N. Sardana, S. Kumar, N. Gupta, and A. K. Singh, "I-shaped metamaterial antenna for X-band applications," In Proc. Progress in Electromagnetics Research Symposium-Spring (PIERS), Petersburg, Russia, 22 May 2017, IEEE, 2017, pp. 2800-2803.

[86] A. Dhouibi, S. N. Burokur, A. Lustrac, "Priou, A Study and analysis of an electric Z-shaped meta-atom," *Advan. Electromag.* vol. 1, no. 2 pp. 64–70, 2012.

[87] A. M. Tamim, M. R. I. Faruque, M. J. Alam, S. S. Islam, and M. T. Islam, "Split ring resonator loaded horizontally inverse double L-shaped metamaterial for C-, X- and Ku-Band Microwave applications," *Res. Phys*. vol. 12, pp. 2112–2122, 2019.

[88] M. J. Hossain, A. M. I. Faruque, M. T. Islam, and S. S. Islam, "An effective medium ratio obeying meta-atom for multiband applications," *Bull. Pol. Acad. Sci. Tech. Sci.* vol. 65, no. 2, pp. 2112–2122, 2019.

[89] S. S. Islam, M. R. I. Faruque, and M. T. Islam, "The design and analysis of a novel H-shaped metamaterial for multi-band microwave applications." *Materials*, vol. *7*, no. 7, pp. 4994–5011, 2014.

[90] A. M. Siddiky, M. R. I. Faruque, M. T. Islam, S. Abdullah, and M. U. Khandaker, "Inverse double-C shaped square split ring resonator-based metamaterial with multi-resonant frequencies for satellite band applications," *Res. Phys*. vol. 19, pp. 103454, 2020.

[91] A. Ishrimaru, S. Jaruwatanadilok, and Y. Kuga, “Generalized surface plasom resonance sensors using metamaterials and negative index materials,” *The Electronmagnetics Academy*, vol. 51, no. pp. 139-152, 2005.

[92] V. Van Yem and N. N. Lan, “Gain and bandwidth enhancement of array antenna using novel metamaterial structure,” J. Comm., vol. 13, no.3, pp. 101-107, 2018.

[93] B. Tutuncu, H. Torpi, and B. Urul, “A comparative study of different types of metamaterials for enhancement of microstrip patch antenna directivity at the Ku-band (12 GHz),” *Turkish Journal of Electrical Engineering and Computer sciences*, vol. 26, no. 3, pp. 1171-1179, 2018.

[94] J. D. Baena. J. Bonache F. Martin, R. M. Sillero, F. Falcone, T. Lopetegi, M. A. Laso, J. Garcia-Garcia, M. F. Portillo, and M. Sorolla, “Equivalent- circuit models for split-ring resonators and complementary split-ring resonators coupled to planar transmission lines,” *IEEE Trans. Microw. Theo. Techn*q., Vol. 53, no. 4, pp. 1451- 1461, 2005.

[95] S. RoyChoudhuy, V. Rawat, A. H. Jalal, S. N. Kale, and S. Bhansali, “Recent advances ion metamaterial split-ring-resonator circuits as bio sensors and therapeutic agents,” Biosensors and Bioelectronics, vol. 86, pp. 595-608, 2016.

[96] D. R. Smith, S. Schultz, P. Markos, and C. M. Soukoulis, “Determination of effective permittivity and permeability of metamaterial from reflection and transmission coefficients,” *physical review B*, vol. 65, no. 19, 2002.

[97] I. A. Buriak, V. O. Zhurba, G. S. Vorobjov, V. R. Kulizhko, O. K. Kononov, and O. Rybalko, “Metamaterials: Theory, classification and application strategies,” *Journal of Nano- and electronic Physics*, vol. 8, no, 4(2), pp. 4088-11, 2016.

[98] C. M. Krowne, “Left-handed material use in monoatomic & III-V ICs” *III-Vs Review,* vol. 17, no. 3, pp. 26-27, 2004.

[99] H. Chen, B. I. Wu, and J. A. Kong, “Review of electromagnetic theory in left-handed materials,” Journal of electromagnetic waves and applications, vol. 20, no. 15, pp. 2137-2151, 2006.

[100] T. J. Cui, D. Smith, and R. Liu, “Metamaterials,” springer, pp. 1-19, 2010.

[101] W. J. Krzystofik and T. N. Cao, “Metamaterials in application to improve antenna parameters,” Metamaterials and Metasurface, vol. 12, no, 2, pp. 63-85, 2018.

[102] R. Kumar, M. Kumar, J. S. Chohan, and S. Kumar, “Overview on metamaterial: History, types and applications,” *Materials Todays: Proceedings*, vol. 56, pp. 3016-3024, 2022.

[103] G. Lipworth, A. Rose, O. Yurduseven, V. R. Gowda, M. F. Imani, H. Odabasi, P. Trofatter, J. Gollub, and D. R. Smith, “Comprehensive simulation platform for a metamaterial imaging system,” *Applied Optics*, vol. 54, no. 32, pp. 9343-9353, 2015.

[104] M. Alibakshikenari, B. S. Virdee, P. Shukla, N. O. Parchin, L. Azpilicueta, C. H. See, R. A. Abd-Alhameed, F. Falcone, I. Huynen, T. A. Denidni, and E. Limiti, “Metamaterial- inspired antenna array for application in microwave breast imaging systems for tumor detection,” *IEEE Access*, vol. 8, pp. 174667-174678, 2020.

[105] W. J. Padilla and R. D. Averitt, “Imaging with metamaterials,” *Nature Reviews Physics*, vol. 4, no. 2, pp. 85-100, 2022.

[106] P. Yu, L. V. Besteiro, Y. Huang, J. Wu, L. Fu, H. H. Tan, C. Jagadish, G. P. Wiederrecht, A. O. Govorov, and Z. Wang, “Broadabnd metamaterial absorbers,” *Advanced Optical Materials*, vol 7, no. 3, pp. 1800995, 2019.

[107] M. Amiri, F. Tofigh, N. Shariati, J. Lipman, and M. Abolhasan, “Review on metamaterial perfect absorbers and their applications to IoT,” *IEEE internet of Things Journal*, vol. 8, no. 6, pp. 4105-41031, 2020

[108] L. Feng, P. Huo, Y. Liang, and T. Xu, “Photonic metamaterial absorbers: morphology engineering and interdisciplinary applications,” *Advance Materials*, vol. 32, no. 27, pp. 1903787, 2020.

[109] B. X. Wang, X. Zhai, G. Z. Wang, W. Q. Huang, and L. L. Wang, “A novel dual-band terahertz metamaterial absorber for a sensor application,” *Journal of Applied Physics*, vol. 117, no. 1, pp. 014504, 2015.

[110] Y.I. Abdulkarim, L. Deng, H. Luo, S. Huang, M. Karaaslan, O. Altıntaş, M. Bakır, F. F. Muhammadsharif, H. N. Awl, C. Sabah, and K. S. Al-badri, “Design and study of a metamaterial-based sensor for the application of liquid chemicals detection,” *Journal of Materials Research and Technology*, vol. 9, no. 5, pp.10291-10304, 2020.

[111] S. K. Sahu, S. Sahu, C. S. Mishra, and G. Palai, “Analysis of reflected frequency band of metamaterial grating at THz frequency: a future application of filter,” *Optik,* vol. 127 no. 10, pp.4547-4550, 2016.

[112] P. Pitchappa, A. Kumar, R. Singh, and N. Wang, “Electromechanically Tunable Frequency-agile Metamaterial Bandpass Filters for Terahertz Waves,” *Advanced Optical Materials*, vol. 10 no. 2, pp. 2101544, 2022.

[113] C. Huang, J. Zhang, Q. Cheng, and T. Cui, "Multi-band tunable asymmetric transmission of linearly polarized electromagnetic waves achieved by active chiral metamaterial. In Proceedings of the 2019 Photonics & Electromagnetics Research Symposium-Fall (PIERS-Fall), Xiamen, China, 17–20 December 2019.

[114] M. Wang, Z. Yang, J. Wu, J. Bao, J. Lui, L. Cai, T. Dang, H. Zheng, and E. Li, “Investigation of SAR reduction using flexible antenna with metamaterial structure in wireless body area network,” *IEEE Trans Antenna Propag*., vol. 66, no. 6. pp. 3076–3086, 2018.

[115] S. S. Islam, M. M. Hasan, and M. R. Faruque, “A new metamaterial-based wideband rectangular invisibility cloak,” *Applied Physics A*. Vol. 124, no. 2, pp. 1-6, 2018.

[116] A. Alex-Amor, A. Palomares-Caballero, and C. Molero, “3-D metamaterials: Trends on applied designs, computational methods and fabrication techniques,” *Electronics,* vol. 11, no. 3, 410, 2022.

[117] B. B. Zheng, R. C. Zhong, X. Chen, M. H. Fu, and L.L. Hu. "A novel metamaterial with tension-torsion coupling effect," *Materials & Design*, vol. 171, pp. 107700, 2019.

[118] P. S. Manage, U. Naik, S. Nargundkar, and V. Rayar, "A survey on applications of metamaterials in antenna design, In 2020 3rd International Conference of Smart Systems and Inventive Technology (ICSSIT), pp. 153-158, IEEE.

[119] K. Gangwar and R. P.S. Gangwar, "Metamaterials: characteristics, process and applications," *Advance in Electronics and Electric Engineering*, vol, 4, no. 1, pp.97-106, 2014.

[120] N. Michishita, "Expectation for metamaterials for antenna applications," In International Symposium on Antenna and Propagation (ISAP), 24 October 2016, pp. 558-559, IEEE

[121] G. Geetharamani and T. Aathmanesan "A metamaterial inspired tapered patch antenna for WLAN/WiMAX applications," *Wireless Personal Communications*, vol.113, no. 2, pp.1331-43, 2020.

[122] N. Agrawal, "Enhanced Performance of Microstrip Antenna with Meta-material: A Review," *Advances in Communication, Devices and Networking*, pp. 221-31, 2022.

[123] V. P. Sarin and K. Vasudevan, "Metamaterials for antenna applications," In Handbook of Metamaterial-Derived Frequency Selective Surfaces, Springer Nature Singapore, vol. 3. pp. 1-47, 2022.

[124] S. S. Al-Bawri, M. T. Islam, T. Shabbir, G. Muhammad, M. S. Islam, and H. Y. Wong, "Hexagonal shaped near zero index (NZI) metamaterial-based MIMO antenna for millimeter-wave application," IEEE Access, vol. 8, pp. 181003-181013, 2020.

[125] P. Kumar, T. Ali, and M. M. Pai, "Electromagnetic metamaterials: A new paradigm of antenna design," *IEEE Access*, vol. 22, no. 9, pp. 18722-18751, 2021.

[126] A. A. Althuwayb, "Enhanced radiation gain and efficiency of a metamaterial-inspired wideband microstrip antenna using substrate integrated waveguide technology for sub-6 GHz wireless communication systems," *Microwave and Optical Technology Letters*, vol. 63, no. 7, pp. 1892-1898, 2021.

[127] J. Wang, Q. Liu, and L. Zhu, " Bandwidth enhancement of a differential-fed equilateral triangular patch antenna via loading of shorting posts," *IEEE Trans. Antennas Propag.*, vol. 65, no. 1, pp. 36-43, 2017.

[128] K. Da Xu, H. Xu, Y. Liu, J. Li, Q. H. Liu, "Microstrip patch antennas with multiple parasitic patches and shorting vias for bandwidth enhancement," *IEEE Access*, vol. 6, pp.11624-11633, 2018.

[129] P. Acharya, J. Kumar, V. Dahiya, and S. Peddakrishna, "Miniaturized omnidirectional satellite phone antenna inspired by meander line radiator and metamaterial integrated ground plane," *International Journal of Information Technology,* vol. 6, pp. 2981-2990, 2022.

[130] B. Yuan, Y. H. Zheng, X. H. Zhang, B. You, and G. Q. Luo, "A bandwidth and gain enhancement for microstrip antenna based on metamaterial," *Microwave and Optical Technology Letters*, vol. 59, no. 12, pp. 3088-3093, 2017.

[131] S. Roy and U. Chakraborty, "Metamaterial-embedded dual wideband microstrip antenna for 2.4 GHz WLAN and 8.2 GHz ITU band applications," *Waves in Random and Complex Media*, vol. 30, no. 2, pp. 193-207, 2020.

[132] R. Pandeeswari and S. Raghavan, "Broadband monopole antenna with split ring resonator loaded substrate for good impedance matching," *Microwave and Optical Technology Letters,* vol. 56, no. 10, pp. 2388-2392, 2014.

[133] M. H. Ullah and M. T. Islam, "A new metasurface reflective structure for simultaneous enhancement of antenna bandwidth and gain," *Smart materials and Structures*, vol. 23, no. 8, pp. 085015, 2014.

[134] W. Cao, W. Ma, W. Peng, and Z. N. Chen, ''Bandwidth-enhanced electrically large microstrip antenna loaded with SRR structures,'' IEEE Antennas Wireless Propag. Lett., vol. 14, no. 1, pp. 169-175, 2020.

[135] H. Al Issa, Y. Khraisat, and F. Alghazo, "Bandwidth enhancement of microstrip patch antenna by using metamaterial," International Journal of Interactive mobile Technology (iJIM), vol. 3, no. 3, pp.

[136] A. K. Panda and A. Sahu, "An investigation of gain enhancement of microstrip antenna by using inhomogeneous triangular metamaterial," In 2011 International Conference on Computational Intelligence and Communication Networks 7 October, pp. 154-157, IEEE.

[137] K. K. Naik, "Asymmetric CPW-fed SRR patch antenna for WLAN/WiMAX applications," *AEU-International Journal of Electronics and Communications*, vol. 93, pp. 103-118, 2018.

[138] M. J. Jeong, N. Hussain, J. W. Park, S. G. Park, S. Y. Rhee, and N. Kim, "Millimeter-wave microstrip patch antenna using vertically coupled split ring metaplate for gain enhancement," *Microwave and Optical Technology Letters*, vol. 61, no.10, 2360-5, 2019.

[139] H. R. Vani and M. A. Goutham, "Gain Enhancement of Microstrip Patch Antenna Using Metamaterial Superstrate," *The Applied Computational Electromagnetics Society Journal (ACES*), vol. 34, Iss. 8, pp. 1250-3, 2019.

[140] A. S. BK and A. Pradeep, "Complementary Metamaterial Superstrate for Wide Band High Gain Antenna," In 2022 IEEE Wireless Antenna and Microwave Symposium (WAMS), June 5, pp. 1-5, IEEE.

[141] D. Chaturvedi and S. Raghavan, "SRR-loaded metamaterial-inspired electrically-small monopole antenna," *Progress In Electromagnetics Research C*, vol. 81, 11-19, 2018.

[142] H. Xiong, D. Li, C. Yang, X. M. Li, and X. Ou, "Miniaturization of monopole antenna by Metamaterial loading technique," IETE Journal of Research, vol. 62 no. 5, pp. 714-720, 2016.

[143] B. Thakur and A. Kunte, “Improved design of CELC meta1resonators for bandwidth improvement and miniaturization of patch antenna,” *Appl. Phys. A Mater. Sci. Process*, vol. 124, no. 12, pp. 1-8, 2018.

[144] H. L. Zhu, S. W. Cheung, and T. I Yuk, “Miniaturization of patch antenna using metasurface,” Microw. Opt. Technol. Lett., vol. 57, no. 9, pp. 2050-2056, 2015.

[145] D. Zarifi, M. Soleimani, and A. Abdolai, “Parameter retrieval of chiral metamaterials based on the state- space approach,” Physical Review E, vol. 88, no. 2, pp. 023204, 2013.

[146] E. J. Rothwell, J. L. Frasch, S. M. Ellison, P. Chahal, and R. O. Ouedraogo, “Analysis of the Nicolson-Ross-Weir method for characterizing the electromagnetic properties of engineered materials,” *Progress In Electromagnetics Research*, vol.157, pp. 31-47, 2016.

[147] O. Luukkonen, S. I. Maslovski, and S. A. Tretyakov, “A stepwise Nicolson-Ross-Wier-based material parameter extraction method,” IEEE Ant. Wirel. Propag. Lett., vol. 10, pp. 1295–1298, 2011.

[148] S. U. Afsar, M. R. I. Faruque, M. J. Hossain, M. U. Khandaker, H. Osman, and S. Alamri, “Modified Hexagonal split ring resonator based on epsilion-negative metamaterial for triple-band satellite communication,” Micromachines, vol. 12, pp. 878, 2021.

[149] O. Sydoruk, E. Tatartschuk, E. Shamonia, and L. Solymar, “Analytical formulation for the resonant frequency of split rings,” *J. Appl. Phys.*, vol. 5, no.1, pp. 014903, 2009.

[150] G. A. Rinard and G. R. Eaton, “*Biomedical EPR-Part B: Methodology, Instrumentation, and Dynamics*,” Springer Science & Business Media: New York, NY, USA, 2005, vol. 24, pp. 19–52.

[151] F. W. Grover, “*Inductance Calculations: Working Formulas and Tables*,” Courier Corporation, Instrument Society of America, Research Triangle Park: Pittsburgh, PA, USA, 2004.

[152] L. F. Shatz and C. W. Christensen, “Numerical inductance calculations based on its principles,” *PLoS ONE*, vol. 9, no 11, pp. e111643, 2014.

[153] X. Chen, T. M. Grzegorczyk, B. Pacheco, J. Wu, and J. A. Kong, “Robust method to retrieve the constitutive effective parameters of metamaterials,” *Phys. Rev. E*, vol. 70, no. 1, pp. 1–7, 2014.

[154] A. Mithari and U. Patil, “Efficiency and bandwidth improvement using metamaterial of microstrip patch antenna”, *International Research Journal of Engineering and Technology (IRJET),* vol. 3, no. 3, pp. 2696-2701, 2016.

[155] S. K. Patel and Y. Kosta, “Triband microstrip-based radiating structure design using split ring resonator and complementary split ring resonator”, *Microwave and optical technology letters*, vol. 55, no. 9, pp. 2219-2222, 2013.

[156] H. Boutayeb and T. A. Denidni, “Gain enhancement of a microstrip patch antenna using cylindrical electromagnetic crystal substrate,” IEEE Trans. Ant. Propag., vol. 55, no. 11, pp. 3140-3145, 2007.

[157] Z. B. Weng, Y. C. Jiao, F.S. Zhang, Y. Song, and G. Zhao, "A multi-band patch antenna on metamaterial substrate," *J. Electromagn. App*., vol. 22, no. 2-3, pp. 445–452, 2008.

[158] T. Alam, M. Samsuzzaman, M. R. I. Faruque, and M. T. Islam, "A metamaterial unit cell inspired antenna for mobile wireless applications," *Microw. Opt. Tech.Lett.,* vol. 58, no. 2. pp. 263-267, 2016.

[159] R. Rajkumar and K. Usha Kiran, "A metamaterial inspired compact open split ring resonator antenna for multiband operation," *Wirel. Per. Comm.,* vol. *97*, no. 1. pp. 951-965, 2017.

[160] M. Saravanan and S. M. Umarani, "Gain enhancement of patch antenna integrated with metamaterial inspired superstrate," *J. of Elect. Syst. and Info Tech.,* vol. 5, no. 3. pp.263-270, 2018.

[161] M. M. Hasan, M. Rahman, M.R. I. Faruque, M. T. Islam, and M. U. Khandaker, "Electrically compact SRR-loaded metamaterial inspired quad band antenna for bluetooth/WiFi/WLAN/WiMAX system." *Electronics*, vol. 8, no. 7, pp. 790, 2019.

[162] A. Pandya, T. K. Upadhyaya, and K. Pandya, "Design of metamaterial based multilayer antenna for navigation/WiFi/satellite applications," *Progress In Electromagnetics Research M 99*, pp. 103-113, 2021.

[163] U. Patel, T. Upadhyaya, A. Desai, R. Pandey, and K. Pandya, "Dual-band compact split-ring resonator-shaped fractal antenna with defected ground plane for sub-6-GHz 5G and global system for mobile communication applications," *International Journal of Communication Systems,* vol. 35, pp. e5105, 2022.

[164] B. D. Ajewole, P. Kumar, T. J. Afullo, "Square SRR Metamaterial inspired Microstrip Antenna for Wireless Mobile Communication," In International Conference on Artificial Intelligence, Big Data, Computing and Data Communication Systems (icABCD) Durban South Africa, 5 August 2021, IEEE, pp. 1-6.

[165] T. Rao, R. Pandey, and A. Kandu, "Design a wideband aperture coupled stacked microstrip antenna at 28 GHz for 5G applications," *Int. J. Sci. Prog. and Res.,* vol. 74, no. 1, pp. 61-65, 2020.

[166] S. L. Tripathi, S. R. Patre, S. Singh, and S. P. Singh, "Triple-band microstrip patch antenna with improved gain," In 2016 International Conference on Emerging Trends in Electrical Electronics & Sustainable Energy Systems (ICETEESES) 11 March 2016, IEEE, pp. 106-110.

[167] J. Kaur, Nitika, R. Panwa, "Design and optimization of a dual-band slotted microstrip patch antenna using differential evolution algorithm with improved cross polarization characteristics for wireless applications," *J. of Electromag. Waves and App.,* vol. 33, no. 11, pp. 1427-1442, 2019.

[168] S. Kucukcan, and A. Kaya, "Dual band microstrip patch antenna design for Wi-Fi applications,"*Europ . J. of Science and Tech.,* vol. 34, pp. 661-665, 2022.

[169] L. Lu, G. Y. Li, A. L. Swindlehurst, A. Ashikhmin, and R. Zhang, "An overview of massive MIMO: Benefts and challenges," *IEEE Journal of Selected Topic in Signal Processing*, vol. 8, no. 5, pp. 742–758, 2014.

[170] H. Yu, G. Yang, F. Meng, and Y. Li, "Performance analysis of MIMO system with single RF link based on switched parasitic antenna," *Symmetry*, vol 9, no 12, 2017.

[171] Y. Wu, K. Ding, B. Zhang, J. Li, D. Wu, K. Wang, Design of a compact UWB MIMO antenna without decoupling structure," *Int. J. Ant. Prop*. 2018.

[172] C. Votis, G. Tatsis, and P. Kostarakis, "Envelope correlation parameter measurement in a MIMO antenna array configuration," Int. J. Comm. Netw. Syst. Sci., vol, 3, pp. 350, 2010.

[173] M. S. Sahrawi, "Printed MIMO Antenna Engineering, Artech House: Norwood, MA, USA, 2014.

[174] B. C. Pan, W. X. Tang, M.Q. Qi, H. F. Ma, Z. Tao, and T. J. Cui, "Reduction of the spatially mutual coupling between dual-polarized patch antennas using coupled metamaterial slabs," *Sci. Rep*., vol. 6, pp. 1-8, 2016.

[175] A. Kumar, A. Q. Ansari, B. K. Kanaujia, and J. Kishor, "A novel ITI- shaped isolation structure placed between two-port CPW-fed dual band MIMO antenna for high isolation," *AUE-International Journal of Electronics and Communication*, vol. 104, pp. 35-43, 2019.

[176] R. Li, Z. Mo, H. Sun, X. Sun, and G. Du, "A low-profile and high-isolated MIMO antenna for 5G mobile terminal," *Micromachines*, vol. 11, no. 4, pp.360, 2020.

[177] R. A. Abd-Alhameed, "Design of Multi-Mode Antenna Array for Use in Next-Generation Mobile Handsets," *Sensors*, vol. 20, no. 9, 2020.

[178] W. A. Ali, M. I. Ashraf, and M. A. Salamin, "A dual-mode double-sided 4× 4 MIMO slot antenna with distinct isolation for WLAN/WiMAX applications," *Microsystem Technologies*, vol. 27, no. 3, pp. 967-983, 2021.

[179] S. P. Dubazane, P. Kumar, T. J. Afullo, "Metasurface superstrate-based MIMO patch antennas with reduced mutual coupling for 5G communications," *The Applied Computational Electromagnetics Society Journal (ACES)*, pp. 408-419, 2022.